

Review

Bioalcohol Reforming: An Overview of the Recent Advances for the Enhancement of Catalyst Stability

Vincenzo Palma , Concetta Ruocco * , Marta Cortese and Marco Martino 

Department of Industrial Engineering, University of Salerno, Via Giovanni Paolo II 132, 84084 Fisciano (SA), Italy; vpalma@unisa.it (V.P.); mcortese@unisa.it (M.C.); mamartino@unisa.it (M.M.)

* Correspondence: cruocco@unisa.it; Tel.: +39-089-964027

Received: 13 May 2020; Accepted: 9 June 2020; Published: 12 June 2020



Abstract: The growing demand for energy production highlights the shortage of traditional resources and the related environmental issues. The adoption of bioalcohols (i.e., alcohols produced from biomass or biological routes) is progressively becoming an interesting approach that is used to restrict the consumption of fossil fuels. Bioethanol, biomethanol, bioglycerol, and other bioalcohols (propanol and butanol) represent attractive feedstocks for catalytic reforming and production of hydrogen, which is considered the fuel of the future. Different processes are already available, including steam reforming, oxidative reforming, dry reforming, and aqueous-phase reforming. Achieving the desired hydrogen selectivity is one of the main challenges, due to the occurrence of side reactions that cause coke formation and catalyst deactivation. The aims of this review are related to the critical identification of the formation of carbon roots and the deactivation of catalysts in bioalcohol reforming reactions. Furthermore, attention is focused on the strategies used to improve the durability and stability of the catalysts, with particular attention paid to the innovative formulations developed over the last 5 years.

Keywords: hydrogen; bioalcohol; reforming; coke; catalyst stability; active phase; support; promoter

Summary

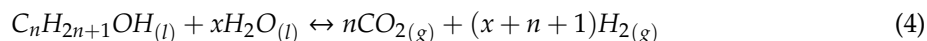
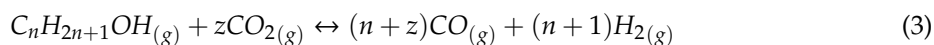
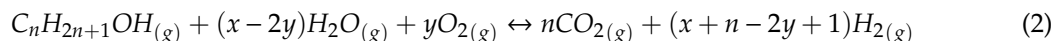
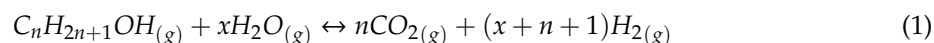
1	Introduction	Pag. 2
2	Bioethanol reforming	Pag. 3
2.1	The influence of the active phase	Pag. 8
2.2	The role of the support	Pag. 12
2.3	The effect of the addition of promoters	Pag. 13
3	(Oxidative) Biomethanol steam reforming	Pag. 19
3.1	The influence of the active phase	Pag. 20
3.2	The role of the support	Pag. 25
3.3	The effect of the addition of promoters	Pag. 27
3.4	Unconventional reactor configuration, simulation, and theoretical studies	Pag. 32
3.5	Oxidative steam reforming of methanol	Pag. 36
4	Bioglycerol reforming	Pag. 39
4.1	The influence of the active phase	Pag. 42
4.2	The role of the support	Pag. 43
4.3	The effect of the addition of promoters	Pag. 46
5	Other bioalcohol reforming	Pag. 50
5.1	The influence of the active phase	Pag. 51
5.2	The role of the support	Pag. 53
5.3	The effect of the addition of promoters	Pag. 54
6	Conclusions	Pag. 54

1. Introduction

The search for clean technology approaches able to assure safe and sustainable energy production is increasingly gaining ground due to the heavy impacts of fossil fuels on the world economy (oil price fluctuation), global warming, and human health [1,2]. An effective solution proposed to reduce the consumption of conventional feedstocks involves the use of hydrogen as an energetic vector, which leads to no or very low carbon emissions, as well as the release of atmospheric pollutants [3]. Steam reforming of natural gas is the most widespread technology for hydrogen production, and applying the same technology to new-generation (biomass-derived) fuels could offer significant energy and environmental advantages [4]. Biomass is abundantly available in different forms. The use of biomass for energy generation results in a neutral carbon balance; only trace amounts of sulphur and heavy metals are present in biomass compared to fossil fuels, thus limiting the formation of harmful substances [5]. Among the available fuels produced from biomass, bioalcohols are emerging as competitive sources for hydrogen production via reforming [6–8]. Bioalcohols (i.e., alcohols generated from biomass or biological routes) can be produced from different feedstocks, including crops, agricultural and forestry waste, and food waste [9]. First-generation biofuels are produced from sugar, starch, oil-bearing crops, or animal fats. Bioethanol is mainly obtained via fermentation of sugar cane or starches, while butanol and propanol are formed as co-products via well-established technologies [10]. Wood, agricultural residues, forestry residues (cellulosic, hemicelluloses, or lignin), organic waste, food waste, and specific biomass crops are the feedstocks used for second-generation bioalcohols. Bioethanol and biobutanol can be produced via fermentation of lignocellulosic sugars via different microorganisms; for the latter, the process is more difficult and not commercialized yet (only pilot plants are available) [11]. Ethanol and butanol can also be derived from algae (third-generation bioalcohols) [12]. Bioglycerol is produced during biodiesel generation via transesterification of triglycerides, using vegetable oil as the feedstock [13]. In addition, glycerol can also be generated as a by-product, along with bioethanol (consuming up to 10% of the weight of the employed sugar) [14]. As an alternative to the conventional approaches for methanol production (which employ natural gas or coal as feedstocks), other routes are available, mainly involving biomass gasification [15] (including the conversion of municipal solid waste [16], animal waste, and agriculture wastes [17]) and CO₂ hydrogenation [18].

Bioalcohol conversion (denoted as X) to hydrogen can follow different routes, including steam reforming (Equation (1)), oxidative steam reforming (Equation (2)), dry reforming (Equation (3)), and aqueous-phase reforming (Equation (4)) [8]. Among these processes, according to the stoichiometry of the reaction, steam reforming gives the highest hydrogen yields. However, several side reactions may occur during reforming, which besides affecting the H₂ selectivity, may also be responsible for carbon formation and catalyst deactivation. In this regard, the addition of oxygen via the oxidative process has been investigated as a viable route to mitigate carbon deposition [19,20]. The main pathways favoring coke formation during reforming include the Boudouard reaction, decomposition of carbon-containing intermediates (i.e., CH₄), dehydration, and subsequent polymerization reactions [21]. The same intermediates participating in the main reactions, in fact, may also be involved in coking pathways, while the contribution of side reactions depends on the operating conditions and the nature of both the active metal and the selected support [22]. In particular, a high water content and oxygen co-feeding disadvantage carbon formation [23,24], while the effect of the temperature on coke selectivity depends on the substrate, which influences the nature of the carbon formed and the effects of the coke gasification reactions [25,26]. In fact, it is clear that the product distribution and contributions of coke formation reactions also depend on the chosen molecule; it was found that the higher the number of the hydroxyl groups in a molecule, the lower the formation of CH₄, while CO selectivity was enhanced. In addition, species with longer carbon chains promote the formation of carbonaceous deposits. In fact, the number of hydroxyl groups influences the oxygen content in the reaction intermediates, along with their contributions to dehydration reactions [27]. The characteristics of the coke formed (amorphous or filamentous, with possible whiskers) also change depending on the starting substrate and the acidic–basic properties of the catalyst [28]. In particular, alcohols were

shown to be precursors of encapsulating coke, while CO and CH₄ were responsible for the formation of filaments, whose contribution to catalyst deactivation was more pronounced [29].



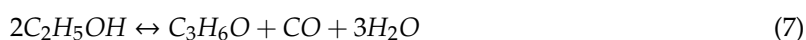
The reforming of bioalcohols has attracted the attention of several scientists, who have proposed different approaches to modulate catalysts' selectivity and improve their durability, including the use of additives and promoters (i.e., alkaline or transition metals and acidic or basic oxides) [30–32], the choice of high surface area supports or perovskites [33,34] and core–shell catalysts [35], the development of innovative preparation methods allowing enhanced dispersion of active species and improved metal–support interactions [36,37], and the synthesis of solid solutions for the confinement of active metals particles [38]. The deposition of catalysts on structured carriers (i.e., foams and monoliths) with high thermal conductivity or on microchannel walls was also shown to prevent the deterioration of catalytic performance due to the reduction of hot and cold spots [39–41]. In addition, the use of fluidized bed reactors was proposed as an effective route to separate filamentous coke from catalyst particles [42].

The present review focuses on the most recent advances to improve the stability and durability of catalysts for the reforming processes of five alcohols (ethanol, methanol, glycerol, butanol, and propanol), presenting a critical analysis of the main carbon formation roots for each substrate. Particular attention is devoted to innovative formulations developed in the last 5 years, analysing the contributions of the active phase, the support, and eventual promoters to catalyst stability. novel reactor configurations developed to improve the performances of the considered reforming processes are also assessed.

This review article is divided into three main sections based on the alcohol used in the catalytic process: ethanol, methanol, and glycerol. Finally, a further section focusing on butanol and propanol reforming is presented. Each of the main sections is divided into paragraphs to highlight the effects of the active phases, supports, and promoters. At the end of every section, a summary table is provided to compare the catalytic performance in terms of carbon formation rates.

2. Bioethanol Reforming

During ethanol steam reforming (ESR), the main pathways responsible for coke formation are ethanol cracking, dehydration reactions to ethylene (Equation (5)) and subsequent polymerization (Equation (6)), and aldol condensation of acetone (Equation (7)), followed by dehydration and oligomerization of mesityl oxide, CO disproportion (Boudouard reaction, Equation (8)), and methane dehydrogenation (Equation (9)); ethane can also be formed and subsequently dehydrogenated [43–45].



Based on the involved mechanism, different types of carbon can be formed (monoatomic adsorbed carbon, amorphous polymeric films, vermicular filaments, and graphitic crystalline platelets); while the monoatomic adsorbed carbon and polymeric coke are derived from the thermal decomposition of

hydrocarbons, metallic sites are directly involved in the formation of filamentous and graphitic coke [46]. The crystallization of carbon coming from ethylene polymerization is favored at high temperatures, while carbide species mainly derive from CH_4 decomposition, which can polymerize and form amorphous carbon or carbon whiskers; finally, carbon growth during Boudouard reactions may involve island formation [47,48]. For several transition metals (e.g., Ni, Co, Rh, Ru, Pd, Pt) [49], discrete Fourier transform (DFT) calculations reveal that before C-C bond breaking, an intermediate CH-CO bond is formed, which based on the reaction conditions and the nature of the metal surface can either dehydrogenate to form solid carbon or be hydrogenated to CH_4 during the C-C rupture. For example, in the case of Ni, it was shown that elevated temperatures favor intermediate decomposition over hydrogenation.

Ethanol reforming has been widely investigated under simulated bioethanol feeding (only containing water and ethanol); some studies were also performed with crude bioethanol feeding or a model mixture containing typical impurities (i.e., methanol, acetaldehyde, isopropyl alcohol, isobutyl alcohol, isoamyl alcohol). However, in the latter case, a faster catalyst deactivation was described. Glycerol and acetic acid are known as the major coke precursors; moreover, longer and heavier alcohols are not easily reformed but can be dehydrated to the corresponding olefins [50].

Liu et al. [51] described the mechanism of carbon formation on Ni/CeO₂ catalysts and the role of the hydroxyl groups in suppressing carbon formation (Figure 1). During ethanol steam reforming on the above catalysts, coke formation was mainly ascribed to the dehydrogenation of the surface methyl groups. Ni⁰, in fact, was the active phase leading to both the C-C and C-H cleavages of ethanol. In general, such methyl groups are not stable on the Ni(111) surfaces and are mostly dehydrogenated to surface carbon and hydrogen. However, in this study, surface carbon was formed through the generation of nickel carbides, which can also be originated from small amounts of ethoxy species decomposing on the Ni sites to form Ni₃C. Water can easily dissociate on the Ni-CeO_x to form hydroxyl groups, which together with the lattice oxygen on the surface, promote the oxidation of deposited carbon. However, the oxygen transfer from the ceria lattice to Ni particles is an endothermic reaction and only occurs above 470 °C. Thus, two competitive processes were described on the surface (carbon deposition and its oxidation by hydroxyls); the redox nature of the support as well as the Ni-ceria interactions are crucial to improve the oxygen transport and coke removal.

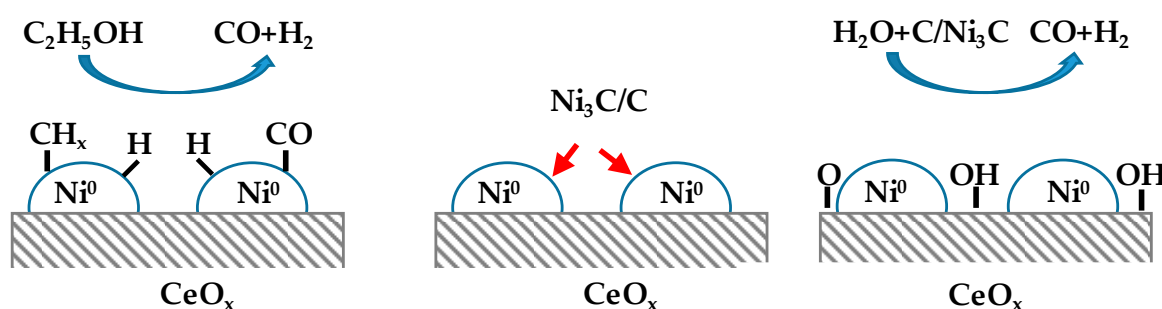


Figure 1. Mechanism of coke formation and removal on a Ni/CeO_x catalyst during ethanol steam reforming (ESR) [51].

The rate of ethylene formation throughout ESR is related to the support acidity and the amount of acidic sites on the catalysts' surfaces. Figure 2 displays the positive effects of acidic surface tailoring by the addition of Ti for a nanostructured Ni-Al catalyst [52]. Ti doping resulted in an expansion of pore sizes, thus improving the mass transfer and the contact between catalytic sites and reactants; moreover, the redox properties of the Ti⁴⁺/Ti³⁺ couple strongly influenced the catalyst selectivity.

In fact, due to the titania effect on the surface basicity, the ethylene formed via ethanol dehydration was more stable and coke generated from the C₂H₄ by polymerization and carbonization was thermodynamically less favoured and easier to decompose compared to the Ni sample containing only alumina.

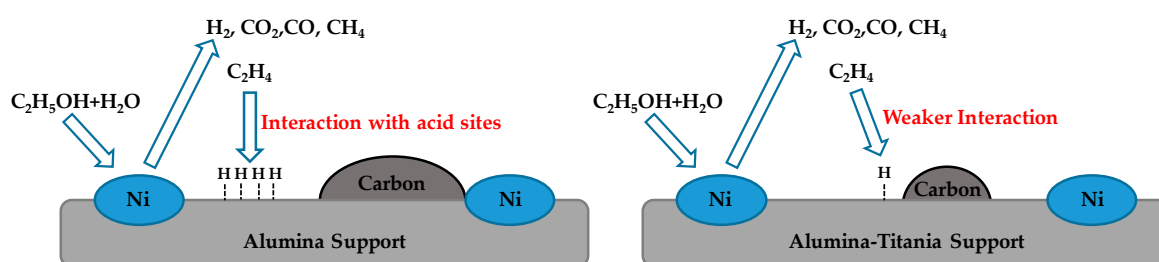


Figure 2. Mechanism of carbon formation of Ni-Al and Ni-Al-Ti catalysts during ethanol steam reforming [52].

For alumina-based catalysts, the beneficial effects of support modification by the addition of CeO_2 or La_2O_3 were shown, as well as for noble metals as active species (i.e., rhodium) [53]. The presence of low ceria loadings adds a Lewis acidity of medium strength to the $\text{CeO}_2\text{-Al}_2\text{O}_3$ mixed oxide, while the reduced carbon deposition on this support is related to the oxygen storage capacity and mobility of the ceria. In fact, the reversible release of oxygen makes O_x (lattice oxygen) available on the oxide surface. Carbon monoxide adsorbs on the surface, reacting with O_x and producing CO_2 . Moreover, the growth of carbon fibres is hindered by CeO_2 , which provides extra oxygen for gasification; solid carbon can react with oxygen lattices, further improving the yield to carbon oxides. Because CO is consumed to generate CO_2 , less carbon monoxide is available to be converted to coke via the Boudouard reaction. A different mechanism for the prevention of carbon build-up was reported for La_2O_3 . In the presence of lanthana, carbon dioxide is subtracted to the equilibrium via the formation of $\text{La}_2\text{O}_2\text{CO}_3$, which can react with the carbon metal species in its vicinity and generate CO.

The origin and nature of coke formed over $\text{Ni/La}_2\text{O}_3\text{-}\alpha\text{Al}_2\text{O}_3$ catalysts via ethanol steam reforming were reported in a work by Montero et al. [22]. The spent catalysts were characterized by scanning electron microscopy (SEM) analysis, which allowed the morphology of the carbonaceous deposits to be determined (encapsulating, filamentous, and graphitic carbon). Acetaldehyde, ethylene, and non-reacted ethanol were identified as the main coke precursors responsible for the deposition of encapsulating coke via cracking and polymerization, while filamentous and partially graphitic coke were derived from CH_4 and CO by decomposition and Boudouard reaction. As filamentous coke is located far from the metallic centers and is not able to cover the active sites (Figure 3), its influence on catalyst deactivation is reduced and the main impact on the catalyst activity loss comes from the encapsulation of active metal sites (in fact, the formation of filamentous coke caused a separation of metal nanoparticles from the support, without covering the active metal sites).

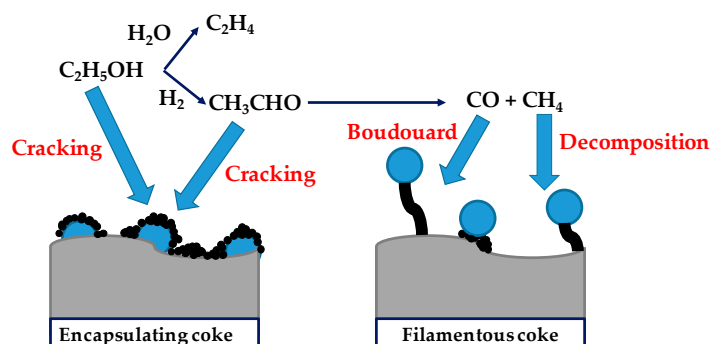


Figure 3. Mechanism and nature of coke formed over $\text{Ni/La}_2\text{O}_3\text{-}\alpha\text{Al}_2\text{O}_3$ [22].

The first mechanism is predominant at high temperatures and with low space velocity, while the second one is favoured at intermediate contact times, at which methane and carbon monoxide concentrations reach a maximum; the increases of the temperature and steam-to-ethanol ratio enhance carbon gasification, reducing the concentration of coke precursors on the surface.

For nickel core–shell-structured catalysts, it was found that during ESR reaction, the ethanol molecule is first dehydrogenated to acetaldehyde, which decomposes to CH_4 and CO , with a subsequent formation of carbon lumps. Conversely, if the ethanol dehydration occurs, ethylene is formed as an intermediate, which can easily polymerise into carbon nanotubes (CNT) [54].

Co@CoO_x core–shell-structured catalysts exposed to mild oxidants (i.e., H_2O and CO_2) during ESR reaction suffer from stressing and collapse of the structure, with an oxidation of the CoO_x core by means of the oxygen-free radical species which are, therefore, no longer available for the gasification of coke; for this system, carbon is mainly formed via dehydrogenation or condensation reactions [55]. Thus, sintering and formation of amorphous coke occurred. The promoting effect of ceria related to the $\text{Ce}^{3+}/\text{Ce}^{4+}$ redox cycle assured easier mobility of the active oxygen species, prevented re-oxidation of metallic Co particles, and at the same time allowed rapid consumption of carbonaceous species. For sol–gel alumina-supported cobalt catalysts, it was reported that the catalytic decomposition of ethylene on the Co sites was responsible for the formation of graphitic carbon, while amorphous coke was derived from the polymerization of carbon coming from methane decomposition. In addition, the influence of the CoO/Co^0 ratio on the carbon growth on the surfaces of the active sites was discussed. This ratio ruled the contribution of ethanol molecule activation and oxidation of adsorbed coke, with an optimal value of 1:3 selected to assure adequate activity and stability of the final catalyst [56].

Oxidative steam reforming of ethanol (OSRE) has also received considerable attention due to the role of gas-phase oxygen species, together with those components that are eventually presented as mobile lattice oxygen, in the oxidation of carbon deposited on the catalysts' surfaces [57,58].

For Ni-Cu bimetallic catalysts derived from hydrotalcite-like compounds, the effect of oxygen co-feeding during ethanol steam reforming was investigated at 500 °C under a molar ratio of water/ethanol/oxygen equal to 6:1:0.3. As depicted in Figure 4, O_2 addition mitigated the formation of filamentous-like coke deposits (which were observed under ESR conditions and caused the separation of metals nanoparticles from the support); oxygen promoted water production, limiting the adsorption of hydrogen (thus hindering the reduction of NiO) and CO or CH_4 products on nickel active sites (which are converted to CO_2 and CO). Moreover, the dissolution of gasified carbon in nickel particles with further diffusion through the metal was mitigated, thus hampering the growth of filamentous coke [59].

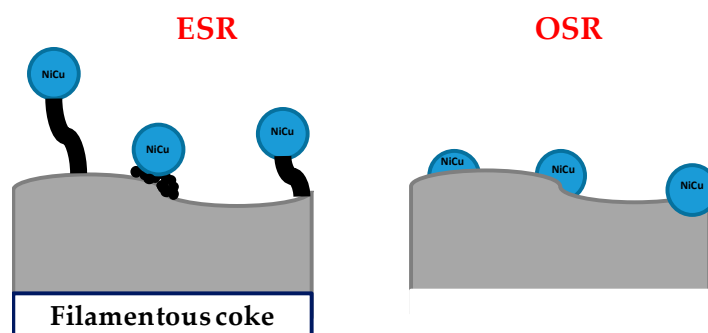


Figure 4. Effects of oxygen addition on carbon formation during ESR for Ni-Cu catalysts derived from hydrotalcite-like compounds [59].

The Pt-Ni/ CeO_2 - SiO_2 catalysts, tested under a reacting stream of $\text{C}_2\text{H}_5\text{OH}/\text{H}_2\text{O}/\text{O}_2 = 1/4/0.5$ at 500 °C, displayed better stability compared to the ESR measurements. The oxygen co-feeding improved coke gasification, thus resulting in diminished accumulation of carbon on the catalysts' surfaces; moreover, oxygen addition in the presence of the catalytic support having remarkable ionic conductivity encouraged the oxidation of carbon-containing species, without affecting the hydrogen production rate, which was almost the same for ESR and OSRE tests [60].

During stability tests in a fluidized bed reactor under OSRE conditions, the Pt-Ni/ CeO_2 - SiO_2 catalyst displayed only partial deactivation, and after 300 h of time-on-stream (TOS), the system

reached a new stationary condition with no more activity decay. When a plateau was observed in the gas product distribution, carbon deposition was measured at different time-on-stream values and no change in coke selectivity was observed. This phenomenon, depicted in Figure 5, can be explained by the fact that carbon deposition was not constant during the test. On the contrary, coke progressively accumulated on the most reactive catalytic sites (involved in both reforming reactions and carbon precursors generation). Therefore, the partial deactivation of the latter sites gradually reduced the carbon formation rate (CFR), and under stationary conditions the net rate of the carbon formation (i.e., the difference between coke formation and gasification) becomes equal to zero [61].

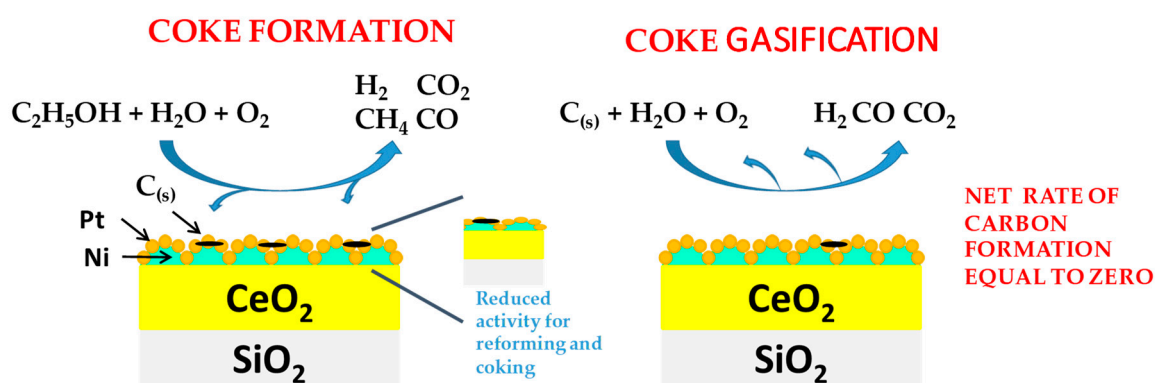


Figure 5. Description of the partial activity loss observed for Pt-Ni/CeO₂-SiO₂ catalysts during oxidative steam reforming of ethanol (OSRE) at 500 °C, where C₂H₅OH/H₂O/O₂ = 1:4:0.5 [61].

For ethanol dry reforming (EDR), the development of stable catalysts is a critical issue, especially when stoichiometric feeds are selected, implying that no excess of CO₂ is available to remove carbon deposits; ethylene polymerization, Boudouard, and methane decomposition reactions are the main routes for carbon deposition and for the reaction of ethanol with carbon dioxide [62]. In the presence of supports with redox properties, the removal of coke accumulated through the above pathways is favoured. CO₂, in fact, can re-fill the oxygen vacancy of the reduced support (i.e., ceria) to form CO and O; this atomic oxygen can be transferred towards the metal surface or the metal–support interface, thus favouring the gasification of carbonaceous deposits [63].

Compared to gas-phase processes, aqueous-phase reforming of ethanol has rarely been investigated in the last five years. Aqueous-phase reforming of ethanol (APRE) is carried out at temperatures below 300 °C; such mild operative conditions minimize the contribution of undesirable decomposition reactions and tend to mitigate coking phenomena (carbon formation is thermodynamically unfavourable) [64,65]. Thus, only a few works provide information about the accumulation of solid carbon on the catalysts' surfaces. Zhao et al. [66] proposed a mechanism for carbon formation over Ru-Pt/TiO₂ catalysts. Ethanol conversion via reforming passes through the cleavage of the C-C bond and the metal particle size influences the C1/C2 product ratio (larger particles assure a higher C1/C2 ratio). The energy barriers for C-C bond breaking are reduced on sites with low coordination at the corners and at step edges on metal surfaces. In fact, the most reactive sites (low coordination) can be strongly linked to the reaction intermediates (CO and CH_x), with a consequent hard regeneration of the catalytic site. Carbon formation can also be linked to Boudouard reaction, methane decomposition, ethylene polymerization, and cracking of ethane; however, CO disproportionation is more likely to occur. Despite the mechanism of APR of ethanol and the carbon formation pathways not being completely understood, for noble metals catalysts supported on titania, it was shown that the by-products selectivity decrease in the order of Ru > Rh > Pt > Ir [64] and that the metal particle size strongly affects the formation of intermediate species acting as coke precursors [67].

Accordingly, in order to minimize the problem of carbon deposition, different strategies have been proposed in the literature, including the control of the metal particle sizes and the addition of a second

metal or promoter able to change the electronic properties of the active species, as well as modify their interactions with the support [68–70]. In this section, the results of selected studies concerning steam reforming, oxidative steam reforming, dry reforming, and aqueous-phase reforming of ethanol are discussed. In the following paragraphs, bioethanol reforming with a focus on carbon formation will be discussed based on the nature of the active phase (Section 2.1), the chosen supports (Section 2.2), and the effects of promoters and additives (Section 2.3).

Ethanol reforming has been investigated with different noble and non-noble catalysts. Figure 6 groups the papers investigated in the present review based on the kind of active species selected.

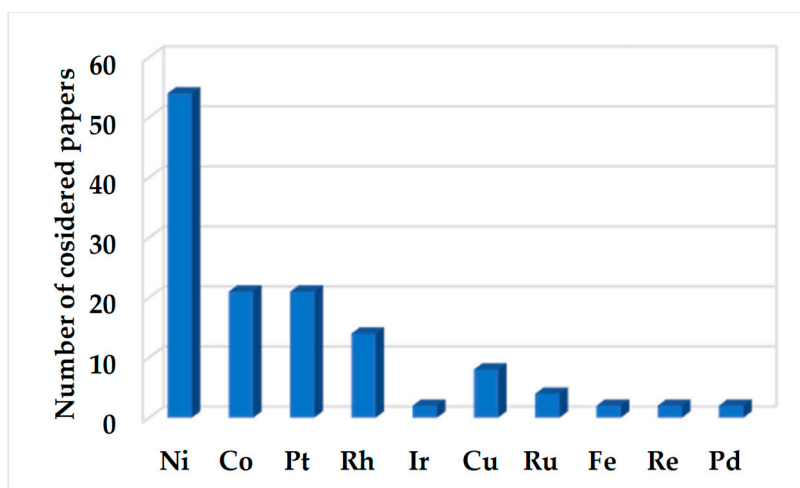


Figure 6. Number of considered papers as a function of the active phase analyzed for the ethanol reforming.

Nickel is the most widely selected metal for ethanol reforming, followed by cobalt. Moreover, among the noble metals, platinum and rhodium are most commonly selected.

2.1. The Influence of the Active Phase

In the following paragraph, the role of active species selection on catalyst stability for bioethanol reforming is discussed. In particular, various examples related to cobalt- and nickel-based catalysts are reported for the investigated processes, followed by the description of the performances of noble-metal-containing catalysts, as well as copper-based catalysts.

At 500 °C and under stoichiometric feeding conditions, CH₄ decomposition and Boudouard reaction were shown to be responsible for the formation of filamentous coke over Co₃O₄/CeO₂ catalysts during ESR [71]; carbon dissolves and subsequently precipitates on the rear of the metal, warding off the Co⁰ active sites from the support and leading to a loss of the Co⁰ active centers. However, by modulating the cobalt loading and particle dispersion, it is possible to vary the thickness of the filamentous coke, thus resulting in a good catalytic stability. In fact, active species dispersion and metal–support interactions are key factors affecting catalyst resistance towards deactivation. Thus, the improved stability of Co/CeO₂ catalysts during ESR at different temperatures (400, 600, and 800 °C) under a steam-to-carbon ratio of 3 compared to Ni-, Fe-, and Cu-based samples was ascribed to the strong metal–support interactions, which contributed to maintaining the Co species in an oxidized state; moreover, the gas–solid reactions between the hydrocarbon species adsorbed on the surface and the oxygen groups assured an easier gasification of such species, preventing their decomposition to coke [72]. For PtKCo/CeO₂ catalysts tested during oxidative steam reforming of ethanol, only a partial activity loss was observed and the reduced catalyst performance was ascribed to both carbon deposition and oxidation of cobalt metallic sites [73]. Carbon filaments were bonded to the support and contain cobalt particles at the top with the unblocked surface, not necessarily causing catalyst deactivation;

thus, only a few metallic particles were encapsulated by carbon and no longer participated in the reaction. In addition, non-filamentous coke (formed as a result of condensation and graphitization of carbon-containing species chemisorbed on the catalysts' surfaces) only covered the external surface of the active particles, while the middle part was still accessible to the reactants. Pt addition had a negligible effect on carbon deposition. It was also shown that the oxygen from the feeding can oxidize the surface atoms of cobalt particles, with a rate that increases for small particle sizes (lower than 4 nm).

The effect of the preparation method (mechanical mixing or sonication) on the stability performance of Co nanoparticles mixed with α -Al₂O₃ was reported by Riani et al. [74]. Well-dispersed Co nanoparticles displaying a good interaction with alumina were observed in the sonicated sample, while for the mechanically mixed catalyst only aggregate nanoparticles were detected. The results of stability tests carried out at 500 °C and under a steam-to-ethanol ratio of 6 proved that Co aggregates produced long carbon nanotubes, which embedded the active particles, while the tendency to form graphitic carbon is very low for the nanoparticles interacting with alumina.

For NiCo-MgAl catalysts prepared by microwave- or sonication-assisted co-precipitation, it was found that the prereduction of the catalyst is crucial to assure proper acid–base properties of the material, which affected the catalyst stability during OSRE. For the unreduced sample, in fact, a high basicity was observed, which favored certain unwanted pathways (including acetone generation), along with the formation of coke precursors [58].

The preparation method was also shown to affect the durability of Ni/SiO₂ catalysts for ESR [75]. Compared to the impregnated samples and those prepared by deposition–precipitation, the catalysts synthesized via strong electrostatic adsorption displayed improved interactions between the active phase and the support, assuring good control of the Ni particle size, which helped reduce the carbon deposition at 600 °C under a H₂O/C₂H₅OH ratio of 9. The same authors demonstrated the benefits of using silica fibers instead of the commonly used porous SiO₂. For porous catalysts, in fact, coke accumulates inside the pores and its gasification via the reaction with water is more difficult; conversely, carbon is deposited on the external surfaces of the fibers and its removal via gasification is easier.

The ultrasound-assisted synthesis of Ni/MgAl₂O₄ catalysts allowed sufficiently dispersed Ni particles to be obtained, even at high Ni loading [70]; the limited surface acidity, mainly due to the presence of Ni, promoted ethanol dehydration to ethylene, which for a Ni loading as high as 10% was further subjected to reforming, with very limited coking phenomena occurring.

Ni/Ce_{0.9}Sm_{0.1}O_{2- δ} nanowires were prepared via a simple two-step hydrothermal method followed by Ni deposited via wet impregnation. Such catalysts displayed high concentrations of oxygen vacancies on their surfaces and very low dimensions for Ni crystallites, assuring higher metallic surface areas compared to their analogue catalysts prepared from commercial doped ceria. Due to these improved properties, the Ni/Ce_{0.9}Sm_{0.1}O_{2- δ} sample displayed an exceptional stability with no loss of activity after 192 h of reaction at 550 °C under stoichiometric feeding conditions (no carbon deposits or filaments were detected for the spent catalyst) during ESR [76]. Ni/CeO₂ catalysts prepared via the sol–gel route displayed improved performance for APRE between 140 and 180 °C with 10 wt.% ethanol in water stream compared to the same catalyst synthesized via the solution combustion method. During the reaction, Ce₂O₃ reduced Ni²⁺ to Ni⁰ and was itself oxidized to CeO₂; the Ni sites can also be substituted for Ce in the CeO₂ lattice, thus increasing oxygen mobility in the structure. The enhanced oxygen mobility of the catalyst prepared by sol–gel method resulted in an improved coking resistance [77].

For Co/CeO₂ catalysts, the use of nitrates as inorganic salt precursors was shown to increase acetaldehyde and ethylene selectivity, with severe carbon deposition [78]; conversely, the choice of cobalt acetyl acetonate strongly enhanced the catalyst stability during ESR at 450 °C under a steam-to-ethanol ratio of 10, the organic ligands linked to the metal sites decreased the size of cobalt particles, improving their dispersion and assuring them a sort of imprinting effect, increasing the sites' accessibility to ethanol and water. Similarly, He et al. [36] prepared Ni/SBA-15 starting from two

different nickel precursors (nitrate and citrate) and tested them for ethanol reforming at 500 °C and a $\text{H}_2\text{O}/\text{C}_2\text{H}_5\text{OH}$ ratio of 3. In the first case, NiC_x species were detected, which were easily removed from catalysts' surfaces. On the contrary, the choice of Ni nitrate as a precursor led to the formation of carbon nanofibers (CNF) with a regular graphite structure, which covered the Ni active sites and were more difficult to remove. Similarly, Pt-Ni/ CeO_2 - SiO_2 was prepared by employing different cerium precursors (nitrate, ammonium nitrate, and acetyl acetonate) and tested at 500 °C $\text{C}_2\text{H}_5\text{OH}/\text{H}_2\text{O}/\text{O}_2 = 1:4:0.5$. It was found that the organic precursor assured a templating effect on the ceria crystallites, protecting them and improving their dispersion; as a result, the carbon formation rate was reduced by half compared to the samples synthesized from inorganic precursors [37].

Ni catalysts prepared by using a smectite-derived material as the starting precursor compared to conventionally impregnated samples displayed reduced crystallite sizes of Ni and a consequent higher resistance towards carbon formation [79]. In fact, during synthesis, Ni species migrated in the smectite framework, and despite moving towards the surface during the reaction, a strong interaction with the framework was maintained, inhibiting sintering. Since this interaction limited the growth of particles, it was possible to reach considerable nickel contents (up to 35 wt.%), thus resulting in high catalytic performance for ESR.

Noble-metal-based catalysts display lower coke formation and enhanced stability with time-on-stream testing compared to Ni or Co [80,81]. For Ir/ CeO_2 catalysts tested during ethanol dry reforming at 500 °C under a $\text{C}_2\text{H}_5\text{OH}/\text{CO}_2$ ratio of 1:1 [82], a very low amount of amorphous carbon was detected, proving that the strong interaction between the Ir particles and the ceria support efficiently prevented the sintering of Ir metal particles, as well as coke formation. Moraes et al. [83] investigated the effect on carbon build-up of Pt addition to a Ni/ CeO_2 nanocube catalyst for ethanol steam reforming at 300 °C and a steam-to-ethanol ratio of 3. The formation of a catalytically inactive nickel carbide phase (solid solution on carbon in Ni) was observed over the monometallic sample, which together with the accumulation of adsorbed acetates on the surface led to significant catalyst deactivation. As depicted in Figure 7, Pt inhibited the formation of NiC_x species, enhancing the hydrogenation rate of carbonaceous species. Moreover, the noble metal is characterized by slower carbon diffusion kinetics; thus, a decrease of the carbon diffusion rate throughout the Ni lattice was assured by the platinum particles (Ni carburization during the reaction was mitigated by a discontinuous Pt surface outer shell) [84]. As a result, the CFR during 28 h of time-on-stream tests was one-fourth of the value recorded for the monometallic catalyst.

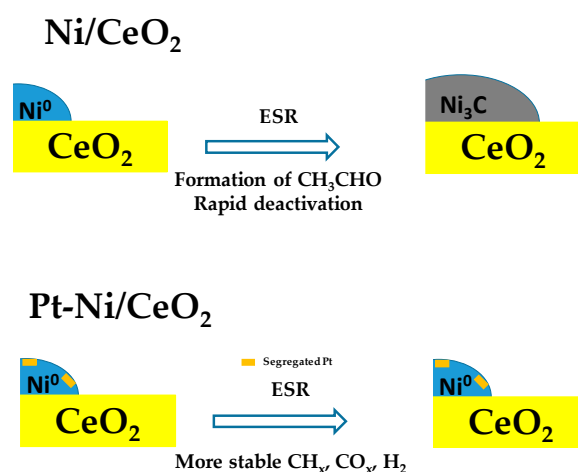


Figure 7. Effect of Pt addition on carbon formation for Pt/ CeO_2 catalysts [84].

For noble-metal-based catalysts, due to the reduced solubility of carbon on the surface, it was shown that carbon nucleation is energetically unfavourable; the noble metal lattice is too large compared to graphene lattice, thus inhibiting its formation. As a consequence, the formation of superficial carbon

instead of more structured deposits is promoted in the presence of supported noble metal catalysts (the solubility of carbon in the latter material is very low) [85].

Similar results were also reported by Palma et al. [86]. The addition of Rh to Ni/CeO₂-La₂O₃ samples enhanced the catalyst stability due to multiple effects, involving the reduced accumulation of acetate as well as the higher capacity for gasification of the methyl groups produced via decomposition of intermediates. In fact, acetates (derived from acetaldehyde dehydrogenation and subsequent oxidation) can be converted to CH_x species or may accumulate on the surface of the Rh-free catalyst, leading to acetone formation and subsequent carbon deposition. As a result, the Rh-Ni catalyst displayed almost no carbon formation for 24 h of reaction at 500 °C under a steam-to-ethanol ratio of 3 [87]. The excellent stability of Rh-Pt/CeO₂ catalysts during ESR under stoichiometric feeding conditions at 700 °C was ascribed to the formation of a Rh-Pt alloy containing both Rh and Pt oxidized species, which also led to very small metal particles (almost 5 nm). The control of the carbon accumulation was related to the availability of surface oxygen, which travels from the support, crossing the active metals and reaching the CH_x coke precursors [85].

The basic properties of the Rh_{0.4}Pt_{0.4}/CeO₂ catalyst assured stable performance during steam reforming of a bioethanol feed (having a steam-to-ethanol ratio of 3 and containing ethyl acetate 0.5 mol.%, 1,1-diethoxyethane 0.2 mol%; trace constituents: propanol, 2-methyl-1-propanol, 3-methyl-1-butanol, and 2-methyl-1-butanol) at 700 °C, where alcohol dehydration was disadvantaged, along with olefin production and further carbonaceous deposition on the catalysts' surfaces [88].

Due to the differing affinity for carbon deposit formation (different adsorption energies of the C-containing intermediate species were reported), Pt/Al₂O₃ and Rh/Al₂O₃ catalysts displayed dissimilar behaviour during steam reforming of crude bioethanol at 500 °C under a steam-to-ethanol ratio of 5 and with 1% impurities [89]. The carbon formation rate of the platinum-based catalyst was affected by the type of impurity selected and decreased in the order of IPA (Isopropyl alcohol) > 1-propanol > pure ethanol > propanal > propylamine > acetone, while the Rh/Al₂O₃ showed a higher durability, with a negligible trend related to the contaminants. A Pt-Co/CeO₂-ZrO₂-Al₂O₃ catalyst was successfully employed for the steam reforming of a real bioethanol feed coming from the industry (having a steam-to-ethanol ratio of approximately 6 and also containing sulphur/phosphorous compounds); during stability measurements at 400 °C, coke deposition did not occur [90].

In some cases, the addition of a second non-noble metal (i.e., Co or Cu) had a mitigating effect in terms of carbon deposition [32,91]. The improved stability of Ni-Co/SBA-15 catalysts upon cobalt deposition was ascribed to the formation of a carbide phase (thermodynamically stable against decomposition to metallic Co and graphitic carbon), which assures a decrease in cobalt particle sizes [92]. Reduced C₂H₄ formation was observed during ESR for NiCu ex-hydrotalcite catalysts compared to the copper-free sample, which limited the deposition of graphitic carbon, as well as the formation of carbon filaments having small metallic particles at their growing tips.

For copper-nickel oxide catalysts [93], it was also reported that the metal-oxide interface facilitates the transformation of CH_x-adsorbed species resulting from acetaldehyde decomposition into methoxy-like adsorbed species, which are readily reformed to produce H₂ instead of being decomposed to solid carbon.

Braga et al. [94] investigated the effect of Co addition to Ni/MgAl₂O₄ on its stability during OSRE at 500 °C under H₂O/EtOH/O₂ = 3:1:0.5. Filamentous carbon was deposited on bimetallic Ni-Cu samples and the rate of carbon deposition increased for lower Co contents. The carbon gasification rate depends on the presence of surface oxygen for the oxidation of the *C species; the small dimension of cobalt particles (lower than 5 nm) interacting with Ni enhanced the fraction of oxidized Co available to oxidize the carbon species on metal sites. Thus, cobalt deposition on Ni/MgAl₂O₄ effectively mitigated coke accumulation, with the best results recorded for the 4Co-4Ni catalyst.

2.2. The Role of the Support

The present paragraph describes the crucial role played by the catalytic support in preventing coking phenomena, mainly linked to its acidic and basic features, as well as its structural properties. Thus, the identification of the acidic and basic sites of the support is fundamental for the understanding of coke formation mechanisms.

For Rh/CeO₂ catalysts tested during ESR [95], NH₃ temperature-programmed desorption (TPD) results indicate the presence of strong basic sites; however, a slightly acid behaviour was also observed. Different paths of ethanol molecule activation are observed based on the site features. Acidic sites favour dehydration reactions and ethylene formation, which is a well-known coke precursor; while the dehydrogenation pathway is promoted in basic sites, leading to the formation of C₂H₅O* intermediates, which can decompose to CH_x species and further be oxidized to CO and CO₂.

La₂Ce_{2-x}Ni_xO_{7-δ} catalysts displayed very stable behaviour during oxidative steam reforming of ethanol. Ni incorporation into the pyrochlore structure, as well as the synergistic effect of nickel and cerium ions, induced the formation of Ce³⁺ ions, thus creating oxygen vacancies. This effect, together with the good dispersion of Ni particles and the presence of NiO as an impurity (sintered nickel oxides promote coke accumulation), mitigates coke deposition [96]. The same authors synthesized pyrochlore catalysts substituted by Li and Ru in A and B sites and supported them on Al₂O₃ or La₂Zr₂O₇. Substitution of La³⁺ by Li⁺ metal cations modified the relative compositions of active metal ions Ruⁿ⁺/Ru⁴⁺ and Ce⁴⁺/Ce³⁺, thus enhancing formation of vacancies and increasing the carbon oxidation rate. Moreover, during tests performed at 350 °C under stoichiometric feeding conditions, disordered carbonaceous and ordered graphitic species were formed over the alumina-supported catalyst, while no coke accumulation was observed for the La₂Zr₂O₇-based sample. The basic properties of this support, in fact, suppressed ethylene formation and its successive polymerization [97].

For Cu catalysts supported on CeO₂, ZrO₂, and CeO₂-ZrO₂, and tested during ethanol dry reforming, it was found that the concentration of the oxygen vacancies decreased in the order of Cu/CeO₂-ZrO₂ > Cu/CeO₂ > Cu/ZrO₂. Thus, coke formation was inhibited and its degree of graphitization reduced with the Cu/CeO₂-ZrO₂ catalysts, which displayed the highest durability at 700 °C under a C₂H₅OH/CO₂ ratio of 1:1 [98]. Cu/Ce_{0.8}Zr_{0.2}O₂ catalysts displayed negligible deactivation during dry reforming of ethanol at 700 °C and a C₂H₅OH/CO₂ ratio of 1:1. In fact, the incorporation of Cu prevented the crystallite growth of the Ce-Zr-O solid solution, which may occur during preparation; thus, the mean crystallite size of the CuCeZr catalyst was approximately 3.1 nm (lower than the value of 5 nm reported for the pure ceria-zirconia support); smaller particles are reported to reduce the formation enthalpy of oxygen vacancies. As a result, coke accumulation and sintering were mitigated [99] and stable behaviour with complete ethanol conversion for 90 h of time-on-stream was recorded [100]. Dang et al. [101] investigated the dry reforming of an ethanol/glycerol mixture (4:1) over a Ni/CaCO₃ catalyst: CaCO₃ reacted with the alcohols to yield CO, H₂, and CaO, while CO₂ allowed for CaCO₃ to be regenerated. The presence of carbonates was beneficial for suppressing coke accumulation; the highly reactive carbonaceous species can interact with the CO₂ coming from the carbonate decomposition and can be easily converted to carbon monoxide.

The metal particle size and the dispersion of the active phase are also affected by the structure of the support. Da Costa-Serra and Chica [102] studied ethanol steam reforming for two Co-based catalysts supported on structured manganese oxides (Birnessite and Todorokite). In the latter case, the special microporous structure of the support provided high-quality positions for the stabilization of the cobalt particles (i.e., the microporous structure assures a good interaction of the metal particles with the support) during the preparation, thus leading to smaller metal particles compared to the birnessite-based sample (6 vs. 12 nm). As a result, carbon accumulated during a 24 h ESR test at 500 °C under a H₂O/C₂H₅OH ratio of 13 was almost one-half of the todorokite-supported Co catalyst. The superior stability of a Ni/KIT-6 catalyst (ordered silica) for ethanol dry reforming at 550 °C under a C₂H₅OH/CO₂ ratio of 1 compared to a nickel sample supported on mesoporous silica was ascribed to the stabilization of the Ni species via the formation of Si-O-Ni-O-Si bonds, with a consequent confinement

within the pores of the ordered structure; such confinement resulted in a stronger metal–support interaction and smaller Ni particles compared to the Ni/SiO₂ catalyst, which enhanced the resistance towards coke formation [103]. By depositing a Pt-Ni/CeO₂ catalyst on high surface area mesoporous silica, a better dispersion of both metal and ceria particles was observed compared to the silica-free sample, thus enhancing the catalyst stability during ESR. The bimetallic catalysts were also prepared at different CeO₂/SiO₂ ratios (0.25, 0.30, and 0.40), and the relationship between the CFR and average Ni crystallites calculated for the spent catalysts was investigated. The smallest crystallite size, which was linked to the minimum coke selectivity, was recorded for a ratio of 30% [60].

Catalyst deposition on specific structured carriers may also affect their stability performance for ethanol reforming. The enhanced mass transfer rate and the improved gas–solid contact of structured carriers (i.e., foams, honeycombs, and monoliths) are expected to increase the contribution of coke gasification reactions, with a consequent mitigation in the deactivation of the catalyst [40,104]. Rh/CeSiO₂ catalysts supported on a ceramic monolith were subjected to a water/ethanol mixture of 3.5 at 755 °C, and no coke formation was observed during 96 h of operation [105]. Cobalt deposition on a Y₂O₃-doped ZrO₂ monolith eliminated the generation of undesired by-products (C₂H₂ and C₂H₄O), whose formation in the presence of the corresponding powder material was responsible for carbon deposition. Moreover, the stability of such structured catalysts was enhanced by infiltrating La into the monolith structure [106]. For the steam reforming of a simulated bioethanol for (containing 1 mol% of acetaldehyde, isopropyl alcohol, isobutyl alcohol, and isoamyl alcohol) over a Pt-Ni/CeO₂-ZrO₂ catalyst supported on a SiC foam, it was observed that the binder employed during the deposition of the catalytic wash coat on the structured carrier may affect catalyst stability [107]. The choice of boehmite as a binder reduced the carbon formation rate during tests at 450 °C at a steam-to-ethanol ratio of 3 compared to both the corresponding powder sample and the structured carrier containing silica as a ligand. In the latter case, in fact, very fast deactivation was observed, which was described as follows: during reforming reactions, steam can attack silica-structured Si atoms, with consequent structural changes for silica. Thus, active species particles can be wrapped or buried within the structure, losing their activity.

2.3. The Effect of the Addition of Promoters

The addition of promoters is a common strategy to mitigate carbon deposition on the catalysts' surfaces during ethanol reforming, and in the following paragraph, the influence of various promoters (mainly alkali metals and rare earths elements) on catalyst stability for bioethanol reforming is discussed.

For Co/CeO₂ catalysts tested during ESR, it was reported that the Co particle size influences the type of carbonaceous deposits; large cobalt particles caused the formation of carbon filaments with encapsulated cobalt (carbon diffuses inside the crystallites, destroying them and the causing growth of nanofibers), while few atomic layers of carbon, mainly located at the boundary of the Co and CeO₂ particles, were detected over small cobalt particles. The same authors found that the concentration of hydroxyls groups on the catalysts' surfaces (modulated on the basis of the steam-to-ethanol ratio) is crucial to changing coke selectivity. In this regard, a high concentration of OH species and K-O sites was assured upon potassium addition. Potassium, in fact, is able to favor the conversion of coke precursors to CH_x instead of fully dehydrogenated C = C species (mainly graphitic whiskers and layers) [108]. Moreover, the formation of carbonaceous deposits was also prevented over Co/ZrO₂ catalysts promoted by potassium, mainly due to the decreased contribution of the CO disproportionation reaction [109]. La₂O₃ promotion improved the active species dispersion and the metal–support interactions for Co/CeO₂ (and Ni/CeO₂) catalysts; the lower carbon formation was attributed to the formation of La₂O₂CO₃ as an intermediate phase, which contributes to eliminating carbon deposits, leading to the formation of carbon monoxide [110]. Cerdà-Moreno et al. [111] investigated the effect of La addition as a promoter on the stability of CoZn hydrotalcites at 600 °C for the steam reforming of a raw bioethanol stream containing several impurities (acetaldehyde, methanol, propanol, and SO₂) and

having a steam-to-ethanol ratio of 10; the improved performance of the lanthanum-containing catalyst is mainly related to the reduced C_2H_4 selectivity.

For Ni/SBA-15 catalysts, the introduction of Mn as a promoter and the subsequent change in the redox properties of the catalytic support favored the formation of a lower amount of coke lumps (carbon donuts surrounding Ni particles), with less activity loss during ESR compared to the Mn-free catalysts [54]. A similar reduction in the extent of deactivation and the same differences in the types of coke formed were observed by adding Mo to Ni/SBA-15 catalysts [112] and Mn to Co/SBA-15 catalysts [113].

The synthesis of a Ni-Ce-W oxide catalyst via reverse microemulsion allowed W and part of the Ni to be incorporated into the ceria lattice, while the remaining Ni formed highly-dispersed nano-NiO (almost 2 nm) outside the Ni-W-Ce oxide structure. Due to the synergy between Ni and W inside the ceria lattice, an increase of the oxygen vacancies with respect to the W-free sample was observed, which assured considerable resistance towards coke formation during ESR [114].

Compared to the ceria-free samples, CeO_2 -promoted Ni/SBA-15 catalysts displayed well-dispersed nickel particles confined in the mesoporous channels of SBA-15 [115]; the metal-support interactions led to a homogeneous distribution of Ni and Ce with a large Ni- CeO_2 interface, which contributed to controlling the size of Ni particles. Ni's ability to break CO bonds responsible for CO disproportionation and carbon deposit formation was mitigated thanks to the strong electronic perturbation induced by ceria. In addition, the OH groups present on the ceria surface, together with those derived from steam, can easily react with methyl groups to generate CO, CO_2 , and H_2 . The high oxygen mobility in the ceria lattice enhanced the carbon gasification rate and assured a lower rate of carbon deposition. Thus, ceria can effectively minimize sintering and coking over Ni/SBA-15 catalysts during ethanol steam reforming at 700 °C and a H_2O/C_2H_5OH ratio of 4, reducing the accumulated amount of coke deposited by almost 70%.

In an attempt to improve the stability of NiMgAl catalysts, Du et al. [116] investigated the addition of various promoters, which modulated the electronic properties of the final catalyst. NiCoMgAl catalysts, compared to the Mn- or Zr-promoted samples, displayed higher durability, ascribable to the good metal dispersion and small metal size, which hindered carbon deposition and sintering (small particles of metals such as Ni have been found to block the mechanism of carbon filament growth and to decrease carbon accumulation). Conversely, an enhanced rate of carbon formation (mainly in a filamentous form) was observed for the NiMnMgAl and NiZrMgAl samples. Ce addition to NiMgAl reduced the dimensions of metal particles, while the presence of lanthanum increased the surface Ni content and the number of basic sites; in both cases, a reduced carbon formation rate was measured. Similarly, the benefits of supporting $LaNiO_3$ catalysts on $CeSiO_2$ were reported [117]. The presence of SiO_2 blocked the sintering of ceria particles and the very low carbon formation rate recorded during ESR at 700 °C, while a H_2O/C_2H_5OH ratio of 3 over the $LaNiO_3/CeSiO_2$ catalyst was ascribed to the metal-support interactions, which contributed to maintaining small dimensions for Ni crystallites. The size of metal particles, in fact, affects the nucleation rate of carbon; a critical ensemble size (ensemble of 6–7 atoms) was proposed, below which carbon formation does not occur. For these catalysts, it was also reported that after initial deactivation, new stability conditions were reached, despite the presence of carbon on the catalyst's surface. The initial loss of activity was observed when the rate of formation of CH_x species was higher than their rate of desorption to form CH_4 . Such species can be further dehydrogenated to C as well as H, and the highly-reactive carbon species can both encapsulate metallic particles, leading to complete deactivation, or diffuse through the Ni crystallites and nucleate the growth of carbon filaments. In the latter case, the top surface is still in contact with the reacting mixture and the catalyst is able to maintain its activity for the ESR. Dan et al. [118] investigated the steam reforming of a fir wood crude bioethanol over Ni/ Al_2O_3 catalysts (containing methanol, acetic acid, higher alcohols, esters, aldehydes, organic acids, and dimethyl furan). However, the bioethanol displayed rapid deactivation during tests at 350 °C, due to the deposition of graphitic carbon. A significant improvement in its durability was observed with the addition of rare earth

oxides, with La_2O_3 decreasing the alumina surface acidity and CeO_2 promoting water activation for the gasification of coke deposits. Thus, stable performance was recorded for 4 h at 350 °C.

Likewise, the incorporation of Au into Ni/SBA-5 catalysts improved the dispersion of the NiO phase to form smaller nickel oxide particles. In addition, strengthened interactions between the SBA-15 support and NiO phase were assured, thus efficiently reducing the coke deposition on active sites [119].

Mondal et al. [120] described the performance of unpromoted and Rh-promoted Ni/CeO₂-ZrO₂ catalysts for oxidative steam reforming of a crude bioethanol stream (containing ethanol, butanediol, butandioic acid, acetic acid, and glycerol). Stability tests were performed at 600 °C and EtOH/H₂O/O₂ = 1:13:0.35. The addition of Rh led to smaller dimensions for Ni crystallites, and despite both amorphous and rod-shaped filamentous carbon nanotubes being observed for the two spent catalysts, the Rh-Ni/CeO₂-ZrO₂ lessened the deposition of encapsulating amorphous coke, thus exhibiting a significantly lower deactivation rate.

The addition of Ce or La to Ni/Al₂O₃ acted as a spacer, preventing NiO particles from aggregating, and hence increasing metal dispersion on the catalyst's surface; thus, improved stability was recorded for ethanol dry reforming. In particular, despite multiwalled carbon nanofibers being deposited on both the promoted and unpromoted catalysts, the stable performance of rare-earth-containing samples was related to the absence of encapsulated Ni particles located on the tip of the filamentous nanocarbon [121,122]. In addition, in the presence of CO₂, the formation of the La₂O₂CO₃ intermediate discussed above was enhanced, along with its ability to oxidize surface C_xH_y species and to preserve active metal sites. Similar results were also reported for Ce-doped Co/Al₂O₃ catalysts [123], La-doped Co/Al₂O₃ [124], and La-doped Cu/Al₂O₃ catalysts [125].

In some cases, the addition of a promoter did not lead to the desired performance improvement. For the Ni/CeO₂ catalyst, the addition of K caused faster deactivation due to the deposition of a very large amount of graphitic fibres, which were longer and thicker than those observed over the unpromoted catalyst; these graphitic fibres encapsulated the nickel crystallites, resulting in an activity loss [126]. For Pt-Ni catalysts, the addition of a third metal (K, Cs, or Rh) as a promoter was investigated, finding that caesium and rhodium are able to reduce the carbon formation rate during ESR at 450 °C and under stoichiometric feeding conditions, while in the presence of potassium, this addition was detrimental for catalyst stability [23].

Table 1 summarizes the stability performance of different catalysts proposed over the last 5 years for steam reforming, oxidative steam reforming, and dry reforming of ethanol. As discussed above, various parameters affect the catalyst durability and carbon formation rate, including the catalyst composition (active species, support, promoters) and operative conditions (temperature, feeding, and space velocity). A high ethanol concentration, low contact time, and high steam/ethanol ratio increase carbon accumulation on the catalyst's surface. Moreover, noble-metal-based catalysts displayed lower coke formation compared to Ni- or Co-based catalysts, with the addition of promoters lessen the coke selectivity. In fact, as can be seen from the data reported in Table 1, when ESR was performed over Ir- and Rh-based catalysts, the CFR was among the lowest reported in the present review. Very low carbon formation rates were also measured in the presence of Pd, as well as for bimetallic Rh-Ni catalysts. Carbon formation rates range between 10⁻² to 10⁻⁷; overall, during oxidative steam reforming of ethanol, reduced coke selectivity values were recorded compared to the steam reforming and dry reforming cases, due to the enhanced contribution of gasification reactions promoted by O₂. In this regard, the highest stability was assured over the Pt-Ni/CeO₂-SiO₂ catalysts, as well as over Ru-based perovskites containing La as a promoter. During dry reforming, the extent of catalyst deactivation was enhanced due to the absence of water in the feed, which is crucial for the promotion of carbon gasification; thus, CFR, defined as the ratio between the mass of carbon, measured in g, and the product of the catalytic mass (measured in g), the mass of carbon feed during the test (in g) and the time on stream (in hours), was of the order of 10⁻³ g_{coke}·g_{catalyst}⁻¹·g_{carbon, fed}⁻¹·h⁻¹. However, a strong improvement in catalyst stability was observed by selecting ceria and zirconia instead of alumina as the catalytic support. The results reported in Table 1 also show the effects of the catalyst preparation

method and the salt precursor selection on the stability of the final catalyst during ethanol reforming. In particular, the lowest values for carbon formation rates were recorded for the catalysts prepared by sonication (which assured lower dimensions for metal crystallites and a better active species–support interaction) instead of impregnation; moreover, the choice of organic salts as precursors improved the dispersion of active species, thus resulting in a more stable catalyst.

Table 1. Carbon formation rates of various catalysts employed for steam reforming, oxidative steam reforming, and dry reforming of ethanol.

Catalyst ^a	Operative Conditions ^b	WHSV ^c (h ⁻¹)	X EtOH (%)	Carbon Formation Rate ^d (Multiplied for 1000)	Ref.
Ethanol steam reforming					
1Pt-3Ni/CeO ₂ -SiO ₂	T = 450 °C S/E = 4 %C ₂ H ₅ OH = 10%	4.1	95% after 310 min	3	
0.5Rh-1Pt-3Ni/CeO ₂ -SiO ₂	T = 450 °C S/E = 4 %C ₂ H ₅ OH = 10%	4.1	93% after 1300 min	0.84	[23]
1Rh-3Ni/CeO ₂ -SiO ₂	T = 450 °C S/E = 4 %C ₂ H ₅ OH = 10%	4.1	91% after 4900 min	0.065	
1Pt-3Ni-0.5K/CeO ₂ -SiO ₂	T = 450 °C S/E = 4 %C ₂ H ₅ OH = 10%	4.1	92% after 200 min	17	
1Pt-3Ni-0.5Cs/CeO ₂ -SiO ₂	T = 450 °C S/E = 4 %C ₂ H ₅ OH = 10%	4.1	94% after 1600 min	0.39	
Ni-Co/mesoporous carbon (MC)	T = 375 °C S/E = 12 %C ₂ H ₅ OH = 4%	1.2	0% after 700 min	14	[32]
Ni-Co/2Zr-MC	T = 375 °C S/E = 12 %C ₂ H ₅ OH = 4%	1.2	77% after 700 min	7.1	
Ni-Co/2Y-MC	T = 375 °C S/E = 12 %C ₂ H ₅ OH = 4%	1.2	90% after 700 min	8.1	
LaNi _{0.85} Zn _{0.15} O _{3-δ}	T = 700 °C S/E = 3 %C ₂ H ₅ OH = 18.6%	8.2	100% after 8 h	2.7	[34]
10Ni/9La ₂ O ₃ -αAl ₂ O ₃	T = 500 °C S/E = 3 %C ₂ H ₅ OH = 8 %	11.5	32 % after 20 h	0.19	[42]
5Co/CeO ₂	T = 500 °C S/E = 3 %C ₂ H ₅ OH = 25%	6.8	94% after 6 h	25	[71]
10Co/CeO ₂	T = 500 °C S/E = 3 %C ₂ H ₅ OH = 25%	6.8	98% after 6 h	75	
20Co/CeO ₂	T = 500 °C S/E = 3 %C ₂ H ₅ OH = 25%	6.8	98% after 6 h	58	
10Ni/CeO ₂	T = 300 °C S/E = 3 %C ₂ H ₅ OH = 2.5%	2.1	10% after 30 h	0.15	[84]
1Pt10Ni/CeO ₂	T = 300 °C S/E = 3 %C ₂ H ₅ OH = 2.5%	2.1	33% after 30 h	0.19	[84]
1Rh-10Ni/15La ₂ O ₃ -10CeO ₂ -Al ₂ O ₃	T = 500 °C S/E = 3 %C ₂ H ₅ OH = 18.8%	42.2	100% after 24 h	0.00031	[87]
Co-La/CeO ₂ La/Co mol ratio 0.1	T = 420 °C S/E = 12 %C ₂ H ₅ OH = 7.7%	9.5	60% after 21 h	0.17	[110]
Ni-La/CeO ₂ La/Ni molar ratio of 0.1	T = 420 °C S/E = 12 %C ₂ H ₅ OH = 7.7%	9.5	99% after 21 h	19	
3Ni/SBA-15	T = 650 °C S/E = 4 %C ₂ H ₅ OH = 4.5%	25.7	70% after 50 h	0.19	[115]
3NiCe/SBA-15 Ce/Ni molar ratio of 1:1	T = 650 °C S/E = 4 %C ₂ H ₅ OH = 4.5%	25.7	90% after 50 h	0.045	[115]
0.4Pt-0.4Rh/CeO ₂ -SiO ₂ Si/Ce molar ratio of 1:2	T = 680 °C S/E = 3 %C ₂ H ₅ OH = 1.8%	14.3	100% for 72 h	0.16	[127]
2Ir/CeO ₂ nanoparticles	T = 650 °C S/E = 3 %C ₂ H ₅ OH = 25%	9.23	80% after 45 h	0.0083	[128]
2Ir/CeO ₂ nanoroads	T = 650 °C S/E = 3 %C ₂ H ₅ OH = 25%	9.23	55% after 45 h	0.0096	[128]
1Rh/Al ₂ O ₃	T = 500 °C S/E = 3 %C ₂ H ₅ OH = 14%	40.7	80% after 45 h	0.028	[129]
1Rh-15%La ₂ O ₃ -Al ₂ O ₃	T = 500 °C S/E = 3 %C ₂ H ₅ OH = 14%	40.7	90% after 45 h	0.0029	[129]
1Rh-15%La ₂ O ₃ -5%CeO ₂ -Al ₂ O ₃	T = 500 °C S/E = 3 %C ₂ H ₅ OH = 14%	40.7	97% after 45 h	0.0016	[129]

Table 1. Cont.

Catalyst ^a	Operative Conditions ^b	WHSV ^c (h ⁻¹)	X EtOH (%)	Carbon Formation Rate ^d (Multiplied for 1000)	Ref.
Co-Mg@mesoporous Al ₂ O ₃ Co/Al molar ratio of 0.1:1 Mg/Al mol ratio 0.25:1	T = 550 °C S/E = 5 %C ₂ H ₅ OH = 6.7%	4.8	100% after 4 h	9	[130]
LaNiO ₃ /ZrO ₂	T = 650 °C S/E = 3 %C ₂ H ₅ OH = 5%	27.1	80% after 50 h	0.57	[131]
LaNi _{0.7} Co _{0.3} O ₃ /ZrO ₂	T = 650 °C S/E = 3 %C ₂ H ₅ OH = 5%	27.1	96% after 50 h	0.36	
LaCoO ₃ /ZrO ₂	T = 650 °C S/E = 3 %C ₂ H ₅ OH = 5%	27.1	70% after 50 h	0.68	
10Ce/Ni-Mg-Al	T = 540 °C S/E = 6 %C ₂ H ₅ OH = 14.3%	2.1	83% after 10 h	0.51	[132]
5Ni/CNTs-SiO ₂ fibers	T = 450 °C S/E = 9 %C ₂ H ₅ OH = 10%	2.6	87% after 22 h	1.2	[133]
10Ni/CNTs-SiO ₂ fibers	T = 450 °C S/E = 9 %C ₂ H ₅ OH = 10%	2.6	100% after 22 h	1.5	
Pt@HBZ (HB zeolite)	T = 350 °C S/E = 4 %C ₂ H ₅ OH = 4%	3.4	100% after 15 h	0.23	[134]
Pt-B (B zeolite)	T = 350 °C S/E = 4 %C ₂ H ₅ OH = 4%	3.4	60% after 15 h	0.46	
2.5Co/hydroxyapatite	T = 500 °C S/E = 6 %C ₂ H ₅ OH = 4.1%	2.2	60% after 5 h	17	[135]
5Co/hydroxyapatite	T = 500 °C S/E = 6 %C ₂ H ₅ OH = 4.1%	2.2	40% after 5 h	19	
7.5Co/hydroxyapatite	T = 500 °C S/E = 6 %C ₂ H ₅ OH = 4.1%	2.2	30% after 5 h	20	
20Ni/Attapulgite	T = 700 °C S/E = 3 %C ₂ H ₅ OH = 12.6%	5.1	75% after 50 h	0.25	[136]
20Ni/5Mg-Attapulgite	T = 700 °C S/E = 3 %C ₂ H ₅ OH = 12.6%	5.1	85% after 50 h	0.23	
20Ni/10Mg-Attapulgite	T = 700 °C S/E = 3 %C ₂ H ₅ OH = 12.6%	5.1	98% after 50 h	0.047	
20Ni/20Mg-Attapulgite	T = 700 °C S/E = 3 %C ₂ H ₅ OH = 12.6%	5.1	87% after 50 h	0.097	
10Ni/20Pt-CeO ₂	T = 600 °C S/E = 5 %C ₂ H ₅ OH = 15.7%	18.2	100% after 120 h	0.0016	[137]
Pd _{0.01} Zn _{0.291} Mg _{0.7} Al ₂ O ₄	T = 450 °C S/E = 3 -	3.1	100% after 30 h	0.00017	[138]
La _{0.7} Ce _{0.3} Ni _{0.7} Fe _{0.3} O ₃	T = 500 °C S/E = 4 -	1.2	98% after 50 h	0.07	[139]
2.5Pt-1Cu@SiO ₂	T = 400 °C S/E = 4 -	2.9	100% after 30 h	0.33	[140]
2.5Pt@SiO ₂	T = 400 °C S/E = 4 -	2.9	70% after 30 h	0.60	
2.5Pt-1Cu/SiO ₂	T = 400 °C S/E = 4 -	2.9	80% after 30 h	0.79	
10Ni/17CeO ₂ ZrO ₂ 5La ₂ O ₃	T = 500 °C S/E = 3 %C ₂ H ₅ OH = 5%	10.1	86% after 4 h	12	[141]
10Ni/ZrO ₂ 5La ₂ O ₃	T = 500 °C S/E = 3 %C ₂ H ₅ OH = 5%	10.1	57% after 4 h	37	
1Rh/17CeO ₂ ZrO ₂ 5La ₂ O ₃	T = 500 °C S/E = 3 %C ₂ H ₅ OH = 5%	10.1	92% after 4 h	0.58	
1Rh/ZrO ₂ 5La ₂ O ₃	T = 500 °C S/E = 3 %C ₂ H ₅ OH = 5%	10.1	68% after 4 h	5.2	
Oxidative steam reforming of ethanol					
1Pt3Ni/CeO ₂ -SiO ₂ Cerium precursor: nitrate	T = 500 °C S/E = 4 O ₂ /E = 0.5 %C ₂ H ₅ OH = 10%	12.3	59% after 100 h	0.0030	[37]
1Pt3Ni/CeO ₂ -SiO ₂ Cerium precursor: ammonium nitrate	T = 500 °C S/E = 4 O ₂ /E = 0.5 %C ₂ H ₅ OH = 10%	12.3	60% after 100 h	0.0029	
1Pt3Ni/CeO ₂ -SiO ₂ Cerium precursor: acetyl acetate	T = 500 °C S/E = 4 O ₂ /E = 0.5 %C ₂ H ₅ OH = 10%	12.3	73% after 100 h	0.0014	
30Ni/CeO ₂ -ZrO ₂	T = 600 °C S/E = 9 O ₂ /E = 0.35	5.1	95% after 36 h	0.92	[43]

Table 1. Cont.

Catalyst ^a	Operative Conditions ^b	WHSV ^c (h ⁻¹)	X EtOH (%)	Carbon Formation Rate ^d (Multiplied for 1000)	Ref.
1Rh-30Ni/CeO ₂ -ZrO ₂	T = 600 °C S/E = 9 O ₂ /E = 0.35	5.1	85% after 36 h	0.45	
NiCo-MgAl (Ni+Co = 20 wt.%) Conventional synthesis	T = 550 °C S/E = 3 O ₂ /E = 0.5 %C ₂ H ₅ OH = 12.8%	91.6	100% after 100 h	7.7	[58]
NiCo-MgAl (Ni+Co = 20 wt.%) Microwave-assisted co-precipitation	T = 550 °C S/E = 3 O ₂ /E = 0.5 %C ₂ H ₅ OH = 12.8%	91.6	100% after 100 h	7	
NiCo-MgAl (Ni+Co = 20 wt.%) Sonication-assisted co-precipitation	T = 550 °C S/E = 3 O ₂ /E = 0.5 %C ₂ H ₅ OH = 12.8%	91.6	100% after 100 h	5.4	
1Pt-3Ni/CeO ₂ -SiO ₂ CeO ₂ /SiO ₂ ratio = 25	T = 500 °C S/E = 4 O ₂ /E = 0.5 %C ₂ H ₅ OH = 10%	4.1	100% after 100 h	0.0076	[60]
1Pt-3Ni/CeO ₂ -SiO ₂ CeO ₂ /SiO ₂ ratio = 30	T = 500 °C S/E = 4 O ₂ /E = 0.5 %C ₂ H ₅ OH = 10%	4.1	100% after 135 h	0.0012	
1Pt-3Ni/CeO ₂ -SiO ₂ CeO ₂ /SiO ₂ ratio = 40	T = 500 °C S/E = 4 O ₂ /E = 0.5 %C ₂ H ₅ OH = 10%	4.1	100% after 120 h	0.0065	
15Ni/MgAl ₂ O ₄	T = 500 °C S/E = 3 O ₂ /E = 0.5 %C ₂ H ₅ OH = 2.5%	9.2	80% after 28 h	22	
4Co11Ni/MgAl ₂ O ₄	T = 500 °C S/E = 3 O ₂ /E = 0.5 %C ₂ H ₅ OH = 2.5%	9.2	70% after 28 h	21	[94]
7.5Co7.5Ni/MgAl ₂ O ₄	T = 500 °C S/E = 3 O ₂ /E = 0.5 %C ₂ H ₅ OH = 2.5%	9.2	70% after 28 h	7.1	
11Co4Ni/MgAl ₂ O ₄	T = 500 °C S/E = 3 O ₂ /E = 0.5 %C ₂ H ₅ OH = 2.5%	9.2	60% after 28 h	6.7	
15Co/MgAl ₂ O ₄	T = 500 °C S/E = 3 O ₂ /E = 0.5 %C ₂ H ₅ OH = 2.5%	9.2	60% after 28 h	1.9	
4Co4Ni/MgAl ₂ O ₄	T = 500 °C S/E = 3 O ₂ /E = 0.5 %C ₂ H ₅ OH = 2.5%	9.2	60% after 28 h	0.11	
La _{0.6} Sr _{0.4} CoO _{3-δ}	T = 600 °C S/E = 3 O ₂ /E = 0.5 %C ₂ H ₅ OH = 4.4%	3.6	96% after 5 h	2.1	[142]
Mg ₂ AlNi ₃ H ₂ O _y	T = 260 °C S/E = 3 O ₂ /E = 1.6 %C ₂ H ₅ OH = 14.4%	81.9	100% after 75 h	0.31	[143]
NiCo-MgAl (Ni+Co = 20 wt.%) Conventional synthesis	T = 550 °C S/E = 3 O ₂ /E = 0.5 %C ₂ H ₅ OH = 12.8%	47.3	100% after 100 h	0.072	[144]
NiCo-5PrMgAl	T = 550 °C S/E = 3 O ₂ /E = 0.5 %C ₂ H ₅ OH = 12.8%	47.3	100% after 100 h	0.044	
NiCo-5CeMgAl	T = 550 °C S/E = 3 O ₂ /E = 0.5 %C ₂ H ₅ OH = 12.8%	47.3	100% after 100 h	0.049	
La ₂ Ce _{1.8} Ru _{0.2} O ₇ /La ₂ Zr ₂ O ₇	T = 400 °C S/E = 3 O ₂ /E = 0.6 %C ₂ H ₅ OH = 14.6%	28.1	100% after 100 h	0.0013	[145]
Mg _x La _{2-x} Ce _{1.8} Ru _{0.2} O ₇ /La ₂ Zr ₂ O _{7-δ}	T = 400 °C S/E = 3 O ₂ /E = 0.6 %C ₂ H ₅ OH = 14.6%	28.1	100% after 100 h	0.00021	
Ca _x La _{2-x} Ce _{1.8} Ru _{0.2} O ₇ /La ₂ Zr ₂ O _{7-δ}	T = 400 °C S/E = 3 O ₂ /E = 0.6 %C ₂ H ₅ OH = 14.6%	28.1	100% after 100 h	0.0011	
Ethanol dry reforming					
1Rh/CeO ₂	T = 700 °C CO ₂ /E = 1 -	18.5	88% after 65 h	0.0089	[63]
1Rh/CeO ₂	T = 700 °C CO ₂ /E = 3 -	18.5	100% after 65 h	0.0033	
2Rh/CeO ₂	T = 700 °C CO ₂ /E = 1 -	4.6	100% after 70 h	0.035	[82]
15Cu/CeO ₂	T = 700 °C CO ₂ /E = 1 %C ₂ H ₅ OH = 30%	6.2	75% after 90 h	0.0061	[98]
15Cu/ZrO ₂	T = 700 °C CO ₂ /E = 1 %C ₂ H ₅ OH = 30%	6.2	64% after 90 h	0.0093	
15Cu/CeO ₂ -ZrO ₂ Ce/Zr mol ratio = 1	T = 700 °C CO ₂ /E = 1 %C ₂ H ₅ OH = 30%	6.2	100% after 90 h	0.0045	
10Co/Al ₂ O ₃	T = 700 °C CO ₂ /E = 1 %C ₂ H ₅ OH = 20%	17.2	20% after 8 h	8.9	
2Ce-10Co/Al ₂ O ₃	T = 700 °C CO ₂ /E = 1 %C ₂ H ₅ OH = 20%	17.2	38% after 8 h	6.6	[123]
3Ce-10Co/Al ₂ O ₃	T = 700 °C CO ₂ /E = 1 %C ₂ H ₅ OH = 20%	17.2	50% after 8 h	4.7	
4Ce-10Co/Al ₂ O ₃	T = 700 °C CO ₂ /E = 1 %C ₂ H ₅ OH = 20%	17.2	37% after 8 h	5.1	

Table 1. Cont.

Catalyst ^a	Operative Conditions ^b	WHSV ^c (h ⁻¹)	X EtOH (%)	Carbon Formation Rate ^d (Multiplied for 1000)	Ref.
5Ce-10Co/Al ₂ O ₃	T = 700 °C CO ₂ /E = 1 %C ₂ H ₅ OH = 20%	17.2	34% after 8 h	5.2	
10Co/Al ₂ O ₃	T = 700 °C CO ₂ /E = 1 %C ₂ H ₅ OH = 20%	17.2	50% after 72 h	0.12	[124]
3La10Co/Al ₂ O ₃	T = 700 °C CO ₂ /E = 1 %C ₂ H ₅ OH = 20%	17.2	30% after 72 h	0.078	
10Ni/SiO ₂ -Al ₂ O ₃	T = 750 °C CO ₂ /E = 1.4 -	1.8	97% after 10 h	2.8	[146]
10Ni/ Al ₂ O ₃ calcined at 500 °C	T = 700 °C CO ₂ /E = 3 -	36.9	100% after 4 h	5.5	
10Ni/ Al ₂ O ₃ calcined at 600 °C	T = 700 °C CO ₂ /E = 3 -	36.9	100% after 4 h	6.7	[147]
10Ni/ Al ₂ O ₃ calcined at 700 °C	T = 700 °C CO ₂ /E = 3 -	36.9	100% after 4 h	9.7	

Note: ^a The metal or oxides loadings are intended for the weight of the catalyst; ^b all the tests were performed at atmospheric pressure; ^c refers to the ethanol mass flow-rate; ^d $g_{\text{coke}} \cdot g_{\text{catalyst}}^{-1} \cdot g_{\text{carbon, fed}}^{-1} \cdot h^{-1}$.

3. Oxidative Biomethanol Steam Reforming

Methanol is actually an attractive feedstock for reforming processes. It can be obtained from renewable and fossil sources [148], including biomass and CO₂, thus offering a pathway to a sustainable carbon-neutral cycle [149]. It can be easily converted to hydrogen via the (oxy-) reforming processes, and the resulting gas mixture, without a water-gas shift unit [150], can be directly used in high-temperature proton exchange membrane fuel cells (Figure 8), or [151] after purification steps in low-temperature polymer electrolyte membrane (PEM) fuel cells [152].

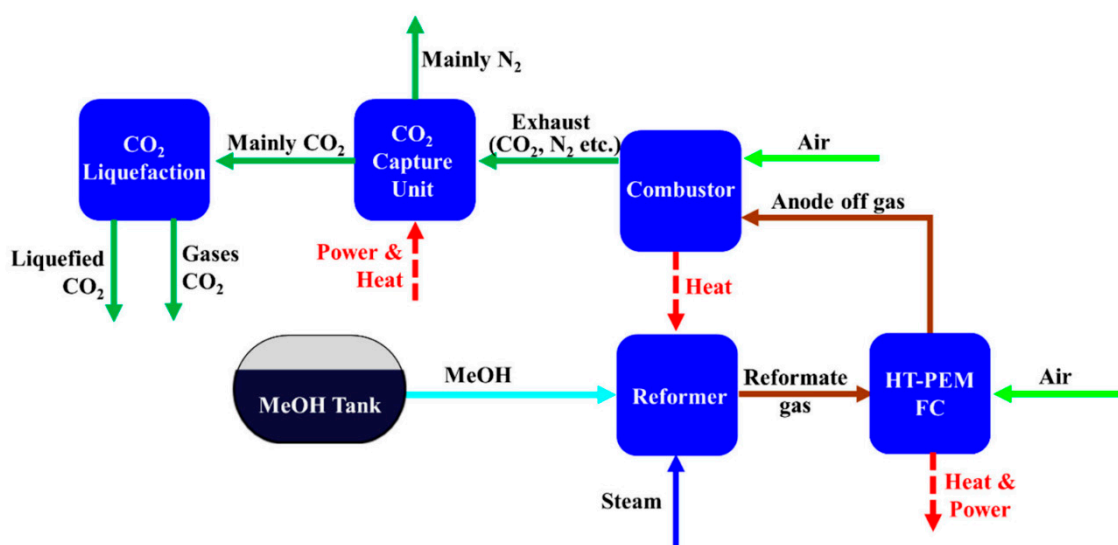
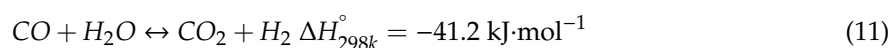
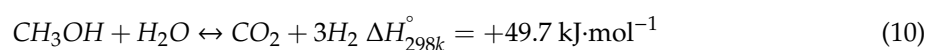
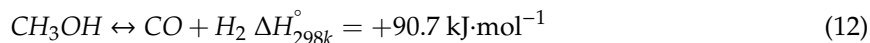


Figure 8. Block diagram of MSR-based system [150].

Many advantages were identified for using methanol for reforming processes. The molecule contains only one C atom, thus the absence of the C-C bond prevents the formation of a series of by-products. During the reforming processes [153], its reforming temperatures are relatively low; moreover, its tendency to form coke is lessened due to the high H/C ratio [154]. Methanol steam reforming (MSR) can be described by the following chemical reactions [155]:





The MSR reaction is endothermic and takes place with an increase in the number of moles; on the contrary, the water–gas shift reaction is exothermic and proceeds without a variation in the number of moles.

In this section, the results of selected studies published in the last five years on methanol (oxy-) steam reforming are reported. In the first paragraph, recent studies on the most-diffused active phases in MSR will be discussed. In the second section, comparative studies on the effects of the support will be reported. In the third section, the effects of promoters will be discussed, while theoretical and simulation studies, as well as non-conventional reactor configurations, will be reported in the fourth section. Finally, a selection of recent articles devoted to the oxidative steam reforming of methanol will be proposed. The paper distribution as a function of the active phase in the bibliographic survey reveals that copper is the preferred metal in methanol reforming; however, noble metals such as gold, platinum, and palladium are also used (Figure 9).

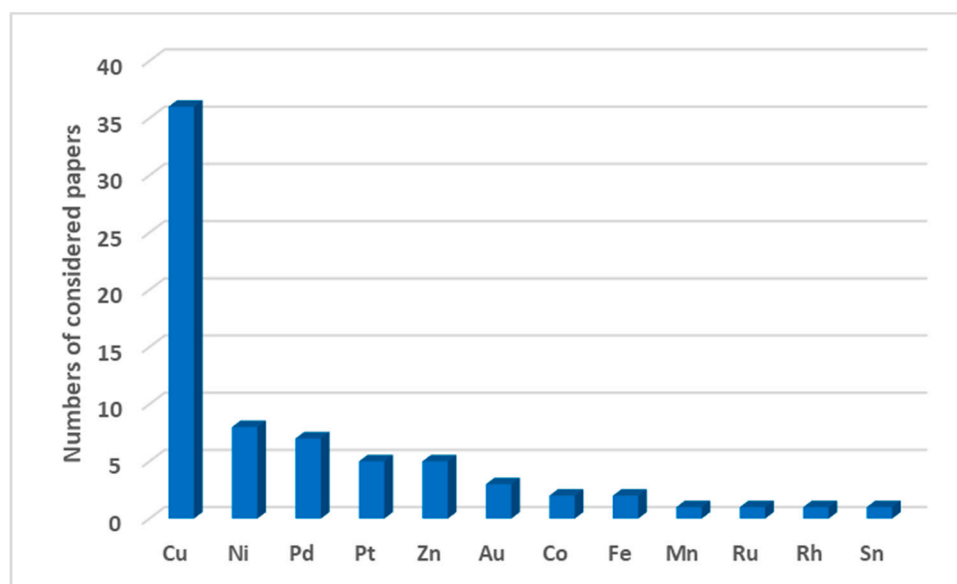


Figure 9. Number of considered papers as a function of the active phase analyzed for the methanol reforming.

3.1. The Influence of the Active Phase

As previously stated, in this section, the main results of a selection of articles on the effects of the active phase are reported. Most of them study copper-based catalysts, while only two cases are based on noble metal catalysts, palladium, or platinum.

Tonelli et al. investigated the stability of copper supported on ceria in MSR [156]. The ceria support was prepared by precipitation method with ammonium hydroxide from a solution of cerium (III) nitrate, while the catalyst was obtained by incipient wetness impregnation of the support with a copper (II) nitrate solution. The MSR tests were carried out on the catalyst, without reduction, at atmospheric pressure, at three temperatures (260, 280, and 300 °C), with a gaseous mixture of methanol, water, and nitrogen. The total flow rate was 82 mL·min⁻¹, with a methanol molar percentage of 5% and a H₂O/CH₃OH molar ratio equal to 1.2, while the catalyst weight was 300 mg. The activity was evaluated under steady-state conditions during a time-on-stream of 60 h and under shutdown–start-up operation, under inert conditions. In all experiments, the initial methanol conversion was higher than 80% and the selectivity to hydrogen was 100%; however, the activity decreased with the time-on-stream. In the case of steady-state conditions, the conversion losses were 76% at 300 °C, 78% at 280 °C, and 67% at 260 °C after 3000 min in reaction, while the catalyst was regenerated by air treatment at 400 °C.

For the discontinuous mode, the initial conversion and conversion until 500 min were the same as that obtained under the continuous regime. Moreover, after the stop period, the activity was recovered and self-activation occurred. The X-ray photoelectron spectroscopy (XPS) spectra suggested that the deactivation was mainly attributed to the adsorption of carbonate or formate species, which can be desorbed under inert flow or air burning. The Cu 2p XPS spectra sample after reduction and after inert treatments showed a decreased Cu surface content, which could be due to the Cu migration out of the ceria lattice or to the redispersion of the Cu particles; moreover, an overreduction of ceria may have also occurred. The effect of Cu loading (Cu = 7, 10, or 15 at%) on $\text{Ce}_x\text{Zr}_{1-x}\text{O}_2$ ($x = 0.4, 0.5, 0.6, 0.7,$ and 0.8) solid solutions was investigated by Das et al. [157]. The catalytic activity tests were performed in the temperature range of 200–330 °C, at atmospheric pressure, with a steam/methanol ratio of 1.1 (mol/mol), using nitrogen (23.5 mL min^{-1}) as the carrier and internal standard at a gas hourly space velocity (GHSV) of $40,000 \text{ h}^{-1}$. The results showed that the most-active catalysts had a Ce/Zr ratio equal to 0.6 and Cu loading of 10 and 15 at%; the MSR behaviour was found to be sensitive to the pretreatment, as evident in the case of the 10 at%Cu/ $\text{Ce}_{0.6}\text{Zr}_{0.4}\text{O}_2$ and 15 at%Cu/ $\text{Ce}_{0.6}\text{Zr}_{0.4}\text{O}_2$ catalysts, which perform better without pretreatment for the former and in the regenerated form for the latter. The time-on-stream activity tests showed a constant decrease of the CH_3OH conversion over 50 h for both 10 at%Cu/ $\text{Ce}_{0.6}\text{Zr}_{0.4}\text{O}_2$ and 15 at%Cu/ $\text{Ce}_{0.6}\text{Zr}_{0.4}\text{O}_2$ catalysts; the XPS analysis showed that the surface atomic ratio of copper decreased from 5.9% before the activity tests to 1.4% after the activity test, demonstrating that the formation of reduced Cu is accompanied by sintering; moreover, carbon formation also occurred. These results suggested that the formation of large aggregates of copper covered with coke could be responsible for the loss in activity. After the regeneration, these aggregates break into a mixture of oxidized (Cu^{2+}) and reduced (Cu^0 and Cu^+) copper species and the catalysts recover the activity, suggesting a correlation between the activity and different proportions of copper components in the various forms of these catalysts. Deshmane et al. studied the effect of Cu loading (Cu = 5–20 wt.%) on high surface area MCM-41 prepared by one-pot synthesis [158]. The Cu-MCM-41 catalysts were reduced before the catalytic activity tests with 4% hydrogen in argon at 550 °C for 5 h. The tests were carried out at atmospheric pressure with a mixture $\text{CH}_3\text{OH}/\text{H}_2\text{O}$ (molar ratio = 1:3) at a GHSV of 2838 h^{-1} in the temperature range of 200–350 °C. The results showed that the methanol conversion increased with the increase of the Cu loading until 15 wt.% for Cu-MCM-41, which showed $\approx 89\%$ conversion, 100% hydrogen selectivity, and 0.8% CO selectivity at 300 °C. A further increase of copper loading was detrimental; methanol conversion decreased to about 77% when the Cu loading was 20 wt.%. This result was attributed to the decrease in catalysts' surfaces area leading to a decrease in Cu dispersion. The time-on-stream test was carried out on 15wt.% Cu-MCM-41 and 20wt.% Cu-MCM-41, with the latter showing strong resistance to deactivation at 48 h of reaction, suggesting that the use of a high surface area MCM-41 support significantly enhanced the stability of Cu-based catalysts. The thermogravimetric analysis of the spent catalysts showed the presence of $\sim 1.3\%$ and $\sim 2.1\%$ carbon for 15% Cu-MCM-41 and 20% Cu-MCM-41 catalysts, respectively. Xu et al. studied the effect of the preparation method on the catalytic activity of Cu-based composite oxide catalysts for MSR [159]. Two catalyst were prepared, the first (Cu-ZnO- Al_2O_3 - ZrO_2 - Ga_2O_3 with Cu/Zn/Al/Zr/Ga = 14.9:30.9:3.9:10.8:1.9 mass ratio) by urea co-precipitation and active carbon co-nanocasting technique, and the other (Cu-ZnO- Al_2O_3 - ZrO_2 - Ga_2O_3 with Cu/Zn/Al/Zr/Ga = 13.3:28.2:3.9:10.0:1.8 mass ratio) by conventional co-precipitation method. The catalytic activity tests were performed at atmospheric pressure, with a methanol solution ($\text{CH}_3\text{OH}/\text{H}_2\text{O} = 1:1$ molar ratio), a liquid flow rate of $0.03 \text{ mL}\cdot\text{min}^{-1}$, and a $F_{\text{reactant}}\cdot W_{\text{cat}}^{-1} = 6000 \text{ mL}\cdot\text{g}_{\text{cat}}^{-1} \text{ h}^{-1}$. The results highlighted the better performance of the catalyst obtained with the active carbon co-nanocasting technique in terms of methanol conversion, hydrogen selectivity, and turnover frequency (TOF) values; moreover, no CO formation was reported. This trend was also confirmed in the stability tests carried out at 275 °C for 70 h, which showed a slight deactivation for the catalysts prepared with the active carbon co-nanocasting technique, while a continuous deactivation occurred in the other case. This result was attributed to the smaller Cu particle size distribution and higher metal-support interaction obtained with the active carbon co-nanocasting

technique. Moreover, the temperature-programmed oxidation (TPO) profiles of this catalyst after the stability test showed a peak at 252 °C and a shoulder at 451 °C, which were assigned to the deposition of amorphous carbon. The TPO of the catalysts obtained by conventional co-precipitation method after the stability test showed two peaks at 411 and 657 °C; the second one was attributed to the formation of graphitic coke, which is more stable and oxidizable only at high temperatures. Thattarathody and Sheintuch investigated the kinetic and dynamic behaviour of MSR on a CuO/ZnO/Al₂O₃ commercial catalyst at various steam-to-carbon ratios (S/C = 0, 0.5, 1), in a steady state and with temperature ramping conditions (140–300 °C) [160]. High activity was observed above 200 °C; moreover, rate oscillation was observed under isothermal conditions at a steam-to-carbon ratio equal to 1, as evident in the volumetric product compositions shown in Figure 10.

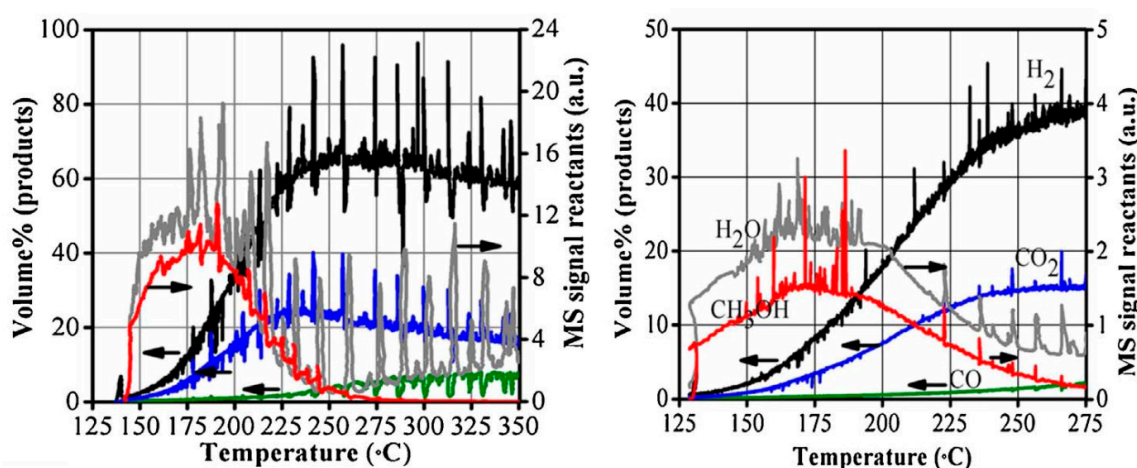


Figure 10. Comparison of product compositions during methanol steam reforming (S/C = 1) with an Ar flow of 10 mL/min (left) and 50 mL/min (right) [160].

After the tests, scanning TPO experiments were carried out to evaluate the amount of coke produced with the three different steam-to-carbon ratios (0, 0.5, and 1.0), obtaining 0.0187, 0.017, and 0.018 g of carbon per g of catalyst, respectively. Bagherzadeh et al. studied the effect of the exposition of CuO/ZnO/Al₂O₃ catalysts prepared by hydrothermal and co-precipitation methods for glow-discharge plasma for 45 min at 1000 V in MSR [161]. The catalytic activity tests were carried out in the temperature range of 180–300 °C, at a GHSV of 10,000 cm³·g_{cat}⁻¹·h⁻¹; the volumetric flow rate of the argon carrier gas was set on 66.7 cm³·min⁻¹ and the H₂O/CH₃OH molar ratio was approximately equal to 1.5. The characterization results demonstrated the benefits of coupling the co-precipitation method with glow-discharge plasma. X-ray diffraction (XRD) patterns highlighted the better dispersion of CuO (111) and another crystallite facet. Moreover, the SEM micrographs showed a more uniform distribution of isomorph particles, which had a smaller particles size and better surficial morphology, and the BET analysis demonstrated a higher specific surface area for the sample obtained by co-precipitation and following treatment with plasma. Accordingly, the results of the catalytic activity tests showed higher methanol conversion and better selectivity for the catalyst prepared by plasma-assisted co-precipitation method. For example, the methanol conversion and CO selectivity at 240 °C were 95% and 0.24%, respectively; in addition, the time-on-stream test showed no significant deactivation over 900 min of reaction. Ajamein et al. studied the effect of fuel type (sorbitol, propylene glycol, glycerol, diethylene glycol, or ethylene glycol) in the preparation of CuO/ZnO/Al₂O₃ nanocatalysts obtained by microwave-enhanced combustion method for MSR [162]. The catalytic activity tests were carried out in the temperature range of 160–300 °C, with a methanol/water ratio equal to 1.5. The results showed that the best performance was related to the use of ethylene glycol as fuel in the preparation of the catalyst. The characterization results demonstrated that sorbitol led to the formation of copper oxide species that were more crystalline in structure and assured a lower

dispersion of crystallite active sites, especially the Cu(111) facet. The use of ethylene glycol resulted in a homogeneous morphology and narrow particles size distribution (the average surface particle size was about 265 nm). The catalytic activity tests highlighted the better performance of the catalyst prepared with the assistance of ethylene glycol, which showed total methanol conversion at 260 °C, with a negligible CO selectivity. The stability tests of the catalysts obtained by sorbitol and propylene glycol showed total conversion during the first 600 min and a considerable drop over a further 800 min. On the other hand, no deactivation occurred with the catalyst prepared by ethylene glycol. Among the polyol used, sorbitol had the highest polarity, facilitating the growth of Zn (002) crystals as the polar facet of zinc crystallites, improving the carbon monoxide formation. A comparative study on the use of different active metals supported on M-MCM-41 (M: Cu, Co, Ni, Pd, Zn, and Sn), prepared by one-pot hydrothermal procedure, was proposed by Abrokwhah et al. [163]. The activity tests were carried out under the same conditions previously reported [158], highlighting the best performance of the Cu-based catalyst, which showed methanol conversion of 68%, hydrogen selectivity of 100%, and CO selectivity of 6% at 250 °C. On the other hand, PdMCM-41 and Ni-MCM-41 catalysts showed reduced activity for the water–gas shift reaction, resulting in higher CO selectivity. The stability tests were carried out at 300 °C for 40 h; the Cu-MCM-41 catalyst displayed an initial increase in the conversion with time due to the unsteady state; thereafter, the conversion stabilized at $\approx 74\%$ and no apparent deactivation occurred with a further 30 h of reaction. Except for Cu-MCM-41 and Co-MCM-41, all the other catalysts showed a decreasing trend for methanol conversion, which was attributed to coking and sintering. The thermogravimetric analysis differential scanning calorimeter (TGA-DSC) thermograms showed a nominal (absolute) 0.25%–0.96% coke formation between 400 and 570 °C that was attributed to the formation of amorphous and graphitic carbon. TPD studies on cobalt-manganese oxides demonstrated that the reaction paths of adsorbed methanol lead to decomposition to CO and H₂, as well as formation of stable surface formates, which decompose at higher temperatures to CO₂ and H₂ [164]. Li et al. investigated the catalytic activity of Mn-, Fe-, Co-, Ni-, Cu-, and Zn-based catalysts in the methanol, acetic acid, and acetone steam reforming [165]. The activity tests for MSR were performed with a steam-to-carbon ratio equal to 5 and a liquid hourly space velocity (LHSV) of 12.7 h⁻¹ at atmospheric pressure, in the temperature range of 200–500 °C. The results showed that Mn-, Fe-, and Zn-based catalysts were not active in MSR due to the low ability to break the chemical bonds or to activate the steam. On the contrary, Cu- and Co-based catalysts were both active; however, Co promoted methanol decomposition, showing higher CO selectivity. The supported metals showed different catalytic behaviour with respect to the unsupported one; for example, in MSR, the unsupported Cu catalysts showed lower stability than the supported one, which rapidly deactivated (Figure 11).

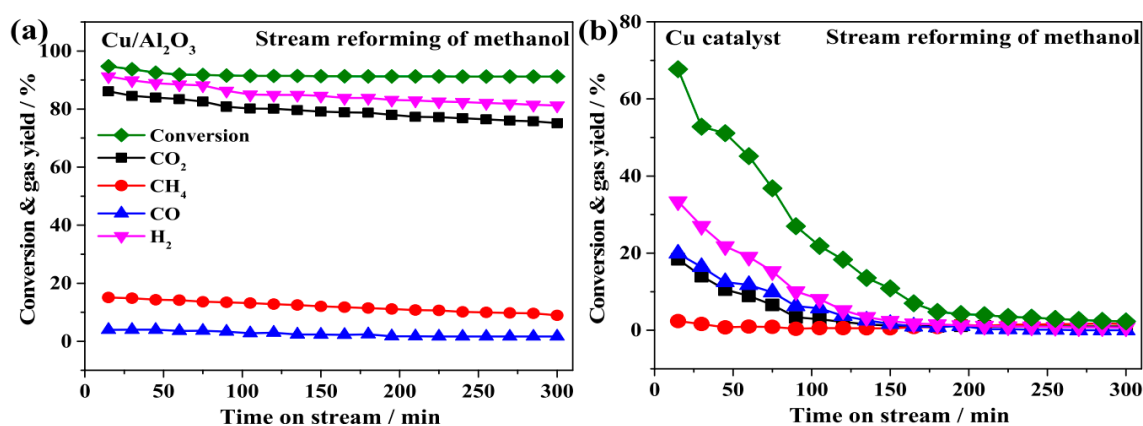


Figure 11. Time-on-stream tests (MSR) for Cu/Al₂O₃ (a) and Cu (b) catalysts. Reaction conditions: S/C = 1.5; T = 500 °C; LHSV = 12.7 h⁻¹; P = 1 atm [165].

It is worthwhile noting that the TPO profiles and the thermogravimetric analysis of the catalyst used in acetic acid and acetone steam reforming demonstrated the formation of a large amount of coke for all the catalysts. Conversely, carbon formation was really low in the case of MSR. Maiti et al. investigated the catalytic activity towards the MSR of a series of copper-ion-substituted CuMAl_2O_4 ($M = \text{Mg, Mn, Fe and Zn}$) spinels prepared via single-step solution combustion synthesis [166]. The catalytic activity tests were carried out in the temperature range of 200–330 °C, under atmospheric pressure, with a steam/methanol ratio of 1.1 (molar basis), at a GHSV of 30,000 h^{-1} . Among the studied catalysts, the $\text{Cu}_{0.1}\text{Fe}_{0.9}\text{Al}_2\text{O}_4$ was the most active, showing methanol conversion of $\approx 98\%$ and CO selectivity of $\approx 5\%$ at 300 °C. On the other hand, the analogous impregnated catalyst, 10 at%CuO/FeAl₂O₄, showed less catalytic activity. The time-on-stream tests showed a decrease of the methanol conversion from 50% to 35% over 20 h of reaction at a temperature of 250 °C. The evaluation of the XRD and high-resolution transmission electron microscopy (TEM) analysis showed the formation of a stable spinel phase containing substitutional copper ions, which stayed intact after 20 h of reaction. The decrease in the activity after the time-on-stream tests was attributed to the sintering of the catalyst, which also caused lowering of the copper surface concentration. Cu-Ni-Al spinel catalysts prepared by solid-phase method using copper hydroxide, nickel acetate, and pseudoboehmite as starting materials were studied by Qing et al. [167]. The results showed that Cu-Ni-Al spinels with molar ratios of 1:0.05:2 and 1:0.05:3 can be prepared at a calcination temperature ranging from 900 to 1100 °C; the spinel content increased with the calcination temperature. The catalytic performance was related to the calcination temperature of the catalyst, so the catalyst obtained at 1000 °C showed the best catalytic performance. The stability tests carried out at 255 °C and a weight hourly space velocity (WHSV) of 2.18 h^{-1} showed no significant deactivation after 300 h; however, the diffractograms of the spent catalysts showed a shift of the peaks to high angles, confirming a gradual release of Cu during the reaction process. Luo et al. developed nano- $\text{Ni}_x\text{Mg}_y\text{O}$ solid-solution oxides prepared by impregnation, hydrothermal treatment, and co-precipitation as catalysts for MSR [168]. The catalytic activity tests were carried out under atmospheric pressure with a mixture of water and methanol (molar ratios of 1 or 3) and a GHSV of 92,000 $\text{mL}\cdot\text{g}_{\text{cat}}^{-1}\cdot\text{h}^{-1}$ or 114,000 $\text{mL}\cdot\text{g}_{\text{cat}}^{-1}\cdot\text{h}^{-1}$, at four different reaction temperatures (400, 500, 600, and 700 °C). The best performance was obtained with the catalyst prepared by hydrothermal method, with methanol conversion of 97.4% and a hydrogen yield of 58.5%, which was maintained for 20 h at a steam-to-carbon ratio of 3. This superior catalytic activity was attributed to the nanoscale active phase and to the high micropore volume; moreover, the excellent anticarbon deposition capability was attributed to the formation of the solid solution, which was able to prevent the agglomeration of nickel particles, and to the high basicity of the magnesium oxide supports, which supplied oxygen from the adsorbed CO₂ and H₂O to burn off the amorphous carbon. Zeng et al. reported a study on the preparation and use of Pd/ZnO-based catalysts in MSR, which were synthesized by reduction with NaHB₄ from Pd ions supported on a zeolitic imidazolate framework-8 (ZIF-8) [169]. The activity tests were carried out with various methanol/water molar ratios ranging from 1 to 6, in the temperature range 250–380 °C, with a flow rate from 0.01 to 0.2 $\text{mL}\cdot\text{min}^{-1}$. The activity of two catalysts that were synthesized by reduction and calcined at 400 and 450 °C, respectively, was compared to that of two catalysts obtained by wet impregnation method and to that of a commercial CuO/ZnO/Al₂O₃ catalyst. The best performance in terms of methanol conversion (97%), CO₂ selectivity (86.3%), and stability after a time-on-stream test of 50 h was obtained with the catalyst prepared by reduction and calcined at 450 °C. This result was attributed to the larger surface area, the evenly distributed PdZn alloy activity sites, and abundant oxygen vacancies. A reaction mechanism was also suggested, in which the PdZn surface stabilizes the intermediate methyl formate and could provide a benefit to the adsorption of hydrogenated O-anchored species, such as HCOOH, H₂CO, and CH₃OH. Defects are able to alter the adsorption characteristics of these molecules, promoting dissociation; moreover, surface oxygen can enable water dissociation at low coverage, which is the key kinetic step in water splitting. Finally, the CO formation can be disfavored by the oxygen vacancies in the ZnO support. Claudio-Piedras et al. investigated the effect of the platinum precursor in Pt nanocatalysts supported

on CeO₂ nanorods in MSR [170]. The catalysts were prepared by impregnation with Pt(NH₃)₄(NO₃)₂, (CH₃-COCHCO-CH₃)₂Pt, and H₂PtCl₆·6H₂O. The best performance was obtained with the catalysts prepared from the nitrate precursor, showing higher hydrogen yield and methanol conversion ascribable to the improved redox process, as well as to the better Pt dispersion on the surface of ceria, which promoted the water–gas shift (WGS) reaction at moderate temperatures. The time-on-stream tests highlighted the high stability of all the catalysts, with no significant deactivation observed after 24 h of reaction.

3.2. The Role of the Support

In this section, some studies on the effect of the support on the catalytic behaviour are reported, focusing on the preparation method, the effect of the precursors, and on the type of phase; in one article, a comparative study on the use of different supports is also discussed.

Barrios et al. prepared and tested two series of palladium catalysts in the MSR reaction, supported on ZnO-CeO₂ nanocomposites (Zn/Ce = 0.5, 1 or 2) and obtained by co-precipitation using oxalate or carbonate precursors [171]. For comparison, a series of catalysts were prepared by impregnation of mixed oxides, obtained through the incorporation of ZnO onto ceria by incipient wetness impregnation with two nominal loadings (3.5 wt.% and 11 wt.%), and by impregnation of ceria and ZnO with palladium acetate. The catalytic activity tests were carried out in the temperature range of 125–350 °C, with a gas mixture of CH₃OH/H₂O (1/1) diluted in He (16 vol.%) at a GHSV of 71,500 cm³h⁻¹g⁻¹ and a W/F⁰_{CH₃OH} ratio, defined as the catalytic mass normalized for the methanol volumetric flow rate of 174 g·h·m_{CH₃OH}⁻³. XPS spectroscopy and the CO chemisorption experiments highlighted the formation of bulk and surface PdZn alloys in the ternary catalysts. The 2 wt.%Pd/CeO₂ catalyst caused CO decomposition at 250 °C and reversed the water–gas shift at higher temperatures. The MSR occurred in all catalysts in which ZnO was present; however, the catalysts prepared by impregnation of the supports obtained by carbonate co-precipitation showed the highest CO₂ selectivity due to the better dispersion of the ZnO phase. The time-on-stream tests carried out over 50 h of reaction showed that in the case of Pd/CeO₂, the methanol conversion (80%) and the CO₂ selectivity (8%) remained constant after 18 h on stream. The Pd/ZnO sample displayed a continuous decrease of methanol and water conversion; however, CO₂ selectivity remained almost constant at 90%. Both nanocomposite-supported Pd catalysts showed deactivation during the first 24–28 h, followed by stabilized methanol conversions of 53% and 40% for the Pd/ZnO–CeO₂ and Pd/ZnO/CeO₂ samples, respectively, with selectivity of 80%. The PdZn alloy formation seems to play a crucial role in preventing the methanol decomposition and in releasing hydrogen via inverse spillover, while the reforming reaction takes place mostly on the oxidized surface. Even though the nanocomposite-supported catalysts were less active and selective than the Pd/ZnO catalysts, they showed much more stability, so that the CeO₂ acted similarly to an “active dispersant of ZnO”. Ajamein et al. investigated the effect of the precursor type, ultrasound irradiation, and urea/nitrate ratio on the catalytic performance of CuO/ZnO/Al₂O₃ nanocatalysts prepared by ultrasound-assisted urea–nitrate combustion method in methanol steam reforming reaction [172]. The results showed that the use of boehmite precursor instead of aluminium nitrate reduces the crystallite size, increases the dispersion, and enhances the specific surface area of copper and zinc species. Comparing sonication and conventional mechanical mixing, the mixing of primary gel provided nanocatalysts with improved homogeneity. Moreover, the CuO and ZnO crystallite sizes and the specific surface areas increased with the urea/nitrate ratio. The best performance in the catalytic activity tests in term of methanol conversion and hydrogen yield were obtained with the catalyst prepared from boehmite with a urea/nitrate ratio equal to 1 obtained by ultrasound irradiation, due to the smaller crystallite sizes and to the highly dispersed particles. This catalyst was also subjected to a time-on-stream test at 240 °C for 1200 min, with a H₂/CH₃HO ratio of 1.5 at a GHSV of 10,000 cm³g⁻¹h⁻¹, showing a decrease in methanol conversion from 100% to 90%. Lin et al. reported the use of platinum atomically dispersed on α-molybdenum carbide for low-temperature (150–190 °C) aqueous-phase methanol reforming, with an average TOF of

18,046 moles of hydrogen per mole of platinum per hour [173]. The exceptional hydrogen production was attributed to the outstanding ability of α -MoC to induce water dissociation, and to the synergy between platinum and α -MoC in activating methanol with a 0.2 wt.%Pt/ α -MoC catalyst. DFT studies demonstrated that the α -MoC support is able to provide highly active sites for water dissociation, with an activation energy of 0.56 eV, thus offering abundant surface hydroxyls and accelerating the methanol-reforming reaction at the interface between Pt₁ and α -MoC. Moreover, the geometry of the well-dispersed Pt₁ maximizes the exposed active interface of Pt₁/ α -MoC and increases the density of active sites for the reforming reaction. In a more recent study, Cai et al. investigated Zn-modified Pt/MoC catalysts (Zn loading = 0–9.8%) prepared by temperature-programmed reaction method in low-temperature methane steam reforming [174]. The activity tests were performed with H₂O and CH₃OH at a molar ratio of 3:1, in the temperature range of 120–200 °C. The Zn doping favored the formation of α -MoC_{1-x} phase, enhancing the Pt dispersion and the interactions between α -MoC_{1-x} and Pt active sites. The 0.5Zn-Pt/MoC catalyst exhibited good performance in terms of hydrogen production, low CO selectivity, and good stability at 120 °C. However, at temperatures higher than 140 °C, the catalytic activity of this catalyst decreased during the initial stage of reaction, due to the sintering of Pt particles and to the change of α -MoC_{1-x} phase. A treatment with a 15 vol.% CH₄/H₂ gas at 590 °C for 2 h was able to increase the catalytic activity of the spent 0.5Zn-Pt/MoC catalyst; however, the deactivation of the catalyst was inevitable. Liu et al. investigated the effects of supports in Pt/In₂O₃/MO_x catalysts (MO_x = γ -Al₂O₃, MgO, Fe₂O₃, La₂O₃, or CeO₂) with Pt loading of 1 wt.% and In₂O₃ loading of 3 wt.% in MSR in the temperature range of 250–400 °C [175]. The catalytic activity tests were carried out in a flowing-type quartz tube (I.D. = 6.0 mm), at a GHSV of between 12,870 h⁻¹ and 38,610 h⁻¹, with a steam-to-carbon ratio of between 0.6 to 1.8. The activity tests showed that the prereduced 1Pt/3In₂O₃/CeO₂ catalyst exhibited the highest activity among the studied catalysts, with methanol conversion of 98.7%, hydrogen selectivity of 100%, and CO selectivity of 2.6% at 325 °C, with a steam-to-carbon ratio of 1.4 and a GHSV of 12,870 h⁻¹. These results were related to the active metal dispersion and enhanced redox properties associated with the strong interactions among Pt, In₂O₃, and CeO₂. Moreover, the 1Pt/3In₂O₃/CeO₂ catalyst showed good stability in the time-on-stream test over 32 h. Díaz-Pérez et al. studied the Cu-based catalysts supported on SiO₂, Al₂O₃–SiO₂, TiO₂ rutile, and TiO₂ anatase metal oxides for MSR [176]. The catalysts were prepared by wet impregnation with a loading of 20 wt.%, while the activity tests were carried out with a steam-to-methanol ratio of 1:1.5. The results showed that on highly acidic supports such as Al₂O₃–SiO₂, the methanol conversion decreased with the TOS due to carbon formation. On TiO₂ anatase, the catalytic activity and stability was significantly lower than that on TiO₂ rutile, probably due to the differences in adsorbate–surface binding on rutile and anatase. The catalyst supported on nanosized SiO₂ showed the highest catalytic activity and selectivity. Time-on-stream tests were performed for over 80 h of reaction at low and high pressures, and no deactivation occurred; however, metal sintering was observed by means of HRTEM and XRD. The high activity and selectivity of Cu/SiO₂ was attributed to the low acid site concentration. Tahay et al. compared the performance of cubic and hexagonal phases of ZnTiO₃ with TiO₂ and ZnO as catalyst supports in MSR [177]. The ZnTiO₃ phases were synthesized by sol–gel method, while copper was used as the active phase. The tests were carried out in the temperature range of 150–300 °C at a WHSV 1 h⁻¹ under atmospheric pressure, with a mixture of N₂/H₂O/methanol at a ratio of 6:2:1. The results of the activity test showed that the Cu/cubic-ZnTiO₃ catalyst exhibited high activity, high hydrogen selectivity, and low coke formation due to low–moderate acid sites in the cubic sample; moreover, the trend of methanol conversion at 300 °C is Cu/cubic-ZnTiO₃ > Cu/TiO₂ > Cu/hexagonal-ZnTiO₃. Time-on-stream tests showed a higher decrease of the methanol conversion of the ZnTiO₃ hexagonal-based catalyst compared to the cubic-based one at 42 h of reaction. The thermogravimetric analysis revealed the presence of three weight losses: the first one between 25 and 200 °C was attributed to the water elimination, the second between 200 and 400 °C to the low-temperature oxidation of the copper, while the weight loss after 400 °C was attributed to the coke burning. The amount of deposited carbon in the case

of Cu/cubic-ZnTiO₃ was negligible; thus, the deactivation was only attributed to the Cu sintering process. The coke resistance of the Cu/cubic-ZnTiO₃ catalyst could be related to the high CO₂/CO ratio, which reduces the CO disproportionation on the catalysts' surfaces.

3.3. The Effect of the Addition of Promoters

In this section, a selection of recently published articles on the effect of promoters on the catalytic activity in MSR is reported. The sequence is settled based on the kind of promoter.

Talkhonchek et al. studied the effect of the preparation method and the CeO₂ promotion effect on CuO/ZnO/Al₂O₃/ZrO₂-based nanocatalysts in the MSR reaction [178]. The catalysts were prepared by means of urea–nitrate combustion synthesis and homogeneous precipitation method; the catalytic activity tests were carried out at a temperature range of 200–300 °C under atmospheric pressure at a GHSV of 10,000 cm³g_{cat}⁻¹·h⁻¹, feeding a mixture of H₂O/MeOH with a ratio equal to 1.5. The XRD analysis and FESEM images showed that the homogeneous precipitation method and the CeO₂ addition improves the dispersion, decreases the particle size, decreases the relative crystallinity of CuO and ZnO species, and enhances the surface homogeneity. The activity tests showed that the catalyst obtained by homogeneous precipitation method was more active in terms of high methanol conversion and low CO selectivity. Moreover, the CeO₂ addition decreased the CO selectivity and reduced the methanol conversion. The stability test carried out on the ceria-promoted catalyst prepared by urea precipitation method showed no deactivation after 1200 min of time-on-stream. In fact, CeO₂ was able to oxidize the carbon deposited on the nanocatalyst's surface. Taghizadeh et al. investigated the activity of cerium-promoted copper-based catalysts synthesized via conventional and surfactant-assisted impregnation methods using KIT-6 as support in MSR [179]. The activity tests were carried out at atmospheric pressure, with a methanol-to-water molar ratio of $\frac{1}{2}$ and at a WHSV of 2 h⁻¹. The results demonstrated that the incorporation of cerium oxide improved the performance of the Cu/KIT-6-based catalysts due to the higher dispersion and to the smaller size of Cu particles; moreover, the surfactant-assisted impregnation enhanced the physiochemical properties of the resulting Ce-promoted catalysts. The catalyst prepared with this method showed methanol conversion of ≈92%, hydrogen selectivity of 99%, and negligible CO selectivity (0.9%) at 300 °C. These results were attributed to the presence of the CTAB surfactant, which hindered the metal species migration during the drying and decreased the sintering during the calcination. The time-on-stream tests highlighted the stability of the Ce-promoted catalysts, with no significant deactivation observed over 24 h of reaction time. Phongboonchoo et al. investigated the catalytic activities of Ce-Mg-promoted Cu/Al₂O₃ catalysts prepared by co-precipitation in MSR [180]. The activity tests were carried out with a methanol/steam ratio of 1.5, 1.75, or 2, diluted in He at a temperature range of 200–300 °C. The results showed that the methanol conversion and hydrogen yield were higher with the monpromoted catalysts (Cu_{0.3}Mg_{0.3}/Al₂O₃ and Cu_{0.3}Ce_{0.3}/Al₂O₃) than those without a promoter, probably due to the higher dispersion of copper species and to the strong interaction between copper and ceria, which lessened the catalyst reduction. Moreover, the performance of the bipromoter catalyst showed higher methanol conversion, higher hydrogen yield, and lower CO selectivity than the monpromoted catalyst. The increase in the catalytic activity was attributed to the formation of smaller Cu crystallites, improved copper dispersion, and lower reduction temperature. The effect of the steam-to-carbon ratio was also investigated, demonstrating that a lower CO selectivity was obtained with a ratio of 2. Moreover, in order to optimize the reaction conditions, a theoretical study was also performed via a face-centered central composite design response surface model (FCCCD-RSM). The analysis was carried out on four main factors (temperature, steam-to-carbon ratio, Cu weight percentage, and magnesium weight fraction: Mg/(Ce+Mg)) by building a matrix and varying each factor within the level of the other factors. The results were analyzed using the Design-Expert 7.0 software package (Stat Ease Inc., Minneapolis, MN, USA), using analysis of variance and the percentage contribution of each factor to the responses. At a 95% confidence interval, the optimal operating region for maximal methanol conversion (100%) and hydrogen yield in the range of 28.9–29.4%, as well as CO

selectivity of 0.16–0.18%, provided a copper level of 46–50 wt.%, a Mg/(Ce+Mg) yield of 16.2–18.0 wt.%, a temperature of 245–250 °C, and a steam-to-carbon ratio of 1.74–1.80 (Figure 12).

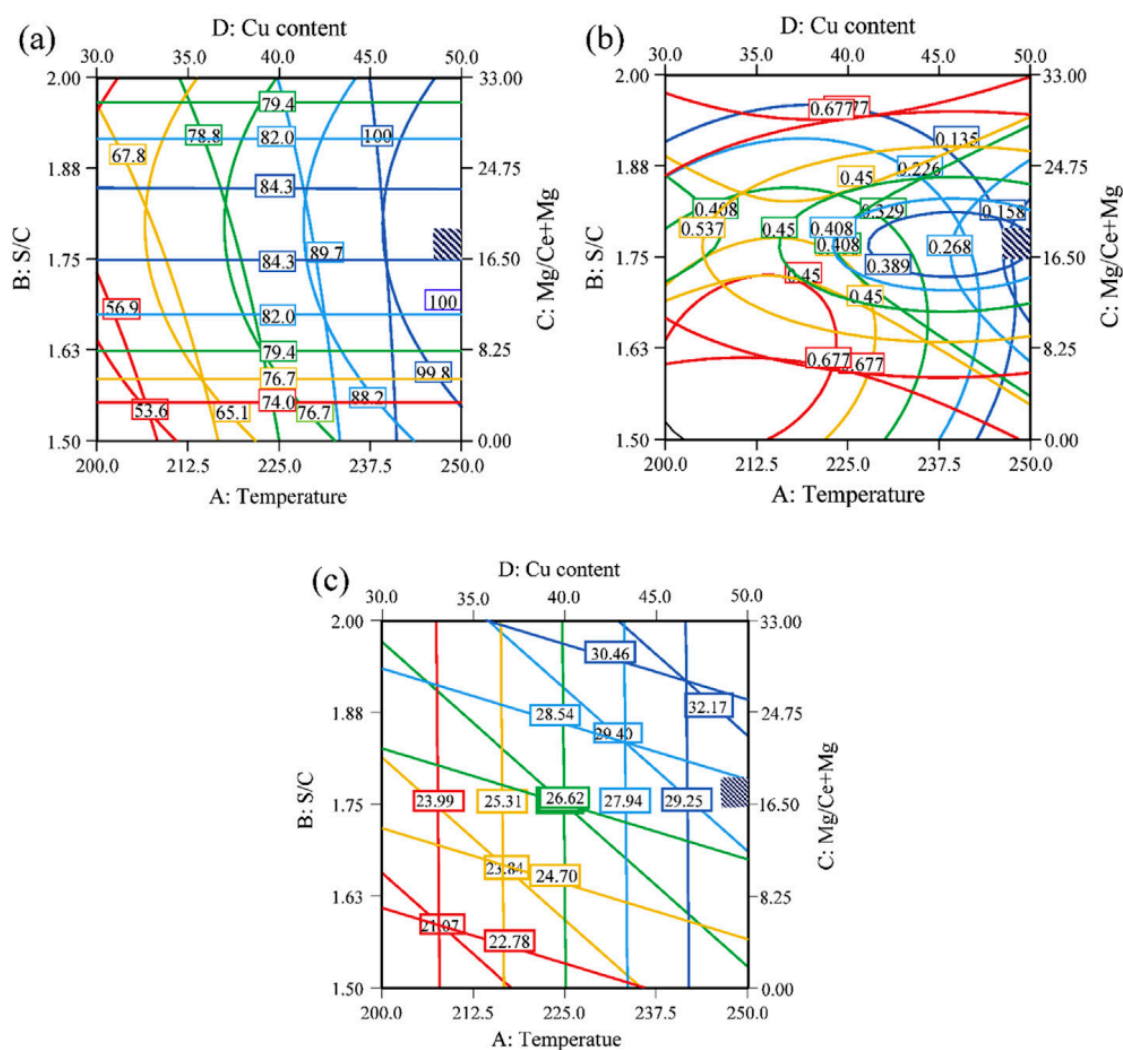


Figure 12. Contour plots for the optimal conditions for the methanol conversion (a); CO selectivity (b); H₂ yield (c) [180].

These results were compared to the catalytic activity of Cu_{0.5}Ce_{0.25}Mg_{0.05}/Al₂O₃ in a time-on-stream test of 72 h under the optimal operating parameters, showing complete methanol conversion and a CO selectivity of 0.14–0.16% with a hydrogen yield of 24–25%; furthermore, no deactivation occurred.

Hou et al. proposed Cu-Al spinel oxide as a sustained release catalyst for MSR, in which the surface modification of the spinel was performed with MgO [181]. The Cu-Al spinel with a Cu/Al atomic ratio equal to 1:3 was prepared by solid-phase method, where MgO was loaded by incipient wetness impregnation (loading = 0.9, 1.7, 3.6, and 9.5%); a reference catalyst 9.5%Mg/Al₂O₃ was also prepared. The catalytic tests were carried out with a methanol-to-water molar ratio of 0.46, the methanol WHSV was 0.98 h⁻¹, and the reaction temperature was 255 °C. The characterization results showed that the MgO strongly interacts with the Cu-Al spinel by changing the surface microstructure. Mg²⁺ cations were incorporated into the spinel structure, substituting a portion of Cu²⁺ in the lattice. The doped catalysts showed a higher reduction temperature, lower copper releasing rate, and smaller copper particle size. The addition of suitable amounts of magnesium oxide to the Cu-Al catalyst enhanced the catalytic activity and stability; the best performance was obtained with 1.7%Mg/CuAl.

The evaluation of coke formation on the spent catalysts demonstrated a correlation with the amount of the MgO loading. In the CO₂-TPD profiles, two oxidation peaks were found; the peak at 150–300 °C was attributed to the decomposition of formate, while the peak at 300–500 °C was attributed to the decomposition of carbonate. For the catalysts with low loading (≤ 1.7 wt.%), the low temperature peak was dominant; on the contrary, for the catalyst with high loading (9.5 wt.%), the high temperature peak was dominant. A correlation between the catalytic activity and the high temperature desorption peak was also found; thus, the lower activity of the catalysts with MgO loading higher than 1.7% was attributed to a coverage effect. The active copper was blocked by the dynamic formation of carbon deposits during the catalytic reaction. Moreover, lower Cu release rates were observed with the increase of MgO loadings and the Cu released was not able to sustain the catalytic activity; thus, fast deactivation was found for the 9.5% Mg/CuAl catalyst. Liu et al. investigated the use of CuOZnOxGa₂O₃-Al₂O₃ and CuOZnOxGa₂O₃-ZrO₂ catalysts (Ga wt.% = 0–12.4) prepared by sol-gel method in the MSR reaction [182]. The catalytic activity tests were performed at 250 and 275 °C at a GHSV of 2,200 h⁻¹, with a mixture CH₃OH/H₂O/N₂ in a 1:1:1.3 molar ratio. The characterization results showed that the addition of alumina and zirconia increased the specific surface area and modified the reduction temperature of the CuOZnOGa₂O₃ catalytic system. Zirconia promotion provided the highest reducibility and best performance in MSR for both studied temperatures. The introduction of Ga₂O₃ enhanced the hydrogen production rate but did not improve the stability of the CuZn system. The CuZn₃Ga₂O₃ZrO₂ catalysts showed higher stability. The hydrogen production rate at 275 °C after 44 h was 312 mL_{g_{cat}}⁻¹min⁻¹, with methanol conversion of 75%. The TPO and TG mass spectrometry analyses demonstrated the presence of negligible amounts of carbon deposits below 250 °C. Mohtashami and Taghizadeh studied ZrO₂-promoted Cu-ZnO/MCM-41 catalysts prepared by sol-gel impregnation and modified impregnation methods in the MSR reaction [183]. The modified impregnation method consisted of treating the MCM-41 support with acetic acid for 5 h at room temperature before drying and calcining. The catalytic tests were performed in the temperature range of 280–320 °C; at a WHSV of 1.08, 1.62, or 2.16 h⁻¹; and with a methanol-to-water molar ratio of 1:2. The inclusion of 2% ZrO₂ to the Cu-ZnO/MCM-41 catalyst increased the methanol conversion from 90.6 to 94.0% at 300 °C. The promoted catalyst prepared through the modified impregnation method showed the best performance, with methanol conversion of 97.8%, a hydrogen selectivity of 99.0%, CO selectivity of 0.4%, and also good stability. Reduced deactivation was observed within 81 h in the time-on-stream test. The evaluation of the amount of coke deposited on the catalyst's surface after the time-on-stream tests by thermogravimetric analysis showed a significant reduction of the coke formation in the zirconia-promoted catalysts. This performance was attributed to the positive effect of the acetic acid pretreatment on the support, which modified the MCM-41 surface through the generation of oxyl groups, which were able to prevent metal particle aggregation, decrease the metal particles size, and improve the dispersion and reduction behaviours of the CuO particles. Lu et al. investigated the effect of the lanthanum addition and the effect of nickel loading on different supported Ni-based catalysts [184]. The catalysts were prepared by co-precipitation wetness impregnation method; the activity tests were carried out at a GHSV of 10,920 h⁻¹, at atmospheric pressure, with a mixture of MeOH/H₂O (molar ratio = 3:1). The results demonstrated that the catalytic performance at low temperature for Ni-based catalysts can be enhanced by the addition of lanthanum, due to the formation of smaller and highly-dispersed NiO particles. The characterization results showed that lanthanum species are able to interact with nickel oxide and aluminum oxide to generate La-Ni or La-Ni-Al mixed oxides. The comparative study on the use of different supports showed that a weak interaction occurred between SiO₂ and NiO species, while with Al₂O₃, the NiAl₂O₄ spinel and separated NiO particles located on the outer surface were formed. The use of the MgO support generated the NiO-MgO solid solution, which decreased the amount of active nickel species. Azhena et al. studied the effect of Cu promotion in Pd/ZrO₂-based catalysts, along with the influence of the zirconia structure, in low-temperature MSR [185]. The catalysts were prepared by wet impregnation and the catalytic activity tests were carried out at atmospheric pressure with a steam-to-methanol ratio of 1.5, a contact

time $W_{\text{cat}}/F_{\text{CH}_3\text{OH}}^0 = 83 \text{ Kg}_{\text{cat}} \cdot \text{mol}^{-1} \text{ s}^{-1}$, and in the temperature range of 180–260 °C. The results showed that the use of monoclinic zirconia provides benefits both in terms of activity and selectivity; at the same time, the selectivity is also improved by the addition of Cu. These improvements were attributed to the enhanced dispersion of the metal phase on monoclinic zirconia and to the strong interaction between Pd and Cu. Liu et al. studied the catalytic behaviour of 1wt.%Pt/xIn₂O₃/Al₂O₃ catalysts ($x = 0\text{--}45 \text{ wt.}\%$) prepared by incipient wetness impregnation in the MSR reaction [186]. The catalytic activity tests were carried out under atmospheric pressure in the temperature range of 200–500 °C. The optimal performance was obtained with a reacting mixture of H₂O/CH₃OH (mole ratio = 1.4; flow rate = 1.2 cm³·h⁻¹) diluted in N₂ (flow rate = 30 cm³·min⁻¹), at a GHSV of 14,040 h⁻¹ and at 350 °C, with In₂O₃ loading of 30 wt.%. Under these conditions, the 1Pt/30In₂O₃/Al₂O₃ catalyst exhibited complete methanol conversion, high hydrogen selectivity (99.6%), and low CO selectivity (3.2%). The high activity was related to the intimate contact of Pt with partly reduced In₂O₃, which was hypothesized to be the active site of the reforming reaction. The performance of the 1Pt/30In₂O₃/Al₂O₃ catalyst was also compared to that of the 1Pt/30ZnO/Al₂O₃ catalyst in a time-on-stream test of 17 h; the higher activity and stability of 1Pt/30In₂O₃/Al₂O₃ was attributed to the enhanced dispersion of metallic Pt, and to the synergistic effect and strong interaction between Pt and In₂O₃, which facilitated the water activation, thus promoting the methanol reforming. Martinelli et al. investigated the effect of the sodium doping on supported Pt-based catalysts in methanol steam reforming [187]. The support was yttria-stabilized zirconia YSZ (Y/Z = 0.11) prepared by co-precipitation, while the catalysts were obtained by sequential incipient wet impregnation with a platinum salt precursor (Pt loading 2 wt.%) and sodium nitrate (Na loading 0.25, 0.5, 1, or 2.5 wt.%). The catalytic activity tests were carried out in a steady state under a feed stream containing 2.9% CH₃OH, 26.1% H₂O, 29.9% H₂, and 4.3% N₂ (balance He) at atmospheric pressure, at a GHSV of 381,000 h⁻¹, in the temperature range of 275–350 °C. The catalysts were activated in hydrogen (100 cm³·min⁻¹) at 350 °C for 1 h (ramp rate = 4 °C·min⁻¹). The results showed that with a 2.5 wt.% of Na loading, the CO₂ selectivity was higher than 90%; the product distribution was attributed to different reaction pathways for methanol decomposition. Methanol decarbonylation was favored in the absence of sodium, while formate decarboxylation was promoted in the presence of 2.5 wt.% of Na (Figure 13). These conclusions were supported from the observed weakening of the C-H bond of formate in in situ diffuse reflectance infrared Fourier transform spectroscopy (DRIFT) studies and kinetic isotope effect experiments. The formate exhibited a $\nu(\text{CH})$ stretching band at a low wavenumber, consistent with C-H bond weakening, thus favoring the dehydrogenation that is directly related to the decarboxylation. The hypothesis is that formate is similar to an intermediate; moreover, Na is able to favor the dehydrogenation and the selectivity can be tuned between decarbonylation and decarboxylation based on the Na dopant level.

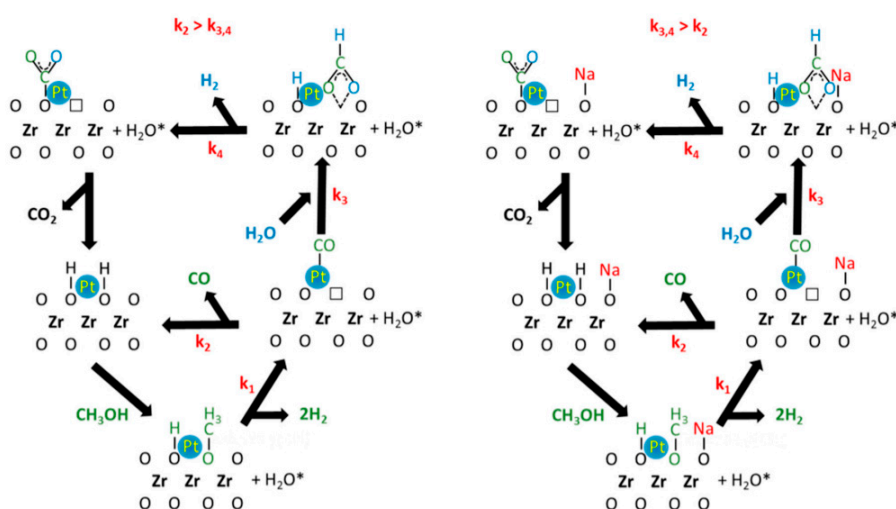


Figure 13. Proposed MSR pathway on undoped Pt/YSZ (right) and Na-doped Pt/YSZ (left) [187].

Zhang et al. investigated the activity of Au-based catalysts supported on modified montmorillonites in MSR [188]. The tests were carried out at atmospheric pressure, in the temperature range of 250–500 °C, with a CH₃OH/H₂O molar ratio of 1. Among the catalysts examined, Au-Ti-Ce/Na-bentonite showed the best performance, with a methanol conversion of 72% and a hydrogen selectivity of 99% at 350 °C. This result was attributed to the formation of the Au-Ce-Ti solid solution into the interlayer space of the bentonite, leading to a high surface area, small Au particle size, and a large average pore volume and diameter. The time-on-stream test showed no significant deactivation during 120 h of reaction (Figure 14).

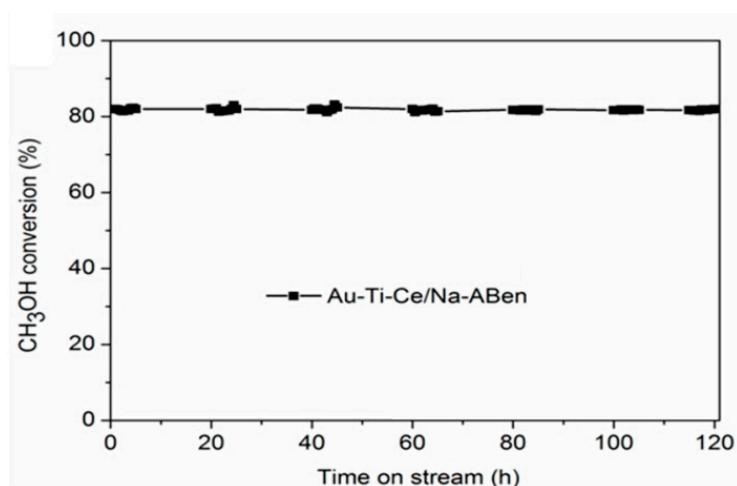


Figure 14. Time-on-stream test. T = 400 °C, CH₃OH/H₂O = 1, 0.175 mL·h⁻¹ [188].

Lytkina et al. studied the influence of the composition and structure of metal-oxide-stabilized zirconia support ($M_xZr_{1-x}O_{2-\delta}$, M = Y, La, Ce) prepared by co-precipitation method in bimetallic Cu-Ni and Ru-Rh catalysts for MSR [189]. The activity tests were carried out at atmospheric pressure in the temperature range of 200–400 °C, with a mixture of methanol and water with a molar ratio of 1/1, at a GHSV of 172 h⁻¹. In this study, a bifunctional mechanism for MSR over the ZrO₂-based catalysts was proposed, in which methanol conversion proceeds on the metal atoms, while the support provides the active sites for the water activation. In cerium-doped catalysts, the fraction of trivalent cerium cations decreases with the increase of cerium amount; thus, the lower catalytic activity for the catalysts with higher cerium loading can be ascribed to the interaction of defects, clustering, or sintering. The lanthanum-doped catalysts showed higher activity than the yttrium ones; however, the selectivity was lower. The Ru-Rh-based catalysts displayed higher activity in both the MSR and the methanol decomposition reaction, which caused a drop in the selectivity. The best performance was obtained with the Ni_{0.2}-Cu_{0.8}/Ce_{0.1}Zr_{0.9}O_{2-δ} catalyst in terms of the hydrogen yield, selectivity, and stability. Lu et al. studied CuZnAlO_x catalysts prepared by co-precipitation method and boron-modified/CuZnAlO_x catalysts with various boron loadings (0.28%, 0.38%, 0.73%, 0.89%, or 4.10%) prepared by impregnation method in MSR [190]. The catalytic tests were performed at atmospheric pressure, at a GHSV of 9000 mL·g⁻¹·h⁻¹, in the temperature range 160–310 °C, with a H₂O/CH₃OH molar ratio of 3. The characterization results showed that the introduction of boron affected the Cu dispersion and reducibility. The best performance was obtained with a boron loading of 0.38%; the methanol conversion reached 93% due to the presence of higher specific surface area, lower reduction temperature, and strong interactions between the boron and copper species, which suppressed the Cu particle migration. Time-on-stream tests showed no deactivation of this catalyst over a period of 102 h of reaction, except for a negligible change for the 0.38B/CuZnAlO_x. Maiti et al. compared the catalytic activity behaviour of sol-gel-synthesized nanostructured Cu_xFe_{1-x}Al₂O₄ (0.3 ≤ x ≤ 0.8; where n = 30, 40, 50, 60, 70, and 80) hercynites with the corresponding catalysts prepared by solution combustion synthesis in MSR [191]. The activity tests were performed at atmospheric pressure, in the temperature

range 200–300 °C, at a GHSV of 30,000 h⁻¹, with a gas stream molar ratio for methanol/water/nitrogen of 1:1.1:8.4. The catalysts prepared by sol–gel method were more active than those prepared by solution combustion synthesis; moreover, Cu doping enhanced the catalytic activity towards methane steam reforming. The Cu_{0.8}Fe_{0.2}Al₂O₄ catalyst showed a methanol conversion of ~80% and low CO selectivity of 2%, even after 50 h of time-on-stream testing; this behaviour was explained as the result of a partial breakdown of the spinel lattice during the reforming reaction, with the formation of CuO followed by reduction to metallic copper, leading to a stable ratio between reduced and oxidized copper (Cu⁰, Cu⁺)/Cu²⁺. XPS studies showed the presence of adventitious carbon; however, the difference in the C1s signal from the fresh to the aged samples indicated a moderate carbon accumulation, also demonstrating that the carbon accumulation was not severe. Song et al. studied the effects of ZnO content on the performance of Zn_yCe₁Zr₉O_x (y = 0, 0.5, 1, 5) in MSR [192]. The catalysts were prepared by using conductive carbon black T100 as a hard template; the catalytic tests were conducted at atmospheric pressure, in the temperature range of 200–500 °C, at a steam-to-carbon of 1.4, at a GHSV of 5151 h⁻¹. The best performance was obtained with the Zn₁Ce₁Zr₉O_x catalyst, which showed full methanol conversion and an improved hydrogen production rate of 0.31 mol·h⁻¹g_{cat}⁻¹ at 400 °C. Moreover, the stability tests, which were carried out for 24 h, showed no deactivation and a CO selectivity below 8%. The characterization results revealed the formation of a solid solution with the incorporation of Zn²⁺ into the Ce₁Zr₉O_x lattice, which modulated the O_{Latt}/O_{Ads} surface ratio and generated a new Zn–O–Zr interfacial structure, increasing the CO₂ selectivity. The CO₂/CO intensity ratio in the desorption peaks observed during CH₃OH-TPD increased with the zinc molar ratio in the catalysts until y = 1 (Zn₁Ce₁Zr₉O_x catalyst) and decreased from y = 1 to y = 5 (Zn₅Ce₁Zr₉O_x catalyst); thus, the highest abundance of lattice oxygen in the Zn₁Ce₁Zr₉O_x catalyst suppressed the undesired CO formation.

3.4. Unconventional Reactor Configuration, Simulation, and Theoretical Studies

This section deals with recently published articles on the MSR, in which the reactor configuration, in addition to being innovative compared to the conventional one (such as membrane or structured reactors), assumes a dominant role in the catalytic activity. In addition, simulations and theoretical studies have also been included.

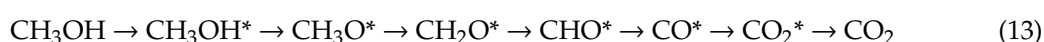
Mateos-Pedrero et al. studied the effect of the surface area and polarity ratio of the ZnO support on the catalytic activity of CuO/ZnO in MSR [193]. The surface area of ZnO was tuned by changing of the calcination temperature, while the polarity ratio was modified by using different salt precursors. The supports were prepared by a modified hydrothermal method, using two different salt precursors, zinc acetate or zinc nitrate, and calcined at four different temperatures: 300, 350, 375, and 400 °C. The catalysts were prepared by impregnation of the support with copper nitrate at pH = 6 using ammonium hydroxide, with a metal loading of 15 wt.% and calcined at 360 °C. The results showed that the copper dispersion and surface area increased with the surface area of the support and that the reducibility of the copper species increased with the polarity ratio in the ZnO support. The activity tests showed a dependence from the surface area of the support, and therefore from the Cu dispersion; moreover, the selectivity increased with the polarity ratio. The best performance was obtained with the catalyst whose support was obtained from zinc acetate and was calcined at 375 °C. This catalyst was tested in a Pd-membrane reactor in two different experiments to evaluate the methanol conversion and gas selectivity stability in one case, and to investigate the hydrogen recovery and hydrogen permeate purity under various operating conditions in the other case. The first set of experiments showed that it is possible to reach 97% of methanol conversion at 300 °C, 2.0 bar, and WHSV = 2.73 h⁻¹, with good stability and selectivity. The second set of experiments showed that it is possible to achieve a hydrogen recovery rate of ca. 75% and a hydrogen permeate purity rate higher than 90% at 330 °C, 2.5 bar, and WHSV = 1.37 h⁻¹. Kim et al. carried out process simulation and design, as well as economic analysis, to evaluate the technical and economic feasibility of MSR in a membrane reactor for ultrapure hydrogen production [194].

The simulation was performed with Aspen HYSYS[®]; certain operating conditions were investigated, such as the effects of the hydrogen permeance ($1 \times 10^{-5} - 6 \times 10^{-5} \text{ mol}\cdot\text{m}^{-2}\cdot\text{s}^{-1}\cdot\text{Pa}^{-1}$), H₂O sweep gas flow rate ($1\text{--}20 \text{ kmol}\cdot\text{h}^{-1}$), and reaction temperature (448–493 K) in a conventional packed-bed reactor, using previously reported reaction kinetics. Improved performances regarding the methanol conversions and hydrogen yield were observed for all the studied cases in the membrane reactor configuration compared to the packed-bed configuration. Higher hydrogen permeance and H₂O sweep gas flow rates were beneficial for methanol conversion, but no further improvement was obtained for H₂O sweep gas flow rates over $10 \text{ kmol}\cdot\text{h}^{-1}$. A unit hydrogen production cost was also calculated, showing a higher cost for the packed-bed reactor ($9.37 \text{ \$ kg}\cdot\text{H}_2^{-1}$) than for the membrane reactor ($7.24 \text{ \$ kg}\cdot\text{H}_2^{-1}$). Köpfle et al. studied the activation and the catalytic performance in MSR of two Zr-containing intermetallic systems, Cu-Zr and Pd-Zr [195]. Metal mixtures of Cu and Zr were prepared with different stoichiometry ratios (Cu/Zr = 9:2, 2:1, 1:2). Moreover, two Pd-Zr systems were prepared by ALD/CVD (atomic layer deposition/chemical vapour deposition) of zirconium(IV)tert-butoxide on Pd and Zr foils (Pd/Zr ratio 2/1). The preparation of the corresponding Cu-Zr intermetallic catalyst was carried out using the Cu foil. The transitions of the initial metal and intermetallic compound structures in the active and CO₂-selective states were monitored in MSR by an inverse surface science and bulk model approach. The CO₂ selectivity and the catalytic performance of the Cu-Zr system were promising due to the formation of a beneficial Cu-ZrO₂ interface. The two Pd-Zr systems showed a low-temperature coking tendency, high water activation temperature, and low CO₂ selectivity. Zhou et al. reported a benchmark study in which the performance of porous Cu-Al fiber sintered felt, constructed using the solid-phase sintering method, was compared to that of Cu fiber sintered felt and Al fiber sintered felt. The fibers were impregnated with Cu/Zn/Al/Zr catalysts and used in a cylindrical MSR microreactor [196]. The results showed that the Cu-Al fiber based catalyst gave higher methanol conversion and hydrogen flow rates than the Cu- and Al-fiber-based catalysts. The rough-fiber-based catalyst showed a much higher methanol conversion and hydrogen flow rate than the smooth one. Moreover, the methanol conversion and hydrogen flow rate increased with the decrease of the Cu fiber weight and the increase of the Al fiber weight. The best performance in terms of hydrogen production was obtained with a three-layer Cu-Al fiber with 80% porosity and a 1.12 g Cu fiber/1.02 g Al fiber. The time-on-stream tests showed a significant deactivation of the catalysts after 32 h due to the coke formation. In further studies, a laser micromilling technique was reported for the fabrication of surface microchannels on porous copper-fiber-sintered felts [197]. The effects of the surface microchannel shape and catalyst loading on the activity in the MSR microreactor was investigated. The results showed that the rectangular shape provided a lower pressure drop, higher average velocity, and higher permeability compared to the stepped and polyline microchannels, as well as the highest methanol conversion and hydrogen flow rate. Furthermore, in the latter case, the deactivation of the catalyst observed during time-on-stream tests was attributed to the carbon deposition and catalyst loss. Tajrishi et al. studied the use of Cu/SBA-15-based nanocatalysts in a parallel-type microchannel reactor for MSR reaction [198]. SBA-15 was prepared by hydrothermal method, while the catalysts were prepared by wetness impregnation method. The catalytic activity tests were carried out at atmospheric pressure; the microchannel reactor walls were coated with the nanocatalysts and a mixture of methanol and distilled water was injected into the microreactor by a syringe pump at various flow rates ($1.8, 2.4$ and $3 \text{ mL}\cdot\text{h}^{-1}$) through a vaporizer at 150 °C . A series of reaction conditions was evaluated on the 5%Cu/SBA-15 catalyst, such as the effects of the reaction temperature ($260, 280, 300, 320,$ and 340 °C), the WHSV ($32.76, 43.68,$ and 54.56 h^{-1}), and the steam-to-carbon molar ratio ($1, 2,$ and 3) on the methanol conversion; hydrogen yield; and H₂, CO, and CO₂ selectivity. Moreover, the effects of promoters were investigated by performing a series of experiments at 300 °C at a weight GHSV of 43.68 h^{-1} and at a steam-to-carbon molar ratio of 2 on the following catalysts: xCu/SBA-15 ($x = 5, 10$ and 15%), 10%Cu/yZnO/SBA-15 ($y = 5, 10$ and 15%), 10%Cu/5%ZnO/2%CeO₂/SBA-15, 10%Cu/5%ZnO/2%ZrO₂/SBA-15, and 10%Cu/5%ZnO/2%CeO₂/2%ZrO₂/SBA-15. Specific surface area measurements and field emission SEM images demonstrated that the addition of CeO₂ and ZrO₂ to the

10%Cu/5%ZnO/SBA-15 catalyst led to a reduction in the agglomeration of crystallites, thus increasing the specific surface area and lowering the pore diameter. The methanol conversion and hydrogen selectivity were improved by ZrO₂ promotion, while ZnO and CeO₂ promoters reduced the CO selectivity. Moreover, CeO₂ and ZrO₂ promoted the stability of the Cu/ZnO/SBA-15-based catalysts, due to the better reducibility of CuO particles and less coke deposition. The 10%Cu/5%ZnO/2%CeO₂/2%ZrO₂/SBA-15 catalyst showed the best performance, displaying optimal methanol conversion of 95.2%, low CO selectivity of 1.4%, high H₂ yield of 90%, and good stability in the time-on-stream test over 60 h of reaction at 300 °C, at a weight space hourly velocity of 43.68 h⁻¹, and at a steam-to-carbon molar ratio of 2, due to smaller size of the copper and zinc crystallites, higher copper dispersion, and greater specific surface area. Liu et al. studied copper foams with different types of hole arrays as catalyst supports for cylindrical laminated MSR microreactors [199]. The copper foams were fabricated by laser processing method; the catalytic formulation (Cu/Zn/Al/Zr) was loaded by impregnation, while macroscopic numerical analysis was used to analyse the reactant distribution on the foams. The optimal hole array distribution was obtained on the basis of the experimental results by varying the reactant flow rate, reaction temperature, and catalyst loading. The simulation results showed that the radial distribution uniformity was improved and the axial flow velocity was increased from the copper foams with hole arrays. The copper foams whose hole size decreased in the arrays from the center to the radial direction provided the best catalytic performance; by feeding a flow rate of 10 mL·h⁻¹ at 300 °C, the initial methanol conversion was 95% and the initial hydrogen production flow rate was 0.52 mol·h⁻¹; after time-on-stream tests for 24 h, the methanol conversion decreased to 70% and the hydrogen production flow rate decreased to 0.35 mol·h⁻¹. Sarafranz et al. investigated the use of the Cu-SiO₂ porous catalyst coated on the internal wall of a microreactor with parallel micropassages in MSR [200]. The catalyst was prepared by coating with copper and silica nanoparticles, using convective flow boiling heat transfer followed by calcination. The catalytic activity tests were carried out in the temperature range of 250–400 °C, with a reactant flow rate of 0.1–0.9 dm³·min⁻¹, a catalyst loading of 0.25–1.25 g, and at a heat flux of 500 kW·m⁻². The highest methanol conversion was obtained at GHSV of 24,000 mL·g⁻¹·h⁻¹, at a temperature of 500 °C, and with a methanol-to-water molar ratio of 0.1. The increase in the GHSV of the reactants generated a decrease in the methanol conversion, which was attributed to the suppression of the reactant diffusion into the pores of the catalyst and to the decrease in the average film temperature of the reactor. Moreover, for the low methanol-to-water molar ratio the reaction was complete, requiring more thermal energy; therefore, greater heat flux was necessary to compensate for the temperature drop. Shanmugam et al. investigated the effect of supports (CeO₂, Al₂O₃, and ZrO₂) and an In₂O₃ co-support in Pt-based catalysts for MSR in a microchannel reactor [201]. CeO₂, Al₂O₃, and ZrO₂ were prepared by sol-gel method, the co-support was obtained by impregnation with In₂O₃, while the catalysts were obtained by impregnation. Two microchannel platelets were coated with the catalysts and sealed face-to-face by laser welding with the inlet and outlet capillaries. The activity tests were carried out in a microchannel reactor at atmospheric pressure in the temperature range of 300–375 °C, with a flow rate for the water/methanol mixture of 30 mL/h and a steam-to-carbon ratio of 1.4. Among the studied catalysts, the best performance was obtained with 15Pt/CeO₂, which exhibited complete methanol conversion, high hydrogen selectivity, and high CO formation (7 vol.%) at 350 °C. The addition of In₂O₃ reduced the CO formation to 1.9 vol.% due to the enhanced dispersion of metallic Pt nanoparticles and to the boost given to the water activation, which reacted with methanol on the Pt surface, leading to the selective formation of CO₂ and H₂ and suppressing the CO formation. The time-on-stream tests showed only slight deactivation in 100 h under reaction conditions at WHSV of 88 L·h⁻¹·g⁻¹. Zhuang et al. developed a multichannel microreactor with a bifurcation inlet manifold and rectangular outlet manifold for MSR, in which the commercial CuO/ZnO/Al₂O₃ catalyst was directly packed [202]. The catalytic tests were performed with a variable steam-to-carbon ratio (1.1–1.5), a variable WHSV (0.4–6.7 h⁻¹) in the temperature range of 225–325 °C, with two catalyst particle sizes of 50–150 mesh and 150–200 mesh. A computation fluid dynamics (CFD) simulation was also performed to study the flow distribution in the multichannel reactor. The results

showed that the methanol conversion was enhanced by increasing the steam-to-carbon ratio and the temperature, as well as by decreasing the WHSV and catalyst particle size. On the other hand, the CO concentration decreased with a growth in the steam-to-carbon ratio and the WHSV, as well as decreased with the decrease of the temperature and catalyst particle size. A time-on-stream test was also carried out for 36 h, achieving a methanol conversion of 94.04% and a CO concentration of 1.05%, with a steam-to-carbon ratio of 1.3, a temperature of 275 °C, a WHSV of 0.67 h⁻¹, and a catalyst particle size of 150–200 mesh. Zhu et al. reported a modelling and design study for a multitubular packed-bed reactor for MSR on a Cu/ZnO/Al₂O₃ catalyst [203]. A multitubular packed-bed reformer pseudo-homogenous model was developed based on Langmuir–Hinshelwood kinetics of the MSR process to investigate the impacts of operating conditions and geometric parameters on the performance. Moreover, pressure drop, heat, and mass transfer phenomena, as well as diffusion inside the catalyst particles, were also investigated. A comparative study was also performed to evaluate the performance of a current–current reactor with respect a co-current reactor.

The simulation results showed that a co-current heat exchanger provided a lower CO concentration and better heat transfer efficacy; moreover, the lower liquid fuel flow rate and higher thermal air inlet temperature gave higher residual methanol and CO concentrations (Figure 15). At a fixed catalyst loading, the increase in the tube numbers, the growth of the baffle plate number, and the decrease in the tube diameter increased both the methanol conversion and the CO concentration. Ke and Lin performed density functional theory computations and transition state theory analyses on the intrinsic mechanism of Ni-catalysed MSR by considering 54 elementary reaction steps [204]. The microkinetic model was obtained by combining the quantum chemical results with a continuous stirring tank reactor. The microkinetic simulations showed that O*, CO*, OH*, and H* are the only surface species with non-negligible surface coverage. The main reaction pathway is described in Equations (13) and (14).



and the rate determining step is:

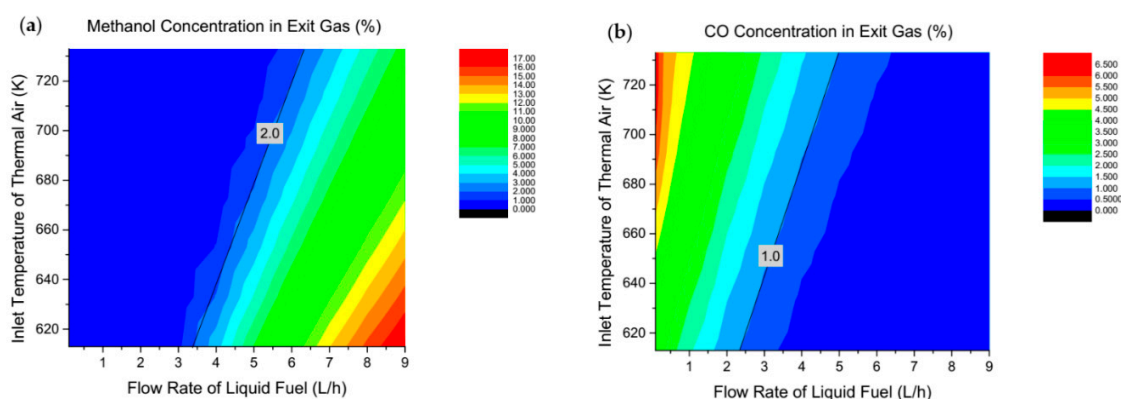


Figure 15. Profiles of the (a) methanol concentration and (b) CO concentration in the exit gas of the reformer with different inlet flow rates for the fuel mixture and inlet temperature of the thermal air [203].

Wang et al. studied a MSR rib microreactor heated by automobile exhaust [205]. The effect of the inlet exhaust and methanol-to-steam ratio on the performance of the reactor were numerically analyzed with a computational fluid dynamic study. The results showed that the methanol conversion increased with the inlet exhaust velocity and the inlet exhaust temperature; moreover, the axial temperature increased along the axis and decreased with the reactant inlet velocity. By fixing the inlet reactant velocity to 0.1 m/s and the inlet temperature to 220 °C, the best performance was obtained with a water/methanol ratio of 1.3, an exhaust inlet velocity of 1.1 m·s⁻¹, and an exhaust inlet temperature of

500 °C, obtaining methanol conversion of 99.4%, hydrogen content of 69.9%, and thermal efficiency of 28%.

3.5. Oxidative Steam Reforming of Methanol

The OSRM is a combination of an exothermic reaction between O₂ and methanol and the endothermic reaction of steam reforming. The exothermic reaction has frequently been assumed to be the partial oxidation (PO) of methanol [206]; however, more recently it was found that with the commercial Cu/ZnO/Al₂O₃ catalyst, the combustion of methanol is the main reaction between oxygen and methanol [207]. This process presents some advantages, such as the possibility to produce hydrogen with a very low concentration of CO; moreover, it is suitable for power variation by varying the methanol/oxygen ratio [208]. A selection of articles on this topic follows below.

Pojanavaraphan et al. investigated the catalytic performance of a series of Au/CeO₂-Fe₂O₃ catalysts prepared by deposition-precipitation for the OSRM [209]. The catalysts were prepared with the aim of investigating the Ce/(Ce+Fe) atomic ratio (1, 0.75, 0.5, 0.25, 0), the gold loading (1, 3, and 5 wt.%), and the calcination temperature (200, 300, and 400 °C). The catalytic activity tests were carried out at a GHSV of 30,000 mL g-cat⁻¹ h⁻¹, in the temperature range of 200–400 °C, at atmospheric pressure. A mixture of distilled water and methanol was continuously injected by a syringe into a vaporizer chamber at 150 °C, at a rate of 1.5 mL h⁻¹. The H₂O/CH₃OH and O₂/CH₃OH molar ratios were varied from 1:1 to 4:1 and from 0 to 2.5, respectively. The best performance was obtained with a gold loading of 3 wt.% and Ce/(Ce+Fe) = 0.25 calcined at 300 °C; this catalyst showed an optimal Au particle size; coexistence of the CeO₂-Fe₂O₃ solid solution and free Fe₂O₃ phase; and strong interaction sites, such as Au-Au, Au⁰-free Fe³⁺, and Ce⁴⁺-Fe³⁺; which were indicated as the main factors for successfully improving the catalytic activity. The presence of high steam content negatively affected the formation of hydroxyl, carbonate, and formate species; the best reaction condition was O₂/H₂O/CH₃OH = 0.6:2:1. Stability tests were carried out, highlighting the effect of a pretreatment with O₂ on the catalytic activity of the catalyst. The results showed that the activity of the untreated catalyst decreased in the methanol conversion from 95.7% to 91% and in the hydrogen yield from 85.87% to 82%, while that of the pretreated catalyst followed the same trend, but with higher conversion and hydrogen yield. The TPO profile of the untreated spent catalyst showed two peaks attributed to the different types of coke formed, with a total coke percentage of 0.629 wt.%. The pretreated catalyst showed the first oxidation peak at 84 °C with low intensity due to carbonaceous species, before being converted to the coke, revealing that the O₂ pretreatment is able to reduce or retard the coke formation rate during the stability test via coke gasification; the coke percentage was only 0.053 wt.%. These data demonstrated that the coke formation did not affect the stability of the pretreated catalyst, suggesting that the O₂ pretreatment could reduce or retard the coke formation rate. Pérez-Hernández et al. investigated the effect of the bimetallic Ni/Cu loading on ZrO₂ support in the autothermal steam reforming of methanol (ASRM) for hydrogen production [210]. The support was prepared by sol-gel method while the catalysts were prepared by sequential impregnation to obtain three different total metallic loading values of 3 wt.%, 15 wt.%, and 30 wt.%, with a Cu/Ni ratio equal to 4:1. TEM-EDX images highlighted the core-shell structure of the Cu/Ni nanoparticles, but in the case of the 30wt.%Ni/Cu/ZrO₂ sample the shell was constituted by the Ni-Cu alloy. The activity tests showed that the methanol conversion increased with the Ni/Cu loading, thus the highest conversion was obtained with the 30wt.%Ni/Cu/ZrO₂ catalyst; however, the 15wt.%Ni/Cu/ZrO₂ catalyst exhibited the highest hydrogen selectivity. A time-on-stream test was also performed on the 30wt.%Ni/Cu/ZrO₂ catalyst, which exhibited stable performance during a 46 h time-on-stream test at 400 °C, without apparent deactivation. Mierczynski et al. studied the performance of copper- and gold-doped copper catalysts supported on a multiwalled carbon nanotube (MWCNT) prepared by wet impregnation and deposition-precipitation methods in OSRM [211]. The tests were carried out at 200 and 300 °C on 100 mg of catalyst and with a stream composition of H₂O/CH₃OH/O₂ (molar ratio = 1:1:0.4), a GHSV of 26700 h⁻¹, under atmospheric pressure, with a

total flowrate of $31.5 \text{ mL}\cdot\text{min}^{-1}$ and methanol concentration of 6% (Argon was used as the diluent gas). The in situ XRD analysis showed the occurrence of Au-Cu alloy in the bimetallic catalyst during the reduction process at $300 \text{ }^\circ\text{C}$. The highest activity and hydrogen yield were obtained with the 0.5%Au–20%Cu/MWCNT bimetallic catalyst; the performance was related to the reducibility and to the highest total acidity of the catalytic system, which is able to stabilize the intermediate formed during the reaction. Jampa et al. investigated the use of Cu-loaded mesoporous ceria and Cu-loaded mesoporous ceria-zirconia catalysts synthesized by nanocasting process, using MCM-48 as the template (% of Cu loading varied from 1 to 12 wt.% in OSRM [212]). The catalytic activity tests were performed over a temperature range of $200\text{--}400 \text{ }^\circ\text{C}$ at atmospheric pressure, with a mixture of $\text{H}_2\text{O}/\text{CH}_3\text{OH}$ ($1.5 \text{ mL}\cdot\text{h}^{-1}$, molar ratio varied from 1:1 to 3:1), He ($45 \text{ mL}\cdot\text{min}^{-1}$), and oxygen ($45 \text{ mL}\cdot\text{min}^{-1}$). The results showed that the best catalytic performance was obtained with 9 wt.% Cu loading, which assured methanol conversion of 100% and hydrogen yield of 60%; however, these results were obtained at $350 \text{ }^\circ\text{C}$ when mesoporous CeO_2 was used as the support and at $300 \text{ }^\circ\text{C}$ when $\text{CeO}_2\text{-ZrO}_2$ was used as the support by feeding O_2 at $5 \text{ mL}\cdot\text{min}^{-1}$ and a $\text{H}_2\text{O}/\text{CH}_3\text{OH}$ molar ratio of 2:1. The time-on-stream stability tests over 169 h of reaction resulted in a continuous decrease of the methanol conversion and hydrogen yields for both the 9%Cu/ CeO_2 and 9%Cu/ CeZrO_4 . The TPO profiles of the spent catalyst 9%Cu/ CeO_2 showed two peaks at $207 \text{ }^\circ\text{C}$ and $296 \text{ }^\circ\text{C}$, whereas 9%Cu/ CeZrO_4 showed the oxidation peaks at 266 and $484 \text{ }^\circ\text{C}$, indicating the presence of two different types of coke or carbonaceous species. The oxidation peaks at 207, 266, and $296 \text{ }^\circ\text{C}$ were assigned to the poorly polymerized coke deposited on the catalyst particles, while the peak at $484 \text{ }^\circ\text{C}$ was ascribed to highly polymerized coke deposited near the catalyst-support interface. Moreover, the significant decrease in the Brunauer-Emmett-Teller (BET) specific surface area of the spent catalysts suggested that sintering had occurred. Based on these data, the deactivation was attributed to coke formation and agglomeration; however, the ceria/zirconia-based catalyst showed reduced CO selectivity. Thus, the main conclusion was that the addition of zirconium into the support improved the redox property, the thermal stability, and the oxygen storage capacity of the catalyst, resulting in a better performance in terms of CO oxidation reaction, and thus in a low CO level during autothermal steam reforming of methanol. Pu et al. investigated the Cu/ZnO-based catalysts promoted by Sc_2O_3 in ASRM [213]. The Cu/ $\text{Sc}_2\text{O}_3\text{-ZnO}$ catalysts were prepared by the reverse precipitation method, with Cu metal loading of 15 wt.% and Sc/Zn molar ratios of 0, 0.03, 0.05, and 0.07. The catalytic activities were evaluated in the temperature range of $220\text{--}600 \text{ }^\circ\text{C}$ at atmospheric pressure, while an aqueous solution of methanol at a rate of $0.05 \text{ mL}/\text{min}$ was fed together with a mixed gas flow ($50 \text{ mL}\cdot\text{min}^{-1}$) of N_2 and O_2 . The characterization results showed that the Sc promotion assured a reduction of the particle size and an increase of the metal dispersion of Cu. In addition, the Sc doping enhanced the interaction between the metal and support in the ZnO lattice, improving the metal dispersion and sintering resistance of the catalysts. The best performances in terms of catalytic activity and stability were obtained with the catalyst characterized by the Sc/ZnO molar ratio of $0.05 \text{ mol}\cdot\text{mol}^{-1}$. The decrease of the methanol conversion in the time-on-stream tests was attributed to sintering phenomena: in fact, coke formation was suggested by the performed analysis.

To summarize, the results shown in Table 2 highlight significant differences in the performance of the catalysts studied in the reviewed articles on the methanol reforming in terms of the carbon formation rate. The highest reported rate ($10^{-2} \text{ g}_{\text{coke}}\cdot\text{g}_{\text{catalyst}}^{-1}\cdot\text{g}_{\text{carbon, fed}}^{-1}\cdot\text{h}^{-1}$) was for Cu/ Al_2O_3 [165], while the lowest one ($6.3\cdot 10^{-7} \text{ g}_{\text{coke}}\cdot\text{g}_{\text{catalyst}}^{-1}\cdot\text{g}_{\text{carbon, fed}}^{-1}\cdot\text{h}^{-1}$) was for 10%Cu-10%Zn-2%Zr/MCM-41 [183]. Although in the two cases the reaction conditions were very different, both in terms of temperature and steam-to-carbon ratio ($500 \text{ }^\circ\text{C}$ and $\text{S}/\text{C} = 1.5$ in the first case; $300 \text{ }^\circ\text{C}$ and $\text{S}/\text{C} = 2$ in the second case), the effect of the zirconium promoter seemed to play a major role. Zirconium, in fact, can stabilize the active species and decrease the growth of metal oxides during the synthesis process, thus allowing the size of the crystallites to be reduced and allowing a better dispersion of the active phases. On the other hand, the use of noble metals such as gold, as well as the addition of oxygen in the reforming reaction, does not seem to suppress the formation of coke; however, further studies are necessary.

Table 2. Carbon formation rates for various catalysts employed for steam reforming and oxidative steam reforming of methanol.

Catalyst ^a	Operative Conditions ^b	T (°C)	WHSV ^c (h ⁻¹)	X MeOH (%)	Carbon Formation Rate ^d (MULTIPLIED for 1000)	Ref.
Methanol Steam Reforming						
15%Cu-MCM-41	H ₂ O/CH ₃ OH = 3/1	250	1.0	≈73 after 48 h	0.015	[158]
20%Cu-MCM-41	H ₂ O/CH ₃ OH = 3/1	250	1.0	≈60 after 48 h	0.024	[158]
Cu-ZnO-Al ₂ O ₃ -ZrO ₂ -Ga ₂ O ₃ Cu/Zn/Al/Zr/Ga = 14.9:30.9:3.9:10.8:1.9 mass ratio	H ₂ O/CH ₃ OH = 1/1	275	4.3	≈85 after 70 h	0.010	[159]
Cu-ZnO-Al ₂ O ₃ -ZrO ₂ -Ga ₂ O ₃ Cu/Zn/Al/Zr/Ga = 13.3:28.2:3.9:10.0:1.8 mass ratio	H ₂ O/CH ₃ OH = 1/1	275	4.3	≈70 after 70 h	0.014	[159]
Pd-MCM-41	H ₂ O/CH ₃ OH = 3/1	300	1.0	≈32 after 40 h	0.041	[163]
Zn-MCM-41	H ₂ O/CH ₃ OH = 3/1	300	1.0	≈5 after 40 h	0.15	[163]
Ni-MCM-41	H ₂ O/CH ₃ OH = 3/1	300	1.0	≈15 after 40 h	0.16	[163]
Cu-MCM-41	H ₂ O/CH ₃ OH = 3/1	300	3.0	≈75 after 40 h	0.049	[163]
Cu/Al ₂ O ₃	H ₂ O/CH ₃ OH = 3/2	500	0.8	≈91 after 5 h	10	[165]
NixMgyO Impregnation	H ₂ O/CH ₃ OH = 1/1	600	65.7	51.4 after 20 h	0.0079	[168]
NixMgyO Hydrothermal method	H ₂ O/CH ₃ OH = 1/1	600	65.7	58.3 after 20 h	0.0030	[168]
NixMgyO Co-precipitation	H ₂ O/CH ₃ OH = 1/1	600	65.7	57.3 after 20 h	0.085	[168]
Cu/cubic-ZnTiO ₃	N ₂ /H ₂ O/CH ₃ OH = 1/2/1	250	1	≈63 after 42 h	1.1	[177]
Cu/hexagonal-ZnTiO ₃	N ₂ /H ₂ O/CH ₃ OH = 1/2/1	250	1	≈5 after 42 h	6.7	[177]
10%Cu-10%Zn/MCM-41	H ₂ O/CH ₃ OH = 2/1	300	1.62	≈75 after 60 h	0.0011	[183]
10%Cu-10%Zn-2%Zr/MCM-41 Impregnated	H ₂ O/CH ₃ OH = 2/1	300	1.62	≈83 after 60 h	0.00095	[183]
10%Cu-10%Zn-2%Zr/MCM-41 Sol-gel method	H ₂ O/CH ₃ OH = 2/1	300	1.62	90.2 after 60 h	0.00079	[183]
10%Cu-10%Zn-2%Zr/MCM-41 MCM-41 pretreated with acetic acid	H ₂ O/CH ₃ OH = 2/1	300	1.62	92.8 after 60 h	0.00063	[183]
10%Cu/SBA-15	H ₂ O/CH ₃ OH = 2/1	300	43.7	≈64 after 60 h	0.0031	[198]
10%Cu/5%ZnO/SBA-15	H ₂ O/CH ₃ OH = 2/1	300	43.7	≈74 after 60 h	0.0025	[198]
10%Cu/5%ZnO/2%CeO ₂ /SBA-15	H ₂ O/CH ₃ OH = 2/1	300	43.7	≈85 after 60 h	0.0013	[198]
10%Cu/5%ZnO/2%ZrO ₂ /SBA-15	H ₂ O/CH ₃ OH = 2/1	300	43.7	≈84 after 60 h	0.0031	[198]
10%Cu/5%ZnO/2%CeO ₂ /2%ZrO ₂ /SBA-15	H ₂ O/CH ₃ OH = 2/1	300	43.7	≈86 after 60 h	0.0031	[198]
Oxidative Steam Reforming of Methanol						
xAu/CeO ₂ -Fe ₂ O ₃ x = 3 wt.%, Ce/(Ce+Fe) = 0.25.	O ₂ /H ₂ O/CH ₃ OH = 0.6/2/1.	350	11.9	91 after 12 h	0.098	[209]
xAu/CeO ₂ -Fe ₂ O ₃ x = 3 wt.%, Ce/(Ce+Fe) = 0.25.	O ₂ /H ₂ O/CH ₃ OH = 0.6/2/1. O ₂ pretreatment	350	11.9	92 after 12 h	0.0082	[209]
9 wt.%Cu/CeO ₂	H ₂ O/CH ₃ OH = 2/1; O ₂ = 5 mL·min ⁻¹	350	0.9	65 after 2.8 h	0.0042	[212]
9 wt.%Cu/CeZrO ₄	H ₂ O/CH ₃ OH = 2/1; O ₂ = 5 mL·min ⁻¹	300	0.9	65 after 2.8 h	0.0032	[212]

Note: ^a The metal or oxide loadings are intended for the weight of the catalyst; ^b all the tests were performed at atmospheric pressure; ^c refers to the methanol mass flow rate; ^d g_{coke}·g_{catalyst}⁻¹·g_{carbon, fed}⁻¹·h⁻¹.

4. Bioglycerol Reforming

An extensive research study concerning the applications of bioglycerol as the main by-product of biodiesel production processes (~10% by weight) [214] was carried out in recent years. Indeed, with the constant growth of the biofuel market and approximately 36 million tons of biodiesel having been produced [215], the supply of bioglycerol exceeds the global demand (~ $3 \cdot 10^6$ ton produced by 2020, with a demand below $\sim 5 \cdot 10^5$ ton/year) [216]. The consequent drop in bioglycerol prices and the difficulties in the disposal of the produced surplus constitute a threat for the biodiesel production process, which is already fails to be competitive in terms of price [215,217,218].

Crude glycerol (i.e., glycerol derived from the biodiesel production process) is a highly viscous liquid characterized by a dark color, which includes variable quantities of soap, catalyst, alcohol, monoglycerides, diglycerides, polymer, water, unreacted triacylglycerols, and biodiesel; glycerol concentrations are in the range of 40–85%, depending on the efficiency of the biodiesel production process. Due to the presence of such impurities, it is not possible to use crude glycerol in most typical applications (e.g., cosmetics, food, alkyd resins, tobacco, pharmaceutical, polyurethane [217]), which are depicted in Figure 16.

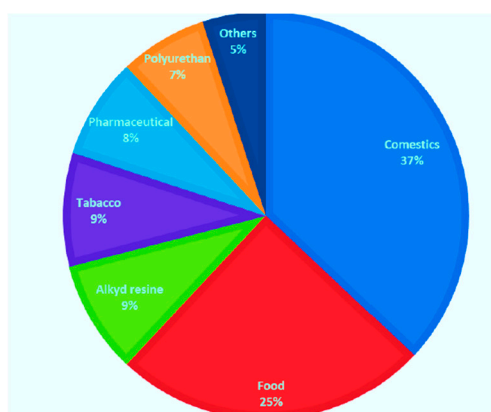


Figure 16. Crude glycerol's most typical applications [217].

Moreover, crude glycerol purification through distillation is an expensive process and most biodiesel plants use this feedstock for direct burning process; however, in this way, the recovery efficiency is low due to the combustion difficulties caused by the high viscosity and the formation of highly toxic substances (e.g., acrolein and aldehyde). Hence, the employment of surplus-produced crude glycerol to obtain other value-added chemicals could represent the best route in view of improving the biodiesel industry's economic feasibility [215,219].

An interesting pathway for crude glycerol revalorization is to use it as a renewable biomass source for H_2 production; thereby, hydrogen, as a promising fuel for moving vehicles and providing power and heat for industries, would be produced, involving less energy consumption in comparison with the traditional routes for its obtainment (water electrolysis and thermochemical processes) [219]. Hydrogen can be produced by glycerol via several processes, including steam reforming, partial oxidation, autothermal reforming, aqueous-phase reforming, dry reforming, and photocatalytic reforming. Among them, steam reforming has drawn major attention. In fact, since the steam reforming of methane is presently the most widely-used process in the industry to obtain hydrogen, the adoption of glycerol would not require many changes in the already existent systems [218,220]. However, glycerol steam reforming (GSR) is an endothermic catalytic process that requires large energy consumption and suffers from catalyst deactivation caused by coke formation. Additionally, the other routes for H_2 generation from glycerol are characterized by several disadvantages. The autothermal reforming (the process in which the partial oxidation is coupled with steam reforming) leads to a lower energy consumption compared to the SR. In fact, the steam reforming step absorbs the energy produced by

the PO reaction; however, as a drawback, the presence of several hotspots caused by the heat produced during the PO can result in negative effects on the catalyst activity. The liquid-phase reaction (APR) operating at pressures of 30–80 bar and temperatures of 200–250 °C, reduces the amount of necessary heat, especially due to the liquid form of the reactant, which does not require energy for vaporization; however, this process usually requires more time compared to the SR and requires noble metals to be adopted as catalysts (generally Pt), increasing costs. Glycerol dry reforming (GDR) appears to be an attractive path for H₂ production, as it is a carbon capture and recycling (CCR) approach; indeed, with the adoption of this process, CO₂ would be converted and recycled back into fuels and added value chemicals. Regardless, the major obstacles in the application of this technology concern the sintering of catalysts particles and the coke accumulation on the catalysts' surfaces, which are even higher compared to other reforming processes. A novel route could be represented by the photocatalytic reforming of glycerol, in which H₂ would be produced under ambient conditions, in the presence of an appropriate catalyst and solar light [62,219,220].

Catalysts activity and stability are essential aspects in the transformation of glycerol into hydrogen through reforming reactions, as they allow the activation energy to be lowered, improving the kinetics of the involved chemical reactions, thus reducing the energy requirements and the correspondent costs [219]. In recent years, an extensive effort has been made towards improving the activity of catalysts. Studies have been performed on both noble and non-noble metals, different kinds of supports, and the influence of promoters. Moreover, intensified investigations on the selective removal of reaction products have also been performed in order to avoid the thermodynamic limitations (glycerol conversion and hydrogen yield) of the process [218]. Since the positive results gained have been in terms of catalyst activity, the main critical issue in glycerol reforming reactions remains the stability of the employed catalysts.

Catalyst stability, the fundamental challenge in the industrial development of glycerol reforming processes, is mainly compromised by metal sintering and coke deposits. Coke formation in glycerol reforming reactions is a truly complex aspect, since a multitude of carbon sources may be responsible for coke deposits, thus making it difficult to define the catalyst deactivation pathway [221]. Numerous side reactions involved in glycerol conversion lead to the formation of coke, such as the Boudouard reaction (Equation (8)), olefin polymerization (Equation (6)), glycerol dehydration, and rearrangement and condensation reactions [222]. Papageridis et al. [223], having gained a deepened understanding of carbon deposition, suggested that atomic carbon or C_yH_{1-y} species (C_α species) are generated by dissociative chemisorption of the hydrocarbon on the catalysts surface. Thus, the production of an amorphous film (C_β) by dehydropolymerization occurred, which can subsequently lead to the formation of graphitic carbon. Otherwise, these carbon atoms may also be dissolved and diffused through the metal to active growth areas, resulting in the precipitation of amorphous vermicular carbon (C_γ) or whiskers (Figure 17). Moreover, under harsh and protracted reaction conditions, the amorphous carbon can also be converted into graphitic form (C_δ) [223]. An accurate analysis of the nature of the formed coke is a powerful tool in the improvement of catalyst stability, as the total amount of generated coke has less impact in catalytic deactivation in comparison to the degree of graphitization of the deposits [224,225]. Temperature-programmed oxidation tests (TPO) performed in numerous research studies have pointed out the easier oxidation of amorphous carbon (T below 550 °C) compared to filamentous and graphitic carbon deposits, such as carbon nanofibers or carbon nanotubes (T over 600 °C) [33,226].

The extent of coke deposition in glycerol reforming reactions is mainly dependent on the nature of the active phase, the extent of dispersion, and the chemical characteristics of the supports or promoters.

Glycerol reforming has been investigated for various metals and the below chart summarizes the papers considered in this review, dividing them on the basis of the active phase analyzed during the study. As it is possible to see from the graph (Figure 18), in recent years, due to their good catalytic activity, low cost, and ease of availability, Ni-based catalysts have drawn major attention among the

other active phases. Regarding the active phase, the most investigated materials have been Ni-, Co-, Rh-, Pt-, and Ru-based catalysts; attention has also been given to Ir, Cu, and Pd catalysts.

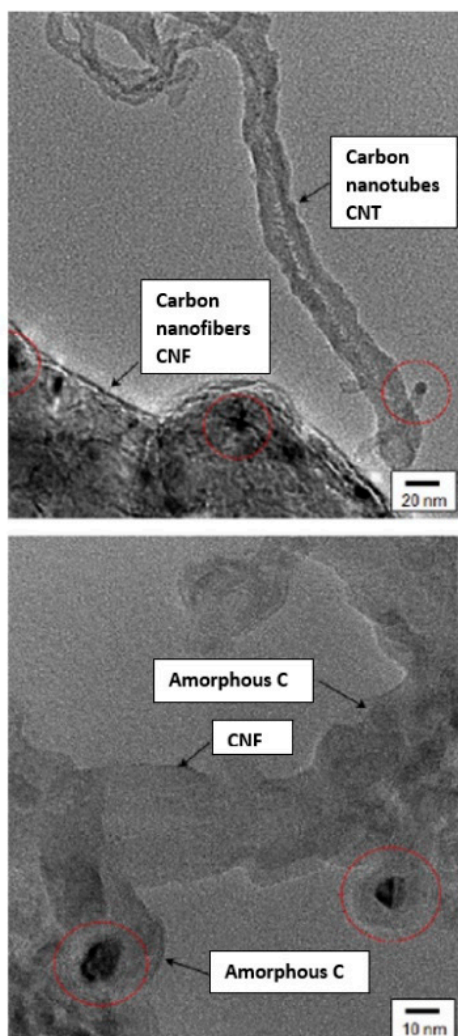


Figure 17. TEM images of amorphous and graphitic carbon formed during glycerol reforming.

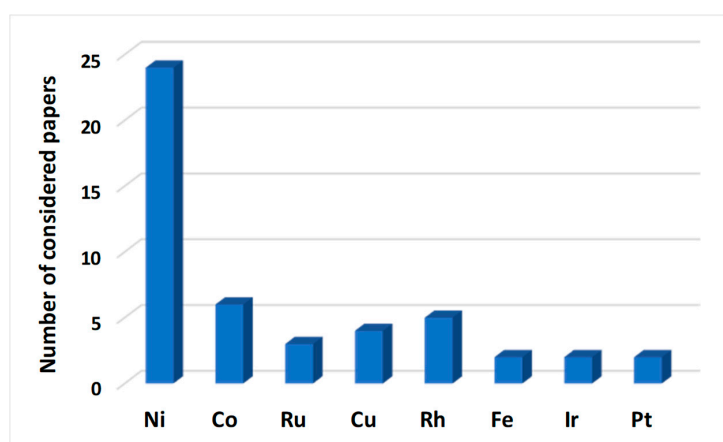


Figure 18. Number of considered papers as a function of the active phases analyzed for glycerol reforming.

4.1. The Influence of the Active Phase

In the following paragraph, selected papers highlighting the roles of active species on catalyst stability for glycerol reforming are discussed.

As anticipated above, nickel is widely used, mainly due to its low cost and satisfactory activity; in addition, Ni has been found to promote the water–gas shift reaction, leading to an increase of H₂ production [215]. Papageridis et al. [223] made a comparison between Ni-, Co-, and Cu/ γ -alumina-supported catalysts for the steam reforming of glycerol, observing the higher ability of the Ni/Al sample to convert glycerol compared to Co/Al and Cu/Al catalysts. On the other hand, the Ni-based catalyst showed worse stability, characterized by a drastic drop in activity within the first 7 h. Rh, Ru, Pt, and Ir have been tested in GSR by Sensei et al. by preparing precious metal nanocatalysts over the promoted Al₂O₃ with MgO. In the stability test performed at 600 °C (GHSV = 35,000 mL g⁻¹ h⁻¹ and H₂O:C₃H₈O₃ = 9), Rh showed a glycerol conversion of ~98% almost constantly over 20 h, while the other metals were characterized by a drastic decrease in the conversion within the first 5 h. Moreover, from the TPO analysis of Rh/MgAl₂O₄, two oxidation peaks were detected, corresponding to the formation of amorphous and graphitic carbon, whereas for Ru, Pt, and Ir, only the presence of graphitic carbon has been evaluated [226]. Rh-alumina catalyst stability was also studied in GSR by Silva et al. [227]. A decrease in the glycerol conversion from 99% to 92% was achieved after 13 h of time-on-stream testing. Moreover, the characterization of the spent catalyst carried out by Raman spectroscopy, SEM/EDS, and TPO showed the presence of amorphous carbon species. According to the results of the TPO analysis, the authors regenerated the catalyst in air at 500 °C, obtaining a complete recovery of the catalytic performance. Montmorillonite (MMT)-supported nickel nanoparticle (Ni/MMT) catalysts were prepared by Jiang et al. In order to optimize the Ni loading and the calcination temperature in GSR. Stability tests were performed on the three catalysts containing 20% Ni (Ni/MMT molar ratio 1:1) and calcination was performed at different temperatures (1Ni-1MMT-800, 1Ni-1MMT-700, and 1Ni-1MMT-600, calcined at 800, 700, and 600 °C, respectively). The 1Ni-1MMT-700 catalyst showed the best stability among all the tested catalysts, probably due to the better dispersion of the metal obtained with the calcination at 700 °C. Furthermore, comparing the stability of 1Ni-1MMT-700 and 1Ni-1Al-700 under 30 h of TOS, a rapid deactivation of the alumina-based catalyst was found. This result, coupled with the characterization of the spent catalysts, pointed out the different reaction pathways for the two catalysts; indeed, with Al₂O₃ acid, dehydration reactions that lead to coke precursors are more prevalent than dehydrogenation reactions [228]. Ni behavior in the steam reforming of glycerol has also been studied over a novel fly-ash-based catalyst. In the stability evaluation, which was performed at 550 °C with a steam/glycerol ratio of 10 and three different space periods of 3 h for time-on-stream testing, glycerol conversions higher than 90% were obtained [229]. Mono- and bimetallic Ni-based catalysts (Ni-Co, Ni-Cu, and Ni-Zn) supported on attapulgite were submitted in a GSR stability investigation at 600 °C, with a steam/glycerol ratio of 9 and GHSV of 9619 h⁻¹. After 30 h of time-on-stream testing, among all the catalysts, Ni-Zn/ATP exhibited the best performance, with glycerol conversion and H₂ selectivity remaining almost stable over the time period [230]. Carrero et al. [231] evaluated the performance of bimetallic Ni-(Cu, Co, Cr)/SBA-15-supported catalysts; the addition of the second metal favored the dispersion of the Ni phase and the metal–support interactions, thus leading to better performances in GSR, particularly for the Ni-Cr/SBA-15 catalyst. This catalyst also showed a lower amount of deposited coke compared with the other bimetallic catalysts and a relatively good stability within 60 h at 600 °C. Bimetallic (Co, Cu, and Fe)-Ni/CNTs catalysts were analyzed in low-temperature GSR (375 °C) tests; a glycerol conversion of ~91% was achieved for Co-Ni/CNTs, which was also characterized by a lower amount of deposited coke (0.05 mg_C·mg_{cat}⁻¹). Moreover, the thermogravimetric analysis performed on Co-Ni/CNTs revealed a shift of the coke peak to lower temperatures, pointing out that the Co addition may have increased the formation of amorphous carbon [232]. The influence of the active phase on the stability of the catalysts and the nature and extent of coke deposits was also analyzed in relation to the dry reforming of glycerol (GDR) by Tavanarad et al. [233], who in 2018 prepared and proved various

Ni/ γ -alumina catalysts by varying the Ni loading from 5 to 20 wt.%. The first activity screening on the Ni content showed that the best performances were obtained with a content of nickel of 15 wt.%, while a Ni loading of 20 wt.% resulted in worse nickel dispersion and bigger crystalline structures. The 15Ni/ γ -Al₂O₃ was subsequently tested at 700 °C under 20 h of time-on-stream; a drastic drop in the catalyst activity was observed in the first 5 h, followed by an almost constant glycerol conversion of ~55% for the next 15 h. TPO and SEM analyses of the catalyst after the stability test evidenced the presence of whisker-type carbonaceous species on its surface. A comparison between the stability of catalysts with different metals as the active phase and the same support specie was investigated by Bac et al. [234] via 72-h time-on-stream stability tests at 750 °C, carried out on Rh, Ni, and Co supported on Al₂O₃-ZrO₂-TiO₂ (AZT) catalysts. Better performances were obtained for Rh/AZT and Ni/AZT. Indeed, for both catalysts the CO₂ conversion was above 91% of the thermodynamic limit, characterized by decreases of only 13% and 8%, respectively. The stability of Rh/AZT was attributed to the lack of sintering and carbon deposits, while Ni/AZT exhibited the ability to post-gasify surface carbon species that were deposited on the catalyst during the first few hours. Moreover, the Co/ATZ catalyst showed a drastic drop in CO₂ conversion, suggesting the presence of severe irreversible carbon formation.

Larimi and co-workers [235] investigated the influence of the Ce/Zr ratio on the performance of a Pt_{0.05}Ce_xZr_{0.95-x}O₂ catalyst for the aqueous-phase reforming of glycerol (GAPR), finding a dependence of the reactivity of the catalyst by the metal ratio, which influenced the Pt oxidation state, the active metal dispersion, the surface area, and the particle size. The catalyst showing the best results in term of activity (Pt_{0.05}Ce_{0.475}Zr_{0.475}O₂) was subsequently tested for 50 h using TOS at 250 °C and 50 bar, during which no deactivation was detected. A comparison between monometallic Ir and bimetallic Ir-Ni and Ir-Co catalysts was evaluated by Espinosa-Moreno et al. [236], who found that IrNi bimetallic catalysts excelled, probably as a result of the high tendency of Ni to cleave to the C-C bond. Moreover, the IrNi/La₂O₃ sample exhibited improved resistance to deactivation, ascribable to the carbon species removal on Ni sites, which is promoted by the oxygen species formed upon La addition. Bimetallic Ni catalysts also showed less CH₄ and CO selectivity, pointing out that the addition of Ni to Ir reduces the methanation reaction and increases the metal-support interactions, thus leading to higher H₂ concentrations.

4.2. The Role of the Support

The role of the support is also fundamental in improving the stability of the adopted catalysts; the present paragraph discusses the benefits and drawbacks of the choices of various supports for bioglycerol reforming.

As a matter of fact, high dispersion and large surfaces are the mainly factors that enhance reactivity in glycerol reforming reactions nonetheless, support acidity and basicity properties also play key roles on the formation of coke deposits. Other authors [237,238] employed Langmuir-Hinshelwood and Eley-Rideal kinetic models coupled with statistical discrimination and thermodynamic evaluation, and identified a molecular adsorption mechanism for glycerol and steam on both Brønsted acidic and basic sites on the catalysts. Thus, they pointed out the necessity of having acidic sites on the surface to improve the process efficiency. On the other hand, acid supports (Al₂O₃) tend to improve dehydration, dehydrogenation, hydrogenolysis, and condensation reactions, which cause coke deposits, leading to rapid deactivation of catalysts [30]. Charisiou and co-authors, in order to evaluate the influence of the support on the glycerol steam reforming (GSR), performed an investigation on nickel catalysts (8 wt.%) supported on Al₂O₃, ZrO₂, and SiO₂. The results of the 20 h stability test at 600 °C pointed out the behavior of different catalysts related to the acidity or basicity of the three supports. In particular, the catalyst prepared on the acidic alumina (Ni/Al₂O₃) showed drastic deactivation, causing the blockage of the active sites by coke precursors formed on the acidic surface sites. Conversely, the more basic Ni/ZrO₂ catalyst appeared to be less affected by deactivation, which may be attributed to the stronger metal-support interactions observed during the TPR analysis, as well as to the capability of

ZrO₂ to enhance the water adsorption and activation. Lastly, the Ni/SiO₂ catalyst ensured the best outcomes in terms of both glycerol conversion and H₂ selectivity, thus leading to the advantages gained from the neutral nature of the support, exploiting both acidic and basic surface sites. Moreover, in the characterization of the spent catalysts, Ni/Al₂O₃ showed the lowest amount of deposited coke (~40%), while for the other two samples the value was almost equal or higher (~50%). On the other hand, the carbon degree of graphitization has also been estimated, which followed the order Ni/Al₂O₃ > Ni/ZrO₂ > Ni/SiO₂, thus leading to the interconnection between the nature of the deposited coke and the deactivation catalysts [224]. The influence of the support towards Ni-based catalysts in the GSR has also studied by Zamzuri and co-authors [239] through the examination of Ni/Al₂O₃, Ni/La₂O₃, Ni/ZrO₂, Ni/SiO₂, and Ni/MgO. The TOS stability test carried out at 650 °C for 5 h showed that the catalysts' overall activity increased following the order Ni/Al₂O₃ > Ni/La₂O₃ > Ni/ZrO₂ > Ni/MgO > Ni/SiO₂. Conversely, while Ni/La₂O₃, Ni/ZrO₂, and Ni/SiO₂ were found to be almost stable within the time-on-stream tests, Ni/Al₂O₃ and Ni/MgO showed decreased activity. Since Al₂O₃ has attracted major attention as a support for catalysts in GSR, by virtue of its high surface area and mechanical and chemical resistance under reaction conditions, numerous strategies have been investigated in order to limit the coke deposition, which is probably caused by the acidic properties of Al₂O₃. A comparison between Ni catalysts supported on mixed lanthana-alumina and Ni catalysts supported on commercial alumina pointed out that addition of La favored the dispersion of the active phase, increasing the basicity of the support and increasing the metal-support interactions. Moreover, after the stability tests, the comparison between the spent catalysts also showed the different nature of the carbon deposits on the catalysts surface. In fact, even though the amount of deposited carbon was approximately equal (0.41 g_{coke}·g_{catalyst}⁻¹ for Ni/Al and 0.44 g_{coke}·g_{catalyst}⁻¹ for Ni/LaAl), TPO and Raman characterizations showed the presence of more graphitic carbon species on the Ni/Al samples than Ni/LaAl, for which almost amorphous carbon deposits were detected. This result was in agreement with the trends of the stability tests, from which it was possible to highlight the good stability in the case of Ni/LaAl and a drastic drop in the activity of Ni/Al [221]. La-modified Al₂O₃ was also investigated by Sanchez et al. as a support for Ni catalysts in GSR reactions. The stability tests were performed on the bare supports and on the catalysts, involving 4 h time-on-stream tests for Ni/Al₂O₃ and Ni/La₂O₃-Al₂O₃ at 700 °C and WHSV = 35 h⁻¹. The addition of La to the support enhanced the H₂ production, giving a result that was close to that obtained with the Ni catalyst; moreover, while Ni/Al₂O₃ showed a drop in the H₂ production over time, Ni/La₂O₃-Al₂O₃ gave an almost stable result after 90 min of reaction. The TGA analysis carried out on the spent catalysts also showed that the amount of coke deposited on Ni/Al₂O₃ was almost twice that deposited on Ni/La₂O₃-Al₂O₃. Moreover, the SEM analysis revealed that the surface of Ni/Al₂O₃ was covered by carbon filaments, which could be the reason for the catalyst deactivation [30]. Additionally, modifications of the alumina support were investigated by Bobadilla et al., who prepared NiSn bimetallic catalysts supported on Al₂O₃, evaluating the influence of the addition of Mg and Ce on the support. NiSn/Al, NiSn/AlMg, NiSn/AlCe, and NiSn/AlMgCe were submitted to stability tests at 650 °C, P = 1 atm, and with a water/glycerol molar ratio of 12 for 6 h TOS tests. The best results were obtained for the catalyst modified with both CeO₂ and MgO. In fact, the addition of these oxides resulted in a synergic effect that decreased the coke formation and favored the WGS reaction [240]. Furthermore, Charisiou and co-authors [241] performed a comparative analysis between Ni/CaO-MgO-Al₂O₃ and Ni/Al₂O₃ catalysts, which showed how the addition of CaO-MgO led to smaller Ni particles, increased the basicity and the surface amount of the Ni⁰ phase, thus resulting in better GSR results. The activity and stability tests carried on the two catalysts showed a different distribution of products, as the modified support favored H₂ and CO₂ production (enhancement of the WGS reaction). Moreover, this proved that the deactivation can be prevented with the addition of CaO and MgO to the support. In addition, the modified support also led to a lower amount of coke being deposited on the catalyst's surface, altering its nature, which based on the Raman analysis appeared to be less graphitic than that deposited on the unmodified Ni/Al₂O₃ catalyst. A study concerning the support roles for Pt-based catalysts in the GSR was carried out by

de Rezende et al. [28]. Several layered double-hydroxides containing Mg and Al (Mg/Al ratios of 3 and 5) as supports were tested. Specifically, four catalysts were prepared, two containing hydrated layered supports, PtMg₅Al-H and PtMg₃Al-H; and two containing mixed calcined oxides, PtMg₅Al-O and PtMg₃Al-O. Subsequently, the catalysts were submitted to GSR time-on-stream stability tests at 600 °C for 250 min, during which PtMg₅Al-H showed a stable conversion rate of ~85%, while all the other catalysts exhibited losses in activity. Moreover, the authors presented a correlation between the amount of carbon deposited on the catalysts and the degree of deactivation, thus pointing out the minor contribution of carbonaceous materials derived from intermediate organic liquid compounds on the deactivation processes. This study is in contrast with what is usually found in the literature, as reaction intermediates adsorbed on the catalysts are generally considered responsible for deactivation of catalysts. An interesting study evaluated the effect of the support on Co-based catalysts adopting alumina, niobia, and 10 wt.% niobia/alumina. The three prepared catalysts containing 20 wt.% CoO were tested under 30 h of GSR reaction at 500 °C with GHSV = 200,000 h⁻¹. In the first 8 h of reactions, complete glycerol conversion was obtained for CoNb, while the rate was ~90% for CoNbAl and ~80% for CoAl. Subsequently, after 24–26 h, a strong deactivation trend was detected for all catalysts, especially for CoNb. Indeed, from the analysis of the product distribution as a function of time, it was evaluated that even though the conversion was higher for CoNb, the gas production was low, thus indicating the probability of coke formation during the process. The catalyst that showed the best stability during the reaction was CoAl, with a decrease observed only after 26 h; these results were probably associated with the higher cobalt dispersion obtained for this catalyst. However, the catalyst supported by both Nb and Al presented the best values for H₂ production during the first 8 h of reaction. On the contrary, CoAl showed reduced hydrogen formation and was also characterized by the lowest amount of deposited coke, thus suggesting a coke formation mechanism based on the hydrogenation reaction of CO and CO₂. Conversely, looking at the H₂ production results, the authors assumed that the coke formed on CoNb and CoNbAl catalysts was mainly caused by the CO disproportionation, thus excluding hydrogen. A further analysis of the nature of the formed carbon revealed more amorphous coke deposited on CoNb and CoNbAl, while the deposits on the CoAl catalyst were predominantly graphitic [242]. The support effect on the stability of the catalysts was also investigated for glycerol dry reforming (GDR). In particular, a comparison between Ni catalysts supported on CaO and ZrO₂ pointed out the differences in the two support species. With this purpose, several catalysts were prepared by wet impregnation on both CaO and ZrO₂, increasing the amount of Ni (5%, 10% and 15%); moreover, the bare supports and the catalysts were also characterized by means of BET surface area determination tests, SEM analysis, XRD technique tests, and TGA and TPR analysis. Afterwards, the prepared catalysts were tested by the authors in stability experiments, which were carried out in a fixed-bed reactor at 700 °C and at atmospheric pressure over 3 h in time-on-streams. This resulted in better performances for the 15%Ni/CaO catalyst, characterized by a glycerol conversion rate of 30.52% and a hydrogen yield rate of 23.06%. For the other tested catalysts, the performances decreased in the order of 10% Ni/ ZrO₂ > 5% Ni/ CaO > 10% Ni/ CaO > 15% Ni/ ZrO₂ > 5% Ni/ ZrO₂. The better outcomes achieved for the 15%Ni/CaO were found to be in agreement with the characterization results, which proved better interactions between Ni and CaO, better metal dispersion, and greater surface area results in comparison with Ni/ZrO₂, also resulting in smaller crystallite sizes for NiO species [243]. Lee et al. [244], through a comparison of Ni-supported catalysts (Ni/LaAlO₃, Ni/CeO₂, Ni/MgO, and Ni/MgAl) regarding glycerol aqueous-phase reforming (GAPR), highlighted the strong dependency of the glycerol conversion and hydrogen yield on the type of support and the Ni loading. The support influence was investigated by the authors on 15 wt.% Ni catalysts supported on the four abovementioned species. In the activity tests at 250 °C and 20 bar, with LHSV = 5 h⁻¹, the catalyst 15%Ni/LaAlO₃ showed the best outcomes, with a glycerol conversion rate of 35.8% and a H₂ selectivity rate of 67.2%. Next, under the same conditions, four LaAlO₃-supported catalysts with 5, 10, 15, and 20 wt.% Ni were tested, confirming that the best performances were obtained with the 15% Ni. 15%Ni/ LaAlO₃ product. The selectivity was also investigated with a 20 h TOS test, during which

high CO₂ and H₂ yields were obtained, while low CO selectivity was achieved due to the WGS reaction. Moreover, the analysis of the spent catalysts revealed the presence of some agglomerated carbon particles on the surfaces of Ni/MgAl, Ni/CeO₂, and Ni/MgO. Conversely, the amount of deposited carbon was small and it was in a fibrous form in the case of the Ni/LaAlO₃ catalyst, thus highlighting the high resistance to coking of the catalyst, which was probably related to the migration of mobile oxygen from the support (LaAlO₃) to the metallic Ni particles [244]. In the study by Espinosa-Moreno and co-authors on Ir-based catalysts for H₂ production through GAPR, a comparison was carried out between La₂O₃ and CeO₂ as supports. The catalytic tests performed at 270 °C and 58 bar showed better values for H₂ production with La₂O₃ catalysts compared to CeO₂-supported catalysts due to the higher pore volume and metal–support interactions obtained using lanthana [236]. As can be appreciated in Figure 19, comparing the performances of IrNi/La₂O₃ and IrNi/CeO₂, much higher carbon-to-gas conversion rates were obtained when using lanthana as the support.

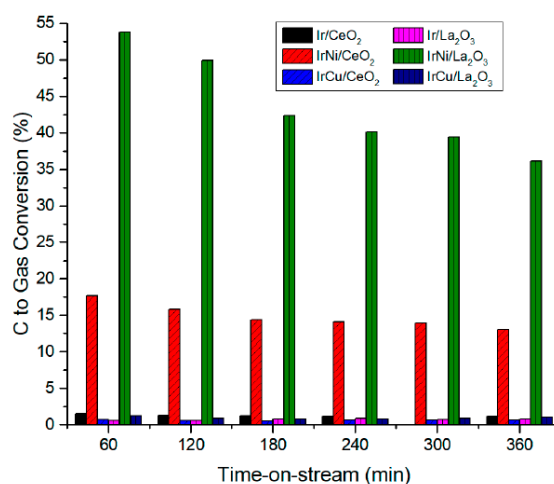


Figure 19. Carbon-to-gas conversion (%) as a function of the time-on-stream (min) stability test carried out at 270 °C and 58 bar [236].

4.3. The Effect of the Addition of Promoters

In this paragraph, the effects of promoters on the stability of various catalysts for glycerol reforming is discussed. In fact, a further strategy to inhibit catalyst deactivation is the adoption of additives and promoters, in order to create specific surface centers, which are mainly acidic or basic, bimetallic, or redox sites [245]. The effect of the addition of promoters to Ni/Al₂O₃ for the GSR has been widely studied in literature. Lima et al. investigated the consequences of the addition of Mg, finding an increase in the Ni dispersion and in its resistance to sintering and a decrease of the catalysts' acidity, thus promoting the stability of the catalysts. The addition of Mg also resulted in a lower amount of deposited coke, which was more graphitic [246]. A supplementary investigation on the effect of the addition of Mg to Ni/Al₂O₃ confirmed that its addition promotes the basicity of the catalyst and results in higher Ni dispersion, thus favoring the catalytic performance and lowering the carbon formation. Indeed, Dieuzeide et al. [247] pointed out that with an optimal loading of Mg of 3 wt.%, the amount of coke obtained was approximately half of the amount obtained without Mg. In addition, correlations between the structure of the deposited carbon, the Ni particle size, and the Mg presence were evaluated, since it was previously observed that a decrease in the Ni particle size and an increase in the Mg loading resulted in an increase of the degree of graphitization of the formed coke. Demsash et al. [248] evaluated the effect of ceria-promoted Ni-alumina catalysts in GSR by varying the amounts of nickel and ceria (5, 10, and 15 wt.% Ni, and 5 and 10 wt.% Ce). Among the prepared catalysts, 10Ni/Al₂O₃/5CeO₂ exhibited the best results in terms of activity and stability, with product distribution remaining almost stable over the 16 h TOS test at 650 °C. The Ce-promoted catalyst also showed the lowest coking activity, as a result of the inhibition effect of ceria to the formation of coke deposits; indeed, CeO₂ promotes

the hydration of the support. Carrero et al. [231] investigated the addition of Cu, Co, and Cr to a Ni/SBA-15 catalyst for GSR applications at 600 °C, involving a steam/carbon ratio of 2 and a WHSV of 7.7 h⁻¹ for a 5 h TOS test. During the stability tests, all the catalysts showed glycerol conversion rates above 85 mol%. In particular, glycerol conversion decreased following the order of Ni-Cr/SBA-15 > Ni-Co/SBA-15 > Ni/SBA-15 > Ni-Cu/SBA-15 along the reaction time, as can be seen in Figure 20.

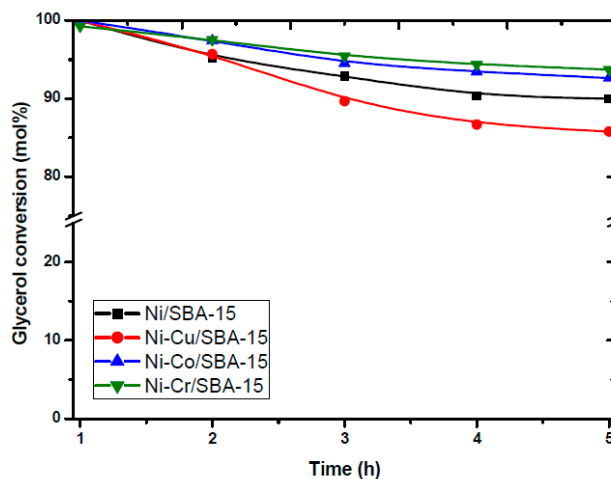


Figure 20. Conversion of glycerol over the Ni-(Cu,Co,Cr)/SBA-15 catalysts (T = 600 °C, P = 1 bar, WHSV_{glycerol} = 7.7 h⁻¹, water/glycerol = 6 mol/mol) [231].

Catalyst deactivation has been shown to be correlated with the amount of coke deposited, increasing in the order of Ni-Cr/SBA-15 < Ni-Co/SBA-15 < Ni/SBA-15 < Ni-Cu/SBA-15. Focusing attention on the product distribution during the reaction with the Ni-Cu/SBA-15 samples, the catalyst characterized by the highest deactivation and largest amount of coke deposition also enhanced the formation of methane and carbon monoxide, while lower amounts of carbon dioxide and hydrogen were produced. Moreover, for the Ni-Cr/SBA-15 samples, the highest hydrogen concentrations were detected in the gas stream. Regarding Ni-Co/SBA-15, despite the high glycerol conversion values obtained, low H₂ production was achieved—even lower than Ni/SBA-15, possibly due to the lower ability of Co than Ni to break the C-C bond. SEM images of the catalysts pointed out the presence of carbon nanofibers on Ni-Cu/SBA-15 and Ni-Co/SBA-15, while no formation of carbon nanofibers was detected by the SEM analysis on Ni-Cr/SBA-15. Subsequently, Ni-Cr/SBA-15 has been tested with a 60 h TOS protocol, which revealed good stability, with a glycerol conversion rate above 93% throughout the time period. Prior to investigating the promotion of Ni catalysts, the same authors evaluated the influence of additives on Co-catalysts in GSR. The study was focused on the comparison between Co/SBA-15 and promoted Co-M/SBA-15 with M/Zr, Ce, or La catalysts. The tests, which were carried out at 500 and 600 °C, with a water/glycerol ratio of 6 and a WHSV of 7.7 h⁻¹, showed that the addition of promoters significantly improved the stability of Co/SBA-15, especially at 500 °C, where the non-promoted catalyst suffered a drastic deactivation (from 98% to 75%) in the first 2 h. Among the promoted catalysts, Co/Ce/SBA-15 ensured the best results, with a glycerol conversion rate of ~100% during the 5 h time-on-stream test; moreover, despite the higher activity of this catalyst, the amount of coke deposited on its surface was lower compared to that observed for Co/SBA-15 (0.025 g_{coke}·g_{cat}⁻¹·h⁻¹ for Co/Ce/SBA-15 and 0.028 g_{coke}·g_{cat}⁻¹·h⁻¹ for Co/SBA-15). The products distribution analysis also pointed out that the use of Co/Ce/SBA-15 led to higher CO₂ and H₂ concentrations, while the CO formation was partially suppressed, highlighting the tendency of ceria to improve the oxygen mobility and water reactivity, enhancing the water–gas shift reaction. On the other hand, the addition of La and Zr resulted in lower hydrogen production; furthermore, the presence of ethylene was detected on Co/Zr/SBA-15, possibly caused by the enhancement of the dehydration reactions on the zirconium acid sites. Co/Ce/SBA-15 was then tested with a 50 h TOS test, during which high stability was reached

(glycerol conversion rate of ~100%). However, the amount produced hydrogen decreased, while the methane concentration increased. Moreover, the amount of coke was found to be higher and the authors suggested the possibility of a secondary reaction, such as $C+2H_2\leftrightarrow CH_4$ [249]. The advantages gained by the addition of Mg to Ni catalysts were verified by Veiga and co-workers, who studied glycerol steam reforming with nickel supported by activated carbon. During stability tests at 650 °C, Mg-promoted catalysts, among other promoters (MgO, La₂O₃, Y₂O₃), showed higher initial conversion and lower deactivation rates as a result of the capability of Mg to enhance the steam adsorption and stabilize Ni against sintering [250]. Other strategies used to improve the stability of catalysts for glycerol steam reforming involved the development of new types of catalysts and their subsequent doping with additives. Nickel, as a promoter for Fe/Mg-containing metallurgical waste, was prepared via solid-state impregnation of Ni into the structure of the metallurgical residue. Its stability was evaluated at 580 °C and 1 atm with a 48 h of TOS test. The developed catalyst exhibited good stability, with a glycerol conversion rate of ~90% and a hydrogen yield rate of ~80%; moreover, the amount of coke formation was low ($2.7 \text{ mg}_{\text{coke}} \text{ g}_{\text{cat}}^{-1} \text{ h}^{-1}$) and its nature was filamentous. This study also evidenced the ability of Mg to activate steam and promote the water–gas shift reaction [251]. An easily reducible NiAl₂O₄ spinel was developed using a novel method from a Ni–Al mixed-metal alkoxide, which was tested for use in GSR and was shown to have a highly porous structure and surface area. Moreover, the effect of the addition of 10 wt.% CeO₂ the catalyst stability was evaluated. The TOS tests performed at 630 °C and 1 atm for 16 h showed the high potential of the catalyst, characterized by low coke formation ($0.0004 \text{ g}_{\text{coke}} \text{ g}_{\text{cat}}^{-1} \text{ h}^{-1}$). Indeed, the addition of ceria diminished the coke deposits and favored their gasification. Additionally, the formation of a well-dispersed CeAlO₃ phase hindered the growth of filamentous carbon [245]. The role of CeO₂ as a promoter was also studied by Dobosz et al. [252], who evaluated its addition to a calcium hydroxyapatite (HAp)-supported cobalt catalyst. During the TOS stability test, which was carried out at 800 °C for 6 h, the catalyst doped with ceria (10Co–Ce/Hap) was stable than the 10Co/Hap catalyst. In fact, even if it a decrease in the hydrogen selectivity was observed, this effect was slower than the trend observed for the undoped catalyst. Ramesh et al. focused their attention on the influence of copper on perovskite catalysts for GSR, comparing a perovskite catalyst with two copper decorated perovskites (LaNi_{0.9}Cu_{0.1}O₃ and LaNi_{0.5}Cu_{0.5}O₃). Comparing their activity, better results were obtained for LaNi_{0.9}Cu_{0.1}O₃, which had a glycerol conversion rate of 73% and a hydrogen selectivity rate of 67%. The stability of the 0.1%-copper-decorated perovskite was confirmed by tests carried out at 650 °C, S/C = 3, and LHSV = 10,000 h⁻¹, during which the catalyst exhibited an almost constant product distribution over the 24 h TOS test. The characterization of the spent catalysts showed the presence of small amounts of graphitic carbon in the perovskites without copper (detected by TGA analysis, in which two oxidation peaks were observed at 550 and 600 °C). Conversely, the addition of copper resulted in only one oxidation peak, suggesting the presence of only amorphous carbon on the surface of the spent catalyst [33]. The Ni/Al₂O₃ catalyst and the improvements obtained with the addition of promoters were also studied in the development of the glycerol dry reforming (GDR) process. Harun and co-authors evaluated the effect of the Ag promotion via the preparation and testing of α-alumina-supported catalysts containing 15% Ni; in particular, four catalysts with Ag loading rates of 0 wt.%, 1 wt.%, 3 wt.%, and 5 wt.% were tested at 700 °C for 3 h, with a glycerol/carbon dioxide feed ratio of 1:1. The results showed that even if similar trends were shown by all of the catalysts (increase of the glycerol conversion in the first 0.5 h followed by a decrease after 1 h and a final stabilization), among the investigated catalysts, Ag(3)-Ni/Al₂O₃ gave the best glycerol conversion result (33.5%). Hence, this catalyst was tested with a 72 h stability test at 800 °C, during which the glycerol conversion firstly decreased from the 46% to the 33% after 10 h, and then remained almost stable for the next 60 h. After 10 h of reaction, H₂ and CO concentrations increased, while CH₄ decreased; the authors suggested that coke gasification by water may have been responsible. TGA analysis performed on the spent catalyst highlighted the presence of low- and high-temperature oxidation peaks, suggesting the presence of both amorphous and graphitic carbon deposits, as was further confirmed by the SEM

images, in which it was possible to appreciate the presence of encapsulated solid carbon deposits and filamentous (whisker-like) carbon deposits [31]. The addition of lanthanum to Ni-based catalysts was also investigated in the GDR. A 3wt.% La-promoted Ni/Al₂O₃ in comparison with the unpromoted catalyst led to better metal dispersion, as evaluated by the increase in the specific surface area and the decrease of the crystallite size (La-promoted catalyst: BET = 96 m² g⁻¹, crystallite size = 9.1 nm; unpromoted catalyst: BET = 85 m² g⁻¹, crystallite size = 12.8 nm). The catalysts stability was tested with a 72-h time-on-stream test at 750 °C and 1 atm with WHSV = 3.6·10⁻⁴ mL g⁻¹ h⁻¹, during which no severe deactivation was encountered [253]. Regarding the aqueous-phase reforming of glycerol (GAPR), Reynoso et al. compared two Pt/CoAl₂O₄ catalysts (Pt loadings of 0.3 wt.% and 1 wt.%) and monometallic Pt/alumina and Co/alumina in 100 h time-on-stream experiments. The results of the tests, which were performed at 260 °C and 50 bar with WHSV = 0.68 h⁻¹, pointed out that while for the bimetallic catalysts the glycerol conversion was high (above 99%) and stable during time-on-stream testing, the monometallic catalysts suffered from deactivation. Similar outcomes were also obtained in terms of the conversion of carbon to gas, which was almost stable at 95% for the bimetallic catalysts, while CoAl and PtAl showed decreases of 36% and 30%, respectively. Raman spectroscopy and temperature-programmed hydrogenation (TPH) were used to characterize the spent catalysts. From the Raman spectra, the presence of ordered graphite-like structures on the monometallic catalysts was evaluated, while no carbonaceous deposits were encountered on the bimetallic formulations. Through the TPH analysis, the presence of a low temperature peak (T = 200 °C, ascribable to the hydrogenation of the most amorphous carbon) was detected on the Pt-containing samples, suggesting that the hydrogenation of carbon deposits could happen in the proximity of the well-dispersed Pt centers as a consequence of the spillover effect. However, the CoAl catalyst showed a higher amount of deposited carbon (13.5 μmol_C·g_{cat}⁻¹), while for Pt-containing samples the values were much lower (1.2–1.9 μmol_C·g_{cat}⁻¹) [254]. Furthermore, Pendem et al. [255] investigated the addition of potassium to hydrotalcite (Pt-KHT) catalysts for GAPR, finding that the K promotion increased the basicity of the catalyst and improved the hydrogen production. The results of the stability test carried out at 250 °C showed a hydrogen selectivity of 67.4% after 3 h of reaction.

Table 3 provides the values for the carbon formation rate obtained from the glycerol steam reforming stability tests performed in the various considered studies. An analysis of the tendency to form coke pointed out that both the active phase and the support play key roles in the final amount of deposited carbon. Among the metals used for active phases, Ni showed better stability; indeed, all the catalytic formulations based on Ni showed lower amounts of carbonaceous deposits. In particular, the best carbon formation rates were seen for the 10Ni/Al₂O₃ and 10Ni/Al₂O₃/5CeO₂ catalysts tested by Demshash et al. (0.00067 and 0.000424 g_{coke}·g_{catalyst}⁻¹·g_{carbon,fed}⁻¹·h⁻¹, respectively) [248]. Moreover, the comparison between these two catalysts also highlighted that the support modification obtained using CeO₂ can lead to a further performance increase for the catalysts. However, the eventual use of promoters in the preparation of catalysts is also of fundamental importance. Comparing the performances of the catalysts prepared by Carrero et al. [231,249], it is possible to observe that for SBA-15, the catalyst prepared using Ni as the active phase was characterized by high rates of carbon formation; conversely, the addition of Co and Cr resulted in an improvement of the obtained results. Indeed, from the investigation of the stability tests performed on Ni-Co/SBA-15 and Co/SBA-15 (stability tests were carried out at 600 °C and WHSV = 7 h⁻¹), it seems that the Ni did not affect the formation of coke, as the carbon formation rate values for the two catalysts were equal. In addition, among all the catalysts tested by the authors, the lowest carbon formation rates were obtained with a catalyst based on Ni (Ni-Cr/SBA-15 carbon formation rate = 3.009 g_{coke}·g_{catalyst}⁻¹·g_{carbon,fed}⁻¹·h⁻¹), thus confirming the better results obtained for Ni catalysts for glycerol steam reforming.

Table 3. Carbon formation rate for various catalysts used for glycerol steam reforming.

Catalyst ^a	Operative Conditions ^b	T (°C)	WHSV ^c (h ⁻¹)	X Glycerol (%)	Carbon Formation Rate ^d (Multiplied for 1000)	Ref.
Glycerol steam reforming						
8Ni/Al ₂ O ₃ 8Ni/ 4La ₂ O ₃ -Al ₂ O ₃	m _{cat} = 200 mg 31 v.v. % C ₃ H ₈ O ₃ and H ₂ O (63% H ₂ O, 7% C ₃ H ₈ O ₃ and 30% He) TOS = 4 h	700	GHSV = 50,000 mL g ⁻¹ h ⁻¹	~75 ~80 After 4 h	0.141 0.152	[221]
Rh/alumina	0.1 mL min ⁻¹ of aqueous glycerol, P = 4.5 bar m _{cat} = 800 mg TOS = 13 h	400	7.8	~92 After 13 h	0.045	[227]
14.5Ni/SBA-15 14.5Ni-4Co/SBA-15 14.3Ni-3.6Cr/SBA-15 15Ni-4Cu/SBA-15	S/C = 2 Water/glycerol = 6 mol/mol m _{cat} = 300 mg TOS = 5 h	600	7.7	~92 ~94 ~95 ~88 After 5 h	27.879 5.092 3.009 51.157	[231]
8Ni/Al ₂ O ₃ 8Ni/CaO-MgO-Al ₂ O ₃	m _{cat} = 200 mg 31 v.v. % C ₃ H ₈ O ₃ and H ₂ O (63% H ₂ O, 7% C ₃ H ₈ O ₃ and 30% He) TOS = 20 h	600	GHSV = 50,000 mL g ⁻¹ h ⁻¹	~70 ~80 After 20 h	0.057 0.048	[241]
10% CeO ₂ addition to NiAl ₂ O ₄ spinel	m _{cat} = 500 mg Water/glycerol = 9 (glycerol solution)/Ar = 1 TOS = 16 h	630	GHSV = 19600 cm ³ g _{cat} ⁻¹ h ⁻¹	90 After 16 h	0.16	[245]
10Ni/Al ₂ O ₃ 10Ni/Al ₂ O ₃ /5CeO ₂	m _{cat} = 1 g 30 wt.% glycerol feed TOS = 16 h	650	12	-	0.00067 0.000424	[248]
7Co/SBA-15 7Co-8.5Zr/SBA-15 7Co-8.5Ce/SBA-15 7Co-8.5La/SBA-15	S/C = 2 Water/glycerol = 6 mol/mol m _{cat} = 300 mg TOS = 5 h	600	7.7	~75 >90 >90 >90 After 5 h	5.092 5.555 5.555 4.629	[249]
12.5Ni-UGS	m _{cat} = 500 mg S/C = 3 Water/glycerol = 9 (Water+glycerol)/Ar = 1:4 TOS = 48 h	580	GHSV = 20600 cm ³ g _{cat} ⁻¹ h ⁻¹	90 After 48 h	0.17	[251]

Note: ^a The metal or oxides loadings are intended for the weight of the catalyst; ^b refers to the glycerol mass flow rate; ^c g_{coke}·g_{catalyst}⁻¹·g_{carbon, fed}⁻¹·h⁻¹.

5. Other Bioalcohol Reforming

In recent years, hydrogen production through reforming processes has been widely studied. In addition to the most investigated biosources, other bioalcohols have been explored as models for hydroxyl-bearing oxygenates. Indeed, research towards the reforming processes of model compounds is a powerful tool that can be used to approach the more complex implementation of bio-oil for H₂ production [256]. The paucity of available literature concerning reforming of butanol (C₄H₉OH) and propanol (C₃H₇OH), which are higher molecular weight alcohols and minor constituents of bio-oil in comparison with methanol or ethanol, makes this an interesting topic. Indeed, as reported in Figure 21, numerous advantages are gained through the use of butanol as a biohydrogen source [257,258]. Along with the other alcohols, reforming of butanol and propanol are processes in which the use of catalysts plays a key role in reactivity regarding the complete conversion, hydrogen yield, and stability. Indeed, different catalysts may induce different reaction pathways; therefore, the selection of a proper catalytic formulation is of prime importance in order to reduce the promotion of undesired by-products and to inhibit coke formation. The mechanisms that lead to coke formation in the reforming processes of the two investigated alcohols are different. Butanol reforming proceeds through numerous pathways; direct reforming and the formation of 1-butene, butyraldehyde, and coke deposits are mainly linked to butyraldehyde rather than 1-butene [259,260]. Instead, regarding the coke formation in the reforming process of propanol, the dehydration and dehydrogenation reactions lead to the formation of propene and propanal, which can subsequently decompose to CO and ethane or condense to form heavier compounds, leading to catalyst deactivation [256].

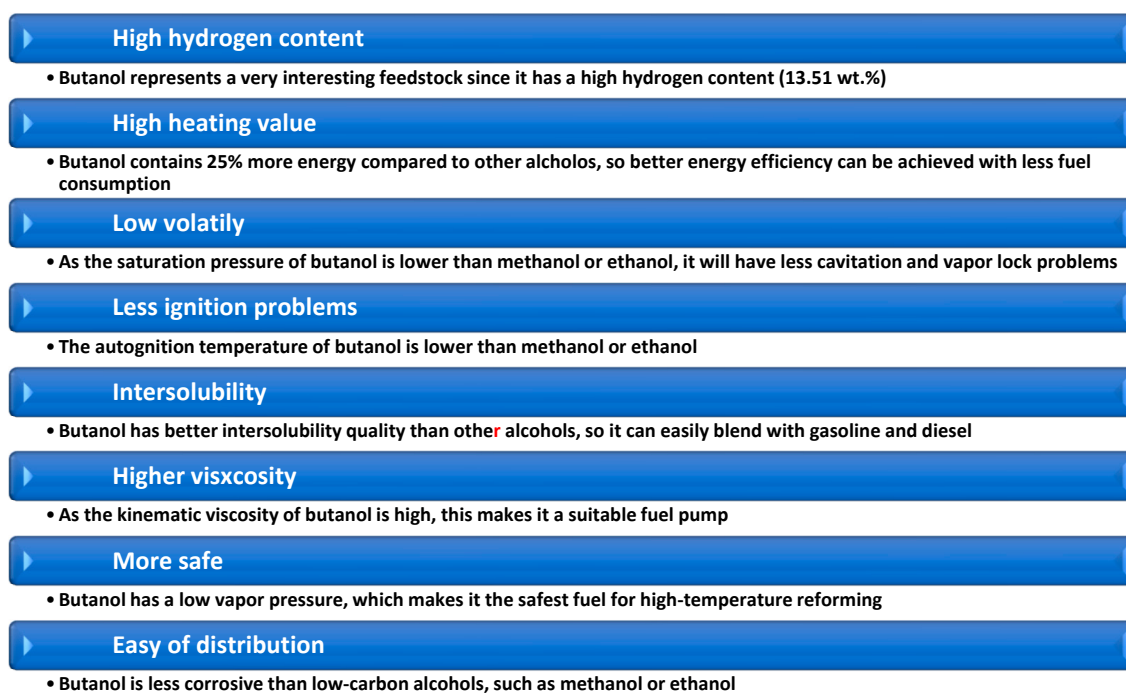


Figure 21. Advantages of using butanol [259].

The metal phase ability to activate the alcohol, the role of the support in the dispersion of the active phase and the eventual addition of promoters are crucial aspects to be taken into account in order to disadvantage the formation of coke, thus promoting catalytic stability [259].

5.1. The Influence of the Active Phase

This section focuses on the roles of active species selection in catalytic performance for butanol reforming; the stability of nickel-, ruthenium-, and platinum-based catalysts is discussed below.

The activity of nickel, as the most-used metal for reforming catalysts, has also been investigated in the steam reforming of butanol. Dhanala et al. [261] performed a comparative study of steam reforming (SR) and oxidative steam reforming (OSRB) of isobutanol on Ni/ γ -Al₂O₃ catalysts with different nickel loadings. Stability tests were carried out by the authors on the 30NiAl sample for the OSRB at 600 °C with WHSV = 7.6 h⁻¹ for 12 h of time-on-stream testing, during which 100% carbon conversion to gaseous products persisted over time. The products distributions after the first 2 h of testing reached steady-state values, with a H₂ yield rate of ~60%, confirming the stability of the tested catalyst. A further investigation on the spent catalysts showed the presence of complex criss-crossed carbon nanofiber networks on Ni/ γ -Al₂O₃ catalysts for both SR and OSRB, probably caused by the decomposition of carbonaceous compounds. The authors also tested catalysts with different Ni loadings (in particular 30NiAl and 20NiAl) and the XRD analysis revealed that 30NiAl has a larger average crystallite size than 20NiAl. Moreover, the further characterization of the two spent catalysts pointed out a correlation between the extent of carbon deposits and the nickel crystallite sizes, while the carbon nanofiber networks over 30NiAl were found to be denser and bigger than 20NiAl. In addition, the O₂ addition to the common steam reforming led to less and smaller carbon nanofibers for the OSRB compared to SR. An investigation of Ni catalysts with various particle sizes (3.6–8.8 nm) was also carried out by Wang et al. [262] through the preparation and testing of mesoporous MgO-supported Ni catalysts for the butanol steam reforming (BSR). The different nickel particle sizes were achieved by the addition of a specific amount of nickel precursor. The as-prepared catalysts with different Ni loadings were denoted as Ni_xO/MgO, with x = 0.04, 0.08, 0.12, 0.15, and 0.20. From the activity tests, Ni_{0.12}O/MgO (Ni size of 5.62 nm, as assessed by TEM analysis) showed better BSR results; thus, the catalyst

was also submitted to a stability test for 20 h at 450 °C ($S/C = 20$, liquid flow rate = $5.5\text{ mL}\cdot\text{h}^{-1}$). During the first 10 h of reaction, butanol conversion declined from 95.2% to 92.1% and the H_2 selectivity declined from 68.1% to 64.9%. Then, in the following 10 h, their values remained almost unchanged; moreover, the tests on the spent catalyst showed no severe coke deposition. A comparison between the activity of Ni and Co was carried out by Yadav and co-authors through the investigation of two multiwalled carbon-nanotube-supported catalysts. From the activity tests, Ni/CNT showed higher butanol conversion and hydrogen yield values for all the investigated temperatures (500, 450, 400, and 350 °C); consequently, the catalyst was tested with 20 h of time-on-stream testing at 500 °C ($W/F_{A0} = 4.2\text{ g h}\cdot\text{mol}^{-1}$). Only slight decreases in results were observed (butanol conversion decreased from 63.6% to 59.6% and H_2 yield decreased from 0.63 mol/mol to 0.57 mol/mol) [263]. A comprehensive study on the deactivation mechanism of a 0.5 wt.% Rh/ZrO₂ catalyst involved in steam reforming and autothermal steam reforming (ATRB) of butanol was performed by Harju et al. [264]. Butanol conversion on the catalyst and the bare support was investigated by the authors for both processes at 500, 600, and 700 °C (S/C molar ratio of 4 and O_2/C molar ratio of 0.1). The results showed the highest performance at 700 °C, with an initial complete conversion for both SR and ATR on the Rh/ZrO₂ catalyst and the bare support. However, while the conversion of the catalyst remained almost constant for 23 h, butanol conversion with ZrO₂ collapsed within 15 min. The authors suggested that the deactivation of Rh/ZrO₂ was mainly caused by the coke deposits on and near the Rh nanoparticles as a result of butyraldehyde and condensation product formation. Moreover, the deactivation of the catalyst follows a different route depending on the operative temperature; while at 700 °C the formation of coke precursors is mainly caused by gas-phase reactions, at lower temperatures the formation of coke deposits takes place mostly through reactions on the catalysts' surfaces. Furthermore, Harju et al. [265] performed a study on the same type of catalyst (Rh/ZrO₂) used in the aqueous-phase reforming of n-butanol. Their attention was focused on the effect of the variation of the support particle sizes. The ZrO₂ support was crushed and sieved in order to obtain three catalysts with particle sizes in the range of 40–60, 60–100, and 250–420 μm. The stability tests, carried out at 220 °C and 35 bar with $\text{LHSV} = 150\text{ h}^{-1}$ for 4 h TOS, pointed out that the catalyst deactivation was faster for large support particles, due to the high concentrations of butyraldehyde inside the catalyst particles, which favored the formation of deposits caused by aldol condensation reactions. However, the catalysts with smaller support particle sizes (4–60 μm and 60–100 μm) also showed decreases in the butanol conversion, albeit with lower values. Regarding the selectivity towards gaseous products, the values were high and almost constant for 40–60-μm and 60–100-μm Rh/ZrO₂ catalysts (from 99% to 97% in 2.5 h), whereas for the catalyst with the larger particle size this dropped off severely over time. Moreover, the elemental analysis of the spent catalyst revealed that the formation of coke deposits increased as the particle sizes of the catalysts increased. Yadav et al. [266] compared the activity and stability of two noble metal catalysts, Pt/Al₂O₃ and Pd/Al₂O₃, for butanol steam reforming. The 20-h time-on-stream investigations conducted at 500 °C exhibited a decrease from 82.5% to 74.1% for butanol conversion with Pt/Al, while for the Pd/Al catalyst the conversion decreased from 80.5% to 74.1%. The H_2 yield decreased from 0.37 to 0.28 mol/mol for Pt/Al and from 0.3 to 0.24 mol/mol for the Pd/Al catalyst, thus pointing out the good stability of both noble-metal-based catalysts. Wang et al. [256] performed a study on n-propanol steam reforming with ruthenium and ruthenium-nickel bimetallic catalysts supported on ceria-alumina oxides, analyzing the influence of the variation of the loading of nickel, loading of ceria, and the calcination of the ruthenium precursor. The catalysts were denoted as AxCyN3Rc or AxCyN3Rnc , where “nc” was used if the ruthenium precursor not calcined and “c” was used if it was calcined; moreover, a stood for the alumina carrier, x was the wt.% loading of the ceria, and y was the weight percent loading of nickel. In this section, the contributions of the calcination of Ru and Ni loading will be discussed, while the effect of the addition of ceria will be discussed in the following section. The investigation of the calcination of the Ru precursor pointed out that poor ruthenium dispersion is achieved after the calcination of the precursor salt, worsening the steam reforming results. On the other hand, from the tests carried out on catalysts with different Ni loading values, it was seen

that the increase of Ni from the 2.5% to 10% resulted in a better n-propanol SR activity due to the capability of Ni to activate the n-propanol molecules. Moreover, from the comparison between the catalysts with and without Ni, a lower H₂ formation rate and CO selectivity were found in the absence of Ni, while CH₄ was higher, suggesting that Ru is less active than Ni in the conversion of methane.

5.2. The Role of the Support

Various supports were selected for butanol reforming. This section describes the effect of the support choice on catalyst stability for butanol reforming.

Due to its high surface area, alumina has been widely adopted as a support for reforming catalysts; however, it has also been documented that the acidic nature of such a support may result in an enhancement of coke deposits, mainly caused by dehydration reactions [259]. Bikzarra et al. [267] investigated the effect of Al₂O₃ modifications by CeO₂, La₂O₃, and MgO for Ni-based catalysts, since their basicity could moderate the acid properties of alumina. Moreover, CeO₂ and La₂O₃ were also adopted to improve the metal dispersion and prevent sintering, while MgO improved the catalysts' strength and enhanced the steam adsorption. Hence, five catalysts were prepared (Ni/Al₂O₃, Ni/CeO₂-Al₂O₃, Ni/La₂O₃-Al₂O₃, Ni/MgO-Al₂O₃) and tested in the n-butanol SR at three temperatures (600, 700, and 800 °C), with a S/C ratio of 5. Among all the catalysts, Ni/CeO₂-Al₂O₃ showed the highest performance for all the investigated temperatures, reaching equilibrium hydrogen yields at 700 and 800 °C, while Ni/MgO-Al₂O₃ exhibited the lowest hydrogen yield in all the performed tests. The adoption of Ni/La₂O₃-Al₂O₃ resulted in experimental results that were much lower than those predicted by thermodynamic equilibrium. Additionally, the CeO₂-supported catalysts also led to high CO₂ selectivity values being obtained, suggesting the enhancement of the WGS reaction. On the other hand, reduced CO₂ selectivity values were obtained with the adoption of Ni/MgO-Al₂O₃, along with high C₂, C₃, and C₄ selectivity. Unfortunately, both CeO₂- and MgO-supported catalysts showed deactivation; for Ni/CeO₂-Al₂O₃, decreases in the H₂ yield rate and CO₂ selectivity were observed by the authors. XPS analysis on the spent catalysts showed different carbon species for investigated samples, covering 62% to 93% of the total area. Lobo and co-authors [268] evaluated the support modification effects for the aqueous steam reforming of 1-propanol. Three Pt/alumina catalysts were prepared through atomic layer deposition, obtaining ~1-nm layer of Al₂O₃, TiO₂, or CeO₂ (Pt-Al, Pt-Ti, Pt-Ce), which was tested at 230–260 °C and 69 bar in the presence of liquid water. All the catalysts demonstrated good activity for 1-propanol conversion; the results decreased in the order of Pt-Ti > Pt-Al > Pt-Ce. The authors suggested that the TiO₂ coating enhanced the rate of the Pt clusters, while the presence of CeO₂ had the opposite effect. Moreover, the characterization of catalysts showed that the coating of Al₂O₃ with both TiO₂ and CeO₂ led to a better Pt dispersion than that observed on the bare alumina, and since Pt-Al performed better than Pt-Ce, this suggested that the dispersion of the Pt particles was not the most critical aspect in determining the catalytic activity. Li et al. [269] investigated the impacts of the acidic sites on the coke formation in the steam reforming of 1-propanol through the comparison of Ni/Al₂O₃ and Ni/SiO₂; indeed, while on Ni/Al₂O₃ the presence of both Lewis and Brønsted acidic sites was observed, on Ni/SiO₂ only Lewis acidic sites were detected by the authors. The 4-h time-on-stream stability tests performed at 600 °C with a S/C ratio of 1.5 and a liquid flow rate of 0.12 mL·min⁻¹ showed that the 1-propanol conversion was high in both catalysts (~100% on Ni/Al₂O₃ and ~98% on Ni/SiO₂); however, the product distribution differed depending on the adopted support. For Ni/Al₂O₃, the yields of H₂ and CO₂ were only 40 and 30%, respectively, and there were significant amounts of CH₄ and CO. Additionally, for Ni/SiO₂, the methane formation was suppressed, resulting in increases of H₂, CO₂, and CO yields. The increased activity of Ni/SiO₂ compared to Ni/Al₂O₃ could be attributed to the presence of less-basic sites or the absence of Brønsted acidic sites on the silica-supported catalyst. Moreover, neither catalyst showed signs of deactivation over the time period. The TEM analysis carried out on the spent catalysts highlighted the presence of amorphous coke and carbon nanotubes on both the samples; however, the amounts and the characteristics of the deposits differed depending on the support. Indeed, Ni/Al₂O₃ displayed more amorphous coke deposits,

while coke deposits were mostly carbon-nanotube-shaped on Ni/SiO₂. Moreover, the diameter and length of the carbon nanotubes were higher on Ni/SiO₂ compared to Ni/Al₂O₃. The Ni/SiO₂ catalyst was found to promote the formation of carbon nanotubes; in fact, nanofiber-shaped carbon deposits were also detected on its surface. On the other hand, finer carbon nanotubes that were mostly hollow were observed for the Ni/SiO₂ sample, while the thicker ones were mainly solid. The reason for this result could be the different growth mechanisms of carbon nanotubes at different growth stages; in the early growth stage, coke was mainly deposited from the inside, while in the latter stages of growth, coke was deposited from the outside, thus increasing the diameter of the carbon nanotubes.

5.3. The Effect of the Addition of Promoters

In this section, the influence of the addition of promoters on the stability of the catalysts for butanol reforming is discussed. In particular, the addition of noble metals to reforming catalysts is a valuable feature that improves their coke resistance and stability. Indeed, despite their high cost, the addition of small percentages of noble metals (e.g., Pt, Pd, and Ru) could result in an enhancement of the metal dispersion and reducibility; moreover, they also possess high reforming activity, due to the enhancement of the steam adsorption on the catalysts' surfaces.

A study concerning the Pt, Pd, and Ru doping of Ni-Cu catalysts supported on a La-Mg mixed-metal oxide for butanol SR pointed out the benefits of the addition of noble metals, which resulted in the absence of coke deposits, thus increasing the stability of the catalysts. In particular, the stability of the catalysts, which was tested at 500 °C and 1 atm with GHSV = 3120 h⁻¹ for 30 h TOS, showed the better performance of the Pt-promoted catalyst, characterized by improved butanol conversion and hydrogen yield. Subsequently, in order to test the long-term stability of the investigated catalytic formulations, up to 10 cycles were carried out, during which the stability rates of the catalysts were in the following sequence: Ru > Pt > Pd. In fact, the Ru-promoted catalyst showed better stability, despite producing lower H₂ concentrations [270]. Furthermore, Sharma et al. [271] observed that promotion of Ru on Ni xerogel catalysts for the autothermal reforming of isobutanol resulted in improved hydrogen production and reduced coke formation. Indeed, the catalyst tested for 25 h TOS at 700 °C with SV = 217,000 h⁻¹, H₂O/C = 2, and O/C = 0.1 showed a decrease in hydrogen yield from 1.53 to 1.4, showing a slow decrease of the reforming extent. Moreover, on the catalysts' surfaces, very low carbon deposits were detected by the authors. Lei et al. [272] evaluated the advantages of the ZnO promotion on the performance of Pt/Al₂O₃ in the aqueous-phase reforming of 1-propanol. An improvement in the sintering resistance of the Pt nanoparticles was observed upon addition of Zn. In particular, three catalysts (Pt/ZnO/Al₂O₃, ZnO/Pt/Al₂O₃, and Pt/Al₂O₃) were prepared and tested for APR at 250 °C and 64 bar; the hydrogen selectivity decreased in the order of ZnO/Pt/Al₂O₃ > Pt/ZnO/Al₂O₃ > Pt/Al₂O₃. Indeed, ZnO/Pt/Al₂O₃ showed a H₂ formation rate of 50.5%. Moreover, both ZnO-promoted catalysts exhibited greater stability under APR conditions.

6. Conclusions

Bioalcohols reforming is a very active research area for clean hydrogen production. During the last five years, the issue of catalyst deactivation has been widely investigated for ethanol steam reforming and oxidative reforming, while only a few studies are available for dry reforming and aqueous-phase reforming. The strategies for minimizing carbon deposition and particle sintering involve the optimization of the dispersion of active species and the improvement of metal-support interactions. In this regard, numerous catalytic formulations have been proposed (mainly based on Ni, Co and Pt as the active phases), including bimetallic catalysts and samples containing additives, both of which were prepared using different routes and employing various salt precursors. The addition of promoters was also investigated as a valuable strategy to reduce the coke selectivity; at that end, different criteria have been proposed and the authors have studied the effects of promoter selection, promoter loading, preparation method, acidic-basic properties, as well as structural properties of the support. The operative conditions (temperature, space velocity, feeding composition, and ethanol

concentration in the reactant stream) also affect the amounts of carbon deposits on the catalysts' surfaces; the lowest carbon formation rates (of the order of 10^{-6} – 10^{-7} $\text{g}_{\text{coke}} \cdot \text{g}_{\text{catalyst}}^{-1} \cdot \text{g}_{\text{carbon, fed}}^{-1} \cdot \text{h}^{-1}$) were recorded for noble-metal-based and promoted catalysts. In particular, when ESR was performed over Ir- and Rh-based catalysts, the CFR value was among the lowest reported in the present review. Very low carbon formation rates were also measured in the presence of Pd, as well as over bimetallic Rh-Ni catalysts. Regarding the tests performed in the presence of oxygen, the highest stability was assured over the Pt-Ni/CeO₂-SiO₂ catalysts, as well as over Ru-based perovskites containing La as the promoter. During dry reforming of ethanol, the choice of ceria and zirconia as catalytic supports instead of alumina reduced the extent of the catalyst deactivation.

MSR is a very attractive alternative for hydrogen production due to the very low tendency for coke formation. Most of the published work on this topic has been focused on Cu-based catalytic systems; the low costs of these materials make them particularly attractive for industrial applications. More sophisticated catalytic formulations, including noble-metal-based catalysts, could provide highly efficient and stable systems, with improved performance in terms of resistance towards deactivation. However, few articles have been published on these catalysts, meaning it is currently hard to establish the real potential of these materials. Although there is high potential for the O₂-assisted process in terms of enhanced hydrogen productivity and the possibility to tune the methanol/oxygen ratio in the power generation, such systems do not seem to provide a valuable alternative to the MSR in terms of reducing the carbon formation rate. The use of alternative reactor configurations is very intriguing; membrane reactor studies have demonstrated the competitiveness of these systems, both in terms of hydrogen production and operating costs.

Bioglycerol reforming processes represent a promising route to improve the economic feasibility of the biodiesel industry. The catalytic transformation of bioglycerol into hydrogen is mainly limited by the undesired formation of coke deposits on the catalysts' surfaces, thus affecting the catalysts' stability, making this an unfeasible industrial process. Therefore, many research studies have been devoted to the deep understanding of the deactivation mechanisms and the possible ways to avoid this problem. In this regard, feasible modifications of Ni-based catalysts have been reported as promising methods to improve the hydrogen production. Moreover, further studies have been performed on the support modifications devoted to improve the basicity of catalysts (e.g., the addition of more basic oxides to high surface area supports, such as Al₂O₃) and on the effects resulting from the addition of promoters.

Among all the catalysts presented in this review, Ni-based catalytic formulations have shown better stability, being characterized by lower carbon formation rates, with reduced amounts of carbon deposits shown by 10Ni/Al₂O₃ and 10Ni/Al₂O₃/5CeO₂. Moreover, analysis on the influences of supports and promoters on the stability of catalysts has shown that both of these aspects contribute to reducing the amount of carbon formed. Particular attention has been given to the modification of supports that include more basic compounds (e.g., 10Ni/Al₂O₃/5CeO₂ presented fewer carbon deposits than 10Ni/Al₂O₃), as well as the use of metals as promoters (e.g., Cr, La, Ce). Reforming processes for other bioalcohols have also been investigated in this review, as powerful tools for approaching the more complex implementation of bio-oil in the field of H₂ production. In particular, butanol and propanol reforming processes have been analyzed, focusing on the influences of the active phase, supports, and eventual promoters on the stability of the catalysts and the coke formation. Indeed, for both bioalcohols, coke formation represents the main threat in the development process, and several actions can be taken to improve the stability of the catalysts.

Author Contributions: All authors have read and agreed to the published version of the manuscript. Conceptualization, V.P. and C.R.; methodology, M.M.; formal analysis, M.C. and M.M.; investigation, C.R. and M.M.; resources, V.P. and M.C. data curation, C.R.; writing—review and editing, C.R., M.C. and M.M.; visualization, V.P.; supervision, V.P.

Funding: This work has received funding from the European Union's Horizon 2020 research and innovation programme under the Marie Skłodowska-Curie grant agreement No 734561.

Conflicts of Interest: The authors declare no conflict of interest.

Abbreviations

APR	Aqueous-phase reforming
APRE	Aqueous-phase reforming of ethanol
ASRM	Autothermal steam reforming of methanol
ATR	Autothermal reforming
BET	Brunauer–Emmett–Teller surface area measurements
BSR	Butanol steam reforming
CCR	Carbon capture and recycling
CFD	Computational fluid dynamics
CFR	Carbon formation rate
CNF	Carbon nanofibers
CNT	Carbon nanotubes
DFT	Discrete Fourier transform
DRIFT	Diffuse reflectance infrared Fourier transform spectroscopy
DSC	Differential scanning calorimeter
EDR	Ethanol dry reforming
EDS	Energy-dispersive X-ray spectrometry
EDX	Energy-dispersive X-ray analysis
GAPR	Aqueous-phase reforming of glycerol
GDR	Glycerol dry reforming
GHSV	Gas hourly space velocity
GSR	Glycerol steam reforming
LHSV	Liquid hourly space velocity
MSR	Methanol steam reforming
MMT	Montmorillonite
OSRE	Oxidative steam reforming of ethanol
OSRM	Oxidative steam reforming of methanol
OSRB	Oxidative steam reforming of butanol
PEM	Polymer electrolyte membrane
PO	Partial oxidation
SEM	Scanning electron microscopy
TEM	Transmission electron microscopy
TGA	Thermogravimetric analysis
TOF	Turnover frequencies
TOS	Time-on-stream
TPD	Temperature-programmed desorption
TPH	Temperature-programmed hydrogenation
TPO	Temperature-programmed oxidation
TPR	Temperature-programmed reduction
WGS	Water–gas shift
WHSV	Weight hourly space velocity
X	Alcohol conversion
XPS	X-ray photoelectron spectroscopy
XRD	X-ray diffraction

References

1. Susmozas, A.; Iribarren, D.; Dufour, J. Assessing the life-cycle performance of hydrogen production via biofuel reforming in Europe. *Resources* **2015**, *4*, 398–411. [[CrossRef](#)]
2. Al-Maamary, H.M.S.; Kazem, H.A.; Chaichan, M.T. The impact of oil price fluctuations on common renewable energies in GCC countries. *Renew. Sustain. Energy Rev.* **2017**, *75*, 989–1007. [[CrossRef](#)]
3. Calles, J.A.; Carrero, A.; Vizcaíno, A.J.; García-Moreno, L.; Megía, P.J. Steam reforming of model Bio-Oil aqueous fraction using Ni-(Cu, Co, Cr)/SBA-15 catalysts. *Int. J. Mol. Sci.* **2019**, *20*, 512. [[CrossRef](#)] [[PubMed](#)]

4. Colmenares, J.C.; Colmenares Quintero, R.F.; Pieta, I.S. Catalytic dry reforming for biomass-based fuels processing: Progress and future perspectives. *Energy Technol.* **2016**, *4*, 881–890. [[CrossRef](#)]
5. Lisý, M.; Lisá, H.; Jecha, D.; Baláš, M.; Križan, P. Characteristic properties of alternative biomass fuels. *Energies* **2020**, *13*, 1448. [[CrossRef](#)]
6. Palma, V.; Barba, D.; Meloni, E.; Ruocco, C.; Martino, M. Chapter 2—Membrane reactors for H₂ and energy production. In *Current Trends and Future Developments on (Bio-) Membranes*; Basile, A., Napporn, T.W., Eds.; Elsevier: Amsterdam, The Netherlands, 2020; pp. 33–56. [[CrossRef](#)]
7. Alique, D.; Bruni, G.; Sanz, R.; Calles, J.A.; Tosti, S. Ultra-Pure hydrogen via co-valorization of olive mill wastewater and bioethanol in pd-membrane reactors. *Processes* **2020**, *8*, 219. [[CrossRef](#)]
8. Frusteri, F.; Bonura, G. 5-Hydrogen production by reforming of bio-alcohols. In *Compendium of Hydrogen Energy*; Subramani, V., Basile, A., Veziroğlu, T.N., Eds.; Woodhead Publishing: Oxford, UK, 2015; pp. 109–136.
9. Melikoglu, M.; Singh, V.; Leu, S.Y.; Webb, C.; Lin, C.S.K. Biochemical production of bioalcohols. In *Handbook of Biofuels Production*, 2nd ed.; Luque, R., Lin, C.S.K., Wilson, K., Clark, J., Eds.; Woodhead Publishing: Oxford, UK, 2016; pp. 237–258.
10. Datta, A.; Hossain, A.; Roy, S. An overview on biofuels and their advantages and disadvantages. *Asian J. Chem.* **2019**, *31*, 1851–1858. [[CrossRef](#)]
11. Ail, S.S.; Dasappa, S. Biomass to liquid transportation fuel via Fischer Tropsch synthesis—Technology review and current scenario. *Renew. Sustain. Energy Rev.* **2016**, *58*, 267–286. [[CrossRef](#)]
12. Behera, S.; Singh, R.; Arora, R.; Sharma, N.K.; Shukla, M.; Kumar, S. Scope of algae as third generation biofuels. *Front. Bioeng. Biotechnol.* **2015**, *2*. [[CrossRef](#)]
13. Seretis, A.; Tsiakaras, P. Crude bio-glycerol aqueous phase reforming and hydrogenolysis over commercial SiO₂Al₂O₃ nickel catalyst. *Renew. Energy* **2016**, *97*, 373–379. [[CrossRef](#)]
14. Coronado, C.J.R. Glycerol: Production, consumption, prices, characterization and new trends in combustion. *Renew. Sustain. Energy Rev.* **2013**, *27*, 475–493. [[CrossRef](#)]
15. Liu, Z.; Peng, W.; Motahari-Nezhad, M.; Shahraki, S.; Beheshti, M. Circulating fluidized bed gasification of biomass for flexible end-use of syngas: A micro and nano scale study for production of bio-methanol. *J. Clean. Prod.* **2016**, *129*, 249–255. [[CrossRef](#)]
16. Iaquaniello, G.; Centi, G.; Salladini, A.; Palo, E.; Perathoner, S.; Spadaccini, L. Waste-to-methanol: Process and economics assessment. *Bioresour. Technol.* **2017**, *243*, 611–619. [[CrossRef](#)]
17. Anitha, M.; Kamarudin, S.K.; Shamsul, N.S.; Kofli, N.T. Determination of bio-methanol as intermediate product of anaerobic co-digestion in animal and agriculture wastes. *Int. J. Hydrogen Energy* **2015**, *40*, 11791–11799. [[CrossRef](#)]
18. Bonfim-Rocha, L.; Gimenes, M.L.; Bernardo de Faria, S.H.; Silva, R.O.; Esteller, L.J. Multi-objective design of a new sustainable scenario for bio-methanol production in Brazil. *J. Clean. Prod.* **2018**, *187*, 1043–1056. [[CrossRef](#)]
19. Hartley, U.W.; Amornraksa, S.; Kim-Lohsoontorn, P.; Laosiripojana, N. Thermodynamic analysis and experimental study of hydrogen production from oxidative reforming of n-butanol. *Chem. Eng. J.* **2015**, *278*, 2–12. [[CrossRef](#)]
20. Palma, V.; Ruocco, C.; Meloni, E.; Ricca, A. Highly active and stable Pt-Ni/CeO₂-SiO₂ catalysts for ethanol reforming. *J. Clean. Prod.* **2017**, *166*, 263–272. [[CrossRef](#)]
21. Bepari, S.; Kuila, D. Steam reforming of methanol, ethanol and glycerol over nickel-based catalysts-A review. *Int. J. Hydrogen Energy* **2019**. [[CrossRef](#)]
22. Montero, C.; Remiro, A.; Valle, B.; Oar-Arteta, L.; Bilbao, J.; Gayubo, A.G. Origin and nature of coke in ethanol steam reforming and its role in deactivation of Ni/La₂O₃-αAl₂O₃ catalyst. *Ind. Eng. Chem. Res.* **2019**, *58*, 14736–14751. [[CrossRef](#)]
23. Palma, V.; Ruocco, C.; Meloni, E.; Ricca, A. Influence of Catalytic Formulation and Operative Conditions on Coke Deposition over CeO₂-SiO₂ Based Catalysts for Ethanol Reforming. *Energies* **2017**, *10*, 1030. [[CrossRef](#)]
24. Horng, R.-F.; Lai, M.-P.; Chiu, W.-C.; Huang, W.-C. Thermodynamic analysis of syngas production and carbon formation on oxidative steam reforming of butanol. *Int. J. Hydrogen Energy* **2016**, *41*, 889–896. [[CrossRef](#)]
25. Valle, B.; Aramburu, B.; Olazar, M.; Bilbao, J.; Gayubo, A.G. Steam reforming of raw bio-oil over Ni/La₂O₃-αAl₂O₃: Influence of temperature on product yields and catalyst deactivation. *Fuel* **2018**, *216*, 463–474. [[CrossRef](#)]

26. Coll, R.; Salvadó, J.; Farriol, X.; Montane, D. Steam reforming model compounds of biomass gasification tars: Conversion at different operating conditions and tendency towards coke formation. *Fuel Process. Technol.* **2001**, *74*, 19–31. [[CrossRef](#)]
27. Larmier, K.; Chizallet, C.; Cadran, N.; Maury, S.; Abboud, J.; Lamic-Humblot, A.-F.; Marceau, E.; Lauron-Pernot, H. Mechanistic investigation of isopropanol conversion on alumina catalysts: Location of active sites for alkene/ether production. *ACS Catal.* **2015**, *5*, 4423–4437. [[CrossRef](#)]
28. De Rezende, S.M.; Franchini, C.A.; Dieuzeide, M.L.; De Farias, A.M.D.; Amadeo, N.; Fraga, M. Glycerol steam reforming over layered double hydroxide-supported Pt catalysts. *Chem. Eng. J.* **2015**, *272*, 108–118. [[CrossRef](#)]
29. Ochoa, A.; Aramburu, B.; Valle, B.; Resasco, D.E.; Bilbao, J.; Gayubo, A.G.; Castaño, P. Role of oxygenates and effect of operating conditions in the deactivation of a Ni supported catalyst during the steam reforming of bio-oil. *Green Chem.* **2017**, *19*, 4315–4333. [[CrossRef](#)]
30. Sánchez, N.; Encinar, J.M.; Nogales, S.; González, J.F. Lanthanum Effect on Ni/Al₂O₃ as a Catalyst Applied in Steam Reforming of Glycerol for Hydrogen Production. *Processes* **2019**, *7*, 449. [[CrossRef](#)]
31. Harun, N.; Abidin, S.Z.; Osazuwa, O.; Taufiq-Yap, Y.H.; Azizan, M.T. Hydrogen production from glycerol dry reforming over Ag-promoted Ni/Al₂O₃. *Int. J. Hydrogen Energy* **2019**, *44*, 213–225. [[CrossRef](#)]
32. Gharahshiran, V.S.; Yousefpour, M.; Amini, V. A comparative study of zirconia and yttria promoted mesoporous carbon-nickel-cobalt catalysts in steam reforming of ethanol for hydrogen production. *Mol. Catal.* **2020**, *484*, 110767. [[CrossRef](#)]
33. Ramesh, S.; Yang, E.-H.; Jung, J.-S.; Moon, D.J. Copper decorated perovskite an efficient catalyst for low temperature hydrogen production by steam reforming of glycerol. *Int. J. Hydrogen Energy* **2015**, *40*, 11428–11435. [[CrossRef](#)]
34. Shao, J.; Zeng, G.; Li, Y. Effect of Zn substitution to a LaNiO_{3-δ} perovskite structured catalyst in ethanol steam reforming. *Int. J. Hydrogen Energy* **2017**, *42*, 17362–17375. [[CrossRef](#)]
35. Sun, C.; Zheng, Z.; Wang, S.; Li, X.; Wu, X.; An, X.; Xie, X. Yolk-shell structured Pt-CeO₂@Ni-SiO₂ as an efficient catalyst for enhanced hydrogen production from ethanol steam reforming. *Ceram. Int.* **2018**, *44*, 1438–1442. [[CrossRef](#)]
36. He, S.; Mei, Z.; Liu, N.; Zhang, L.; Lu, J.; Li, X.; Wang, J.; He, D.; Luo, Y. Ni/SBA-15 catalysts for hydrogen production by ethanol steam reforming: Effect of nickel precursor. *Int. J. Hydrogen Energy* **2017**, *42*, 14429–14438. [[CrossRef](#)]
37. Ruocco, C.; Palma, V.; Ricca, A. Hydrogen production by oxidative reforming of ethanol in a fluidized bed reactor using a Pt Ni/CeO₂SiO₂ catalyst. *Int. J. Hydrogen Energy* **2019**, *44*, 12661–12670. [[CrossRef](#)]
38. Wang, F.; Zhang, L.; Deng, J.; Zhang, J.; Han, B.; Wang, Y.; Li, Z.; Yu, H.; Cai, W.; Deng, Z. Embedded Ni catalysts in Ni-O-Ce solid solution for stable hydrogen production from ethanol steam reforming reaction. *Fuel Process. Technol.* **2019**, *193*, 94–101. [[CrossRef](#)]
39. Ricca, A.; Palma, V.; Martino, M.; Meloni, E. Innovative catalyst design for methane steam reforming intensification. *Fuel* **2017**, *198*, 175–182. [[CrossRef](#)]
40. Palma, V.; Ruocco, C.; Castaldo, F.; Ricca, A.; Boettge, D. Ethanol steam reforming over bimetallic coated ceramic foams: Effect of reactor configuration and catalytic support. *Int. J. Hydrogen Energy* **2015**, *40*, 12650–12662. [[CrossRef](#)]
41. Koc, S.; Avci, A.K. Reforming of glycerol to hydrogen over Ni-based catalysts in a microchannel reactor. *Fuel Process. Technol.* **2017**, *156*, 357–365. [[CrossRef](#)]
42. Montero, C.; Ochoa, A.; Castaño, P.; Bilbao, J.; Gayubo, A.G. Monitoring Ni 0 and coke evolution during the deactivation of a Ni/La₂O₃-αAl₂O₃ catalyst in ethanol steam reforming in a fluidized bed. *J. Catal.* **2015**, *331*, 181–192. [[CrossRef](#)]
43. Mondal, T.; Pant, K.K.; Dalai, A.K. Catalytic oxidative steam reforming of bio-ethanol for hydrogen production over Rh promoted Ni/CeO₂-ZrO₂ catalyst. *Int. J. Hydrogen Energy* **2015**, *40*, 2529–2544. [[CrossRef](#)]
44. Li, M.-R.; Wang, G.-C. The mechanism of ethanol steam reforming on the Co⁰ and Co²⁺ sites: A DFT study. *J. Catal.* **2018**, *365*, 391–404. [[CrossRef](#)]
45. Grewal, T.P.K.; Roy, S. Modeling the effect of coke deposition in a heat integrated ethanol reformer. *Int. J. Hydrogen Energy* **2016**, *41*, 19863–19880. [[CrossRef](#)]
46. Argyle, M.D.; Bartholomew, C.H. Heterogeneous catalyst deactivation and regeneration: A review. *Catalysts* **2015**, *5*, 145–269. [[CrossRef](#)]

47. Trevisanut, C.; Mari, M.; Millet, J.-M.M.; Cavani, F. Chemical-loop reforming of ethanol over metal ferrites: An analysis of structural features affecting reactivity. *Int. J. Hydrogen Energy* **2015**, *40*, 5264–5271. [[CrossRef](#)]
48. Sharma, Y.C.; Kumar, A.; Prasad, R.; Upadhyay, S.N. Ethanol steam reforming for hydrogen production: Latest and effective catalyst modification strategies to minimize carbonaceous deactivation. *Renew. Sustain. Energy Rev.* **2017**, *74*, 89–103. [[CrossRef](#)]
49. Li, D.; Li, X.; Gong, J. Catalytic reforming of oxygenates: State of the art and future prospects. *Chem. Rev.* **2016**, *116*, 11529–11653. [[CrossRef](#)] [[PubMed](#)]
50. Lazar, M.D.; Senila, L.; Dan, M.; Mihet, M. Chapter 10—Crude bioethanol reforming process: The advantage of a biosource exploitation. In *Ethanol*; Basile, A., Iulianelli, A., Dalena, F., Veziroğlu, T.N., Eds.; Elsevier: Amsterdam, The Netherlands, 2019; pp. 257–288.
51. Liu, Z.; Duchoň, T.; Wang, H.; Peterson, E.W.; Zhou, Y.; Luo, S.; Zhou, J.; Matolin, V.; Stacchiola, D.J.; Rodríguez, J.A.; et al. Mechanistic Insights of Ethanol Steam Reforming over Ni–CeO_x(111): The Importance of Hydroxyl Groups for Suppressing Coke Formation. *J. Phys. Chem. C* **2015**, *119*, 18248–18256. [[CrossRef](#)]
52. Gonçalves, A.A.S.; Faustino, P.B.; Assaf, J.M.; Jaroniec, M. One-Pot Synthesis of Mesoporous Ni–Ti–Al Ternary Oxides: Highly Active and Selective Catalysts for Steam Reforming of Ethanol. *ACS Appl. Mater. Interfaces* **2017**, *9*, 6079–6092. [[CrossRef](#)]
53. Osorio-Vargas, P.; Flores-González, N.A.; Navarro, R.M.; Fierro, J.L.; Campos, C.H.; Reyes, P. Improved stability of Ni/Al₂O₃ catalysts by effect of promoters (La₂O₃, CeO₂) for ethanol steam-reforming reaction. *Catal. Today* **2016**, *259*, 27–38. [[CrossRef](#)]
54. Jo, S.W.; Kwak, B.S.; Kim, K.M.; Do, J.Y.; Park, N.-K.; Lee, T.J.; Lee, S.-T.; Kang, M. Reasonable harmony of Ni and Mn in core@shell-structured NiMn@SiO₂ catalysts prepared for hydrogen production from ethanol steam reforming. *Chem. Eng. J.* **2016**, *288*, 858–868. [[CrossRef](#)]
55. Chen, M.; Wang, C.; Wang, Y.; Tang, Z.; Yang, Z.; Zhang, H.; Wang, J. Hydrogen production from ethanol steam reforming: Effect of Ce content on catalytic performance of Co/Sepiolite catalyst. *Fuel* **2019**, *247*, 344–355. [[CrossRef](#)]
56. Passos, A.R.; Martins, L.; Pulcinelli, S.H.; Santilli, C.; Briois, V. Correlation of Sol-Gel Alumina-Supported Cobalt Catalyst Processing to Cobalt Speciation, Ethanol Steam Reforming Activity, and Stability. *ChemCatChem* **2017**, *9*, 3918–3929. [[CrossRef](#)]
57. Spallina, V.; Maturro, G.; Ruocco, C.; Meloni, E.; Palma, V.; Fernandez, E.; Melendez, J.; Tanaka, A.P.; Sole, J.V.; Annaland, M.V.S.; et al. Direct route from ethanol to pure hydrogen through autothermal reforming in a membrane reactor: Experimental demonstration, reactor modelling and design. *Energy* **2018**, *143*, 666–681. [[CrossRef](#)]
58. Muñoz, M.; Moreno, S.; Molina, R. Oxidative steam reforming of ethanol (OSRE) over stable NiCo–MgAl catalysts by microwave or sonication assisted coprecipitation. *Int. J. Hydrogen Energy* **2017**, *42*, 12284–12294. [[CrossRef](#)]
59. Passos, A.R.; Pulcinelli, S.H.; Santilli, C.V.; Briois, V. Operando monitoring of metal sites and coke evolution during non-oxidative and oxidative ethanol steam reforming over Ni and NiCu ex-hydrotralcite catalysts. *Catal. Today* **2019**, *336*, 122–130. [[CrossRef](#)]
60. Palma, V.; Ruocco, C.; Meloni, E.; Ricca, A. Oxidative steam reforming of ethanol on mesoporous silica supported PtNi/CeO₂ catalysts. *Int. J. Hydrogen Energy* **2017**, *42*, 1598–1608. [[CrossRef](#)]
61. Palma, V.; Ruocco, C.; Meloni, E.; Ricca, A. Oxidative reforming of ethanol over CeO₂ -SiO₂ based catalysts in a fluidized bed reactor. *Chem. Eng. Process. Process. Intensif.* **2018**, *124*, 319–327. [[CrossRef](#)]
62. Yu, J.; Odriozola, J.; Reina, T.R. Dry reforming of ethanol and glycerol: Mini-review. *Catalysts* **2019**, *9*, 1015. [[CrossRef](#)]
63. Zhao, S.; Cai, W.; Li, Y.; Yu, H.; Zhang, S.; Cui, L. Syngas production from ethanol dry reforming over Rh/CeO₂ catalyst. *J. Saudi Chem. Soc.* **2018**, *22*, 58–65. [[CrossRef](#)]
64. Nozawa, T.; Yoshida, A.; Hikichi, S.; Naito, S. Effects of Re addition upon aqueous phase reforming of ethanol over TiO₂ supported Rh and Ir catalysts. *Int. J. Hydrogen Energy* **2015**, *40*, 4129–4140. [[CrossRef](#)]
65. Xiong, H.; DeLaRiva, A.; Datye, A.K.; Wang, Y. Low-temperature aqueous-phase reforming of ethanol on bimetallic PdZn catalysts. *Catal. Sci. Technol.* **2015**, *5*, 254–263. [[CrossRef](#)]
66. Zhao, Z.; Zhang, L.; Tan, Q.; Yang, F.; Faria, J.; Resasco, D.E. Synergistic bimetallic Ru–Pt catalysts for the low-temperature aqueous phase reforming of ethanol. *AIChE J.* **2018**, *65*, 151–160. [[CrossRef](#)]

67. Gogoi, P.; Nagpure, A.S.; Kandasamy, P.; Satyanarayana, C.V.V.; Raja, T.; Kandasamy, P.; Thirumalaiswamy, R. Insights into the catalytic activity of Ru/NaY catalysts for efficient H₂ production through aqueous phase reforming. *Sustain. Energy Fuels* **2020**, *4*, 678–690. [[CrossRef](#)]
68. Mulewa, W.; Tahir, M.; Amin, N.A.S. MMT-supported Ni/TiO₂ nanocomposite for low temperature ethanol steam reforming toward hydrogen production. *Chem. Eng. J.* **2017**, *326*, 956–969. [[CrossRef](#)]
69. Nejat, T.; Jalalinezhad, P.; Hormozi, F.; Bahrami, Z. Hydrogen production from steam reforming of ethanol over Ni-Co bimetallic catalysts and MCM-41 as support. *J. Taiwan Inst. Chem. Eng.* **2019**, *97*, 216–226. [[CrossRef](#)]
70. Di Michele, A.; Dell'Angelo, A.; Tripodi, A.; Bahadori, E.; Sánchez, F.; Motta, D.; Dimitratos, N.; Rossetti, I.; Ramis, G.; Sanchez, F. Steam reforming of ethanol over Ni/MgAl₂O₄ catalysts. *Int. J. Hydrogen Energy* **2019**, *44*, 952–964. [[CrossRef](#)]
71. Carvalho, F.L.; Asencios, Y.J.O.; Bellido, J.D.; Assaf, J.M. Bio-ethanol steam reforming for hydrogen production over Co₃O₄/CeO₂ catalysts synthesized by one-step polymerization method. *Fuel Process. Technol.* **2016**, *142*, 182–191. [[CrossRef](#)]
72. Konsolakis, M.; Ioakimidis, Z.; Kraia, T.; Marnellos, G.E. Hydrogen Production by Ethanol Steam Reforming (ESR) over CeO₂ Supported Transition Metal (Fe, Co, Ni, Cu) Catalysts: Insight into the Structure-Activity Relationship. *Catalysts* **2016**, *6*, 39. [[CrossRef](#)]
73. Greluk, M.; Słowik, G.; Rotko, M.; Machocki, A. Steam reforming and oxidative steam reforming of ethanol over PtKCo/CeO₂ catalyst. *Fuel* **2016**, *183*, 518–530. [[CrossRef](#)]
74. Riani, P.; Garbarino, G.; Canepa, F.; Busca, G. Cobalt nanoparticles mechanically deposited on α-Al₂O₃: A competitive catalyst for the production of hydrogen through ethanol steam reforming. *J. Chem. Technol. Biotechnol.* **2019**, *94*, 538–546. [[CrossRef](#)]
75. Mhadmhan, S.; Natewong, P.; Prasongthum, N.; Samart, C.; Reubroycharoen, P. Investigation of Ni/SiO₂ fiber catalysts prepared by different methods on hydrogen production from ethanol steam reforming. *Catalysts* **2018**, *8*, 319. [[CrossRef](#)]
76. Rodrigues, T.S.; De Moura, A.B.; Silva, F.; Candido, E.G.; Da Silva, A.G.; De Oliveira, D.C.; Quiroz, J.; Camargo, P.H.; Bergamaschi, V.S.; Ferreira, J.C.; et al. Ni supported Ce_{0.9}Sm_{0.1}O_{2-δ} nanowires: An efficient catalyst for ethanol steam reforming for hydrogen production. *Fuel* **2019**, *237*, 1244–1253. [[CrossRef](#)]
77. Roy, B.; Leclerc, C. Study of preparation method and oxidization/reduction effect on the performance of nickel-cerium oxide catalysts for aqueous-phase reforming of ethanol. *J. Power Sources* **2015**, *299*, 114–124. [[CrossRef](#)]
78. Sohn, H.; Ozkan, U.S. Cobalt-Based Catalysts for Ethanol Steam Reforming: An Overview. *Energy Fuels* **2016**, *30*, 5309–5322. [[CrossRef](#)]
79. Yoshida, H.; Yamaoka, R.; Arai, M. Stable Hydrogen Production from Ethanol through Steam Reforming Reaction over Nickel-Containing Smectite-Derived Catalyst. *Int. J. Mol. Sci.* **2014**, *16*, 350–362. [[CrossRef](#)]
80. Ogo, S.; Sekine, Y. Recent progress in ethanol steam reforming using non-noble transition metal catalysts: A review. *Fuel Process. Technol.* **2020**, *199*, 106238. [[CrossRef](#)]
81. Hou, T.; Yu, B.; Zhang, S.; Xu, T.; Wang, D.; Cai, W. Hydrogen production from ethanol steam reforming over Rh/CeO₂ catalyst. *Catal. Commun.* **2015**, *58*, 137–140. [[CrossRef](#)]
82. Hou, T.; Lei, Y.; Zhang, S.; Zhang, J.; Cai, W. Ethanol dry reforming for syngas production over Ir/CeO₂ catalyst. *J. Rare Earths* **2015**, *33*, 42–45. [[CrossRef](#)]
83. Moraes, T.S.; Neto, R.C.R.; Ribeiro, M.; Mattos, L.V.; Kourtelesis, M.; Ladas, S.; Verykios, X.; Noronha, F.B. The study of the performance of PtNi/CeO₂-nanocube catalysts for low temperature steam reforming of ethanol. *Catal. Today* **2015**, *242*, 35–49. [[CrossRef](#)]
84. Moraes, T.S.; Neto, R.C.R.; Ribeiro, M.; Mattos, L.V.; Kourtelesis, M.; Ladas, S.; Verykios, X.; Noronha, F.B. Ethanol conversion at low temperature over CeO₂-Supported Ni-based catalysts. Effect of Pt addition to Ni catalyst. *Appl. Catal. B Environ.* **2016**, *181*, 754–768. [[CrossRef](#)]
85. Cifuentes, B.; Valero, M.F.; Conesa, J.A.; Cobo, M. Hydrogen Production by Steam Reforming of Ethanol on Rh-Pt Catalysts: Influence of CeO₂, ZrO₂, and La₂O₃ as Supports. *Catalysts* **2015**, *5*, 1872–1896. [[CrossRef](#)]
86. Palma, V.; Ruocco, C.; Meloni, E.; Ricca, A. Renewable hydrogen from ethanol reforming over CeO₂-SiO₂ based catalysts. *Catalysts* **2017**, *7*, 226. [[CrossRef](#)]

87. Campos, C.H.; Pecchi, G.; Fierro, J.L.G.; Osorio-Vargas, P. Enhanced bimetallic Rh-Ni supported catalysts on alumina doped with mixed lanthanum-cerium oxides for ethanol steam reforming. *Mol. Catal.* **2019**, *469*, 87–97. [[CrossRef](#)]
88. Sanchez, N.; Ruiz, R.; Cifuentes, B.; Cobo, M. Hydrogen from glucose: A combined study of glucose fermentation, bioethanol purification, and catalytic steam reforming. *Int. J. Hydrogen Energy* **2016**, *41*, 5640–5651. [[CrossRef](#)]
89. Bilal, M.; Jackson, S.D. Ethanol steam reforming over Pt/Al₂O₃ and Rh/Al₂O₃ catalysts: The effect of impurities on selectivity and catalyst deactivation. *Appl. Catal. A Gen.* **2017**, *529*, 98–107. [[CrossRef](#)]
90. Iulianelli, A.; Palma, V.; Bagnato, G.; Ruocco, C.; Huang, Y.; Veziroglu, N.T.; Basile, A. From bioethanol exploitation to high grade hydrogen generation: Steam reforming promoted by a Co-Pt catalyst in a Pd-based membrane reactor. *Renew. Energy* **2018**, *119*, 834–843. [[CrossRef](#)]
91. Nichele, V.; Signoretto, M.; Pinna, F.; Ghedini, E.; Compagnoni, M.; Rossetti, I.; Cruciani, G.; Di Michele, A. Bimetallic Ni-Cu catalysts for the low-temperature ethanol steam reforming: Importance of metal-support interactions. *Catal. Lett.* **2014**, *145*, 549–558. [[CrossRef](#)]
92. Rodriguez-Gomez, A.; Caballero, A. Bimetallic Ni-Co/SBA-15 catalysts for reforming of ethanol: How cobalt modifies the nickel metal phase and product distribution. *Mol. Catal.* **2018**, *449*, 122–130. [[CrossRef](#)]
93. Chen, L.-C.; Cheng, H.; Chiang, C.-W.; Lin, S.D. Sustainable hydrogen production by ethanol steam reforming using a partially reduced copper-nickel oxide catalyst. *ChemSusChem* **2015**, *8*, 1787–1793. [[CrossRef](#)]
94. Braga, A.H.; Ribeiro, M.; Noronha, F.B.; Galante, D.; Bueno, J.M.C.; Santos, J.B.O. Effects of Co addition to supported Ni catalysts on hydrogen production from oxidative steam reforming of ethanol. *Energy Fuels* **2018**, *32*, 12814–12825. [[CrossRef](#)]
95. Baruah, R.; Dixit, M.; Parejiya, A.; Basarkar, P.; Bhargav, A.; Sharma, S. Oxidative steam reforming of ethanol on rhodium catalyst—I: Spatially resolved steady-state experiments and microkinetic modeling. *Int. J. Hydrogen Energy* **2017**, *42*, 10184–10198. [[CrossRef](#)]
96. Weng, S.-F.; Hsieh, H.-C.; Lee, C.-S. Hydrogen production from oxidative steam reforming of ethanol on nickel-substituted pyrochlore phase catalysts. *Int. J. Hydrogen Energy* **2017**, *42*, 2849–2860. [[CrossRef](#)]
97. Hsieh, H.-C.; Chang, Y.-C.; Tsai, P.-W.; Lin, Y.-Y.; Chuang, Y.-C.; Sheu, H.-S.; Lee, C.-S. Metal substituted pyrochlore phase Li_xLa_{2-x}Ce_{1.8}Ru_{0.2}O_{7-δ} (x = 0.0–0.6) as an effective catalyst for oxidative and auto-thermal steam reforming of ethanol. *Catal. Sci. Technol.* **2019**, *9*, 1406–1419. [[CrossRef](#)]
98. Cao, D.; Zeng, F.; Zhao, Z.; Cai, W.; Li, Y.; Yu, H.; Zhang, S.; Qu, F. Cu based catalysts for syngas production from ethanol dry reforming: Effect of oxide supports. *Fuel* **2018**, *219*, 406–416. [[CrossRef](#)]
99. Cao, N.; Cai, W.; Li, Y.; Li, C.; Yu, H.; Zhang, S.; Qu, F. Syngas Production from Ethanol Dry Reforming over Cu/Ce_{0.8}Zr_{0.2}O₂ Catalyst. *Catal. Lett.* **2017**, *147*, 2929–2939. [[CrossRef](#)]
100. Chen, Q.; Cai, W.; Liu, Y.; Zhang, S.; Li, Y.; Huang, D.; Wang, T.; Li, Y. Synthesis of Cu-Ce_{0.8}Zr_{0.2}O₂ catalyst by ball milling for CO₂ reforming of ethanol. *J. Saudi Chem. Soc.* **2019**, *23*, 111–117. [[CrossRef](#)]
101. Dang, C.; Wu, S.; Yang, G.; Cao, Y.; Wang, H.; Peng, F.; Yu, H. Syngas production by dry reforming of the mixture of glycerol and ethanol with CaCO₃. *J. Energy Chem.* **2020**, *43*, 90–97. [[CrossRef](#)]
102. Da Costa-Serra, J.F.; Chica, A. Catalysts based on Co-Birnessite and Co-Todorokite for the efficient production of hydrogen by ethanol steam reforming. *Int. J. Hydrogen Energy* **2018**, *43*, 16859–16865. [[CrossRef](#)]
103. Wei, Y.; Cai, W.; Deng, S.; Li, Z.; Yu, H.; Zhang, S.; Yu, Z.; Cui, L.; Qu, F. Efficient syngas production via dry reforming of renewable ethanol over Ni/KIT-6 nanocatalysts. *Renew. Energy* **2020**, *145*, 1507–1516. [[CrossRef](#)]
104. Chai, R.; Li, Y.; Zhang, Q.; Zhao, G.; Liu, Y.; Lu, Y. Monolithic Ni-MO_x/Ni-foam (M = Al, Zr or Y) catalysts with enhanced heat/mass transfer for energy-efficient catalytic oxy-methane reforming. *Catal. Commun.* **2015**, *70*, 1–5. [[CrossRef](#)]
105. Moraes, T.S.; Borges, L.E.P.; Farrauto, R.; Noronha, F.B. Steam reforming of ethanol on Rh/SiCeO₂ washcoated monolith catalyst: Stable catalyst performance. *Int. J. Hydrogen Energy* **2018**, *43*, 115–126. [[CrossRef](#)]
106. Gaudillere, C.; González, J.J.; Chica, A.; Serra, J.M. YSZ monoliths promoted with Co as catalysts for the production of H₂ by steam reforming of ethanol. *Appl. Catal. A Gen.* **2017**, *538*, 165–173. [[CrossRef](#)]
107. Palma, V.; Ruocco, C.; Ricca, A. Ceramic foams coated with PtNi/CeO₂ZrO₂ for bioethanol steam reforming. *Int. J. Hydrogen Energy* **2016**, *41*, 11526–11536. [[CrossRef](#)]
108. Turczyniak, S.; Greluk, M.; Słowik, G.; Gac, W.; Zafeiratos, S.; Machocki, A. Surface state and catalytic performance of ceria-supported cobalt catalysts in the steam reforming of ethanol. *ChemCatChem* **2017**, *9*, 782–797. [[CrossRef](#)]

109. Greluk, M.; Rybak, P.; Słowik, G.; Rotko, M.; Machocki, A. Comparative study on steam and oxidative steam reforming of ethanol over 2KCo/ZrO₂ catalyst. *Catal. Today* **2015**, *242*, 50–59. [[CrossRef](#)]
110. Greluk, M.; Rotko, M.; Turczyniak-Surdacka, S. Enhanced catalytic performance of La₂O₃ promoted Co/CeO₂ and Ni/CeO₂ catalysts for effective hydrogen production by ethanol steam reforming. *Renew. Energy* **2020**, *155*, 378–395. [[CrossRef](#)]
111. Cerdá-Moreno, C.; Da Costa-Serra, J.F.; Chica, A. Co and La supported on Zn-Hydrotalcite-derived material as efficient catalyst for ethanol steam reforming. *Int. J. Hydrogen Energy* **2019**, *44*, 12685–12692. [[CrossRef](#)]
112. Kim, D.; Kwak, B.S.; Park, N.-K.; Han, G.B.; Kang, M. Dynamic hydrogen production from ethanol steam-reforming reaction on Ni_xMo_y/SBA-15 catalytic system. *Int. J. Energy Res.* **2015**, *39*, 279–292. [[CrossRef](#)]
113. Kwak, B.S.; Lee, G.; Park, S.-M.; Kang, M. Effect of MnO_x in the catalytic stabilization of Co₂MnO₄ spinel during the ethanol steam reforming reaction. *Appl. Catal. A Gen.* **2015**, *503*, 165–175. [[CrossRef](#)]
114. Liu, Z.; Xu, W.; Yao, S.; Johnson-Peck, A.C.; Zhao, F.; Michorczyk, P.; Kubacka, A.; Stach, E.A.; Fernández-García, M.; Senanayake, S.D.; et al. Superior performance of Ni–W–Ce mixed-metal oxide catalysts for ethanol steam reforming: Synergistic effects of W- and Ni-dopants. *J. Catal.* **2015**, *321*, 90–99. [[CrossRef](#)]
115. Li, D.; Zeng, L.; Li, X.; Wang, X.; Ma, H.; Assabumrungrat, S.; Gong, J. Ceria-promoted Ni/SBA-15 catalysts for ethanol steam reforming with enhanced activity and resistance to deactivation. *Appl. Catal. B Environ.* **2015**, *176*, 532–541. [[CrossRef](#)]
116. Du, Y.-L.; Wu, X.; Cheng, Q.; Huang, Y.-L.; Huang, W. Development of Ni-Based Catalysts Derived from Hydrotalcite-Like Compounds Precursors for Synthesis Gas Production via Methane or Ethanol Reforming. *Catalysts* **2017**, *7*, 70. [[CrossRef](#)]
117. Marinho, A.L.A.; Rabelo-Neto, R.C.; Noronha, F.B.; Mattos, L.V. Steam reforming of ethanol over Ni-based catalysts obtained from LaNiO₃ and LaNiO₃/CeSiO₂ perovskite-type oxides for the production of hydrogen. *Appl. Catal. A Gen.* **2016**, *520*, 53–64. [[CrossRef](#)]
118. Dan, M.; Senila, L.; Roman, M.; Mihet, M.; Lazar, M.D. From wood wastes to hydrogen—Preparation and catalytic steam reforming of crude bio-ethanol obtained from fir wood. *Renew. Energy* **2015**, *74*, 27–36. [[CrossRef](#)]
119. He, S.; He, S.; Zhang, L.; Li, X.; Wang, J.; He, D.; Lu, J.; Luo, Y. Hydrogen production by ethanol steam reforming over Ni/SBA-15 mesoporous catalysts: Effect of Au addition. *Catal. Today* **2015**, *258*, 162–168. [[CrossRef](#)]
120. Mondal, T.; Pant, K.K.; Dalai, A.K. Oxidative and non-oxidative steam reforming of crude bio-ethanol for hydrogen production over Rh promoted Ni/CeO₂-ZrO₂ catalyst. *Appl. Catal. A Gen.* **2015**, *499*, 19–31. [[CrossRef](#)]
121. Bahari, M.B.; Phuc, N.H.H.; Abdullah, B.; Alenazey, F.; Vo, D.-V.N. Ethanol dry reforming for syngas production over Ce-promoted Ni/Al₂O₃ catalyst. *J. Environ. Chem. Eng.* **2016**, *4*, 4830–4838. [[CrossRef](#)]
122. Bahari, M.B.; Phuc, N.H.H.; Alenazey, F.; Vu, K.B.; Ainirazali, N.; Vo, D.-V.N. Catalytic performance of La-Ni/Al₂O₃ catalyst for CO₂ reforming of ethanol. *Catal. Today* **2017**, *291*, 67–75. [[CrossRef](#)]
123. Fayaz, F.; Danh, H.T.; Nguyen-Huy, C.; Vu, K.B.; Abdullah, B.; Vo, D.-V.N. Promotional Effect of Ce-dopant on Al₂O₃-supported Co Catalysts for Syngas Production via CO₂ Reforming of Ethanol. *Procedia Eng.* **2016**, *148*, 646–653. [[CrossRef](#)]
124. Fayaz, F.; Bach, L.-G.; Bahari, M.B.; Nguyen, D.T.; Vu, K.B.; Kanthasamy, R.; Samart, C.; Nguyen-Huy, C.; Vo, D.-V.N. Stability evaluation of ethanol dry reforming on Lanthania-doped cobalt-based catalysts for hydrogen-rich syngas generation. *Int. J. Energy Res.* **2018**, *43*, 405–416. [[CrossRef](#)]
125. Shafiqah, M.-N.N.; Nguyen, T.D.; Jun, L.N.; Bahari, M.B.; Phuong, P.T.; Abdullah, B.; Vo, D.-V.N. *Production of Syngas from Ethanol CO₂ Reforming on La-Doped Cu/Al₂O₃: Impact of Promoter Loading*; AIP Publishing LLC: Melville, NY, USA, 2019; p. 020011.
126. Słowik, G.; Greluk, M.; Rotko, M.; Machocki, A. Evolution of the structure of unpromoted and potassium-promoted ceria-supported nickel catalysts in the steam reforming of ethanol. *Appl. Catal. B Environ.* **2018**, *221*, 490–509. [[CrossRef](#)]
127. Cifuentes, B.; Hernández, M.; Monsalve, S.; Cobo, M. Hydrogen production by steam reforming of ethanol on a RhPt/CeO₂/SiO₂ catalyst: Synergistic effect of the Si:Ce ratio on the catalyst performance. *Appl. Catal. A Gen.* **2016**, *523*, 283–293. [[CrossRef](#)]

128. Wang, F.; Zhang, L.; Zhu, J.; Han, B.; Zhao, L.; Yu, H.; Deng, Z.; Shi, W. Study on different CeO₂ structure stability during ethanol steam reforming reaction over Ir/CeO₂ nanocatalysts. *Appl. Catal. A Gen.* **2018**, *564*, 226–233. [[CrossRef](#)]
129. Osorio-Vargas, P.; Campos, C.H.; Navarro, R.M.; Fierro, J.L.; Reyes, P. Rh/Al₂O₃–La₂O₃ catalysts promoted with CeO₂ for ethanol steam reforming reaction. *J. Mol. Catal. A Chem.* **2015**, *407*, 169–181. [[CrossRef](#)]
130. Gunduz, S.; Doğu, T. Hydrogen by steam reforming of ethanol over Co–Mg incorporated novel mesoporous alumina catalysts in tubular and microwave reactors. *Appl. Catal. B Environ.* **2015**, *168*, 497–508. [[CrossRef](#)]
131. Zhao, L.; Han, T.; Wang, H.; Zhang, L.; Liu, Y. Ni–Co alloy catalyst from LaNi_{1–x}Co_xO₃ perovskite supported on zirconia for steam reforming of ethanol. *Appl. Catal. B Environ.* **2016**, *187*, 19–29. [[CrossRef](#)]
132. Bepari, S.; Basu, S.; Pradhan, N.C.; Dalai, A.K. Steam reforming of ethanol over cerium-promoted Ni–Mg–Al hydrotalcite catalysts. *Catal. Today* **2017**, *291*, 47–57. [[CrossRef](#)]
133. Prasongthum, N.; Xiao, R.; Zhang, H.; Tsubaki, N.; Natewong, P.; Reubroycharoen, P. Highly active and stable Ni supported on CNTs–SiO₂ fiber catalysts for steam reforming of ethanol. *Fuel Process. Technol.* **2017**, *160*, 185–195. [[CrossRef](#)]
134. Dai, R.; Zheng, Z.; Sun, C.; Li, X.; Wang, S.; Wu, X.; An, X.; Xie, X. Pt nanoparticles encapsulated in a hollow zeolite microreactor as a highly active and stable catalyst for low-temperature ethanol steam reforming. *Fuel* **2018**, *214*, 88–97. [[CrossRef](#)]
135. Dobosz, J.; Małecka, M.; Zawadzki, M. Hydrogen generation via ethanol steam reforming over Co/HAp catalysts. *J. Energy Inst.* **2018**, *91*, 411–423. [[CrossRef](#)]
136. Chen, M.; Wang, Y.; Yang, Z.; Liang, T.; Liu, S.; Zhou, Z.; Li, X. Effect of Mg-modified mesoporous Ni/Attapulgite catalysts on catalytic performance and resistance to carbon deposition for ethanol steam reforming. *Fuel* **2018**, *220*, 32–46. [[CrossRef](#)]
137. Xiao, Z.; Li, Y.; Hou, F.; Wu, C.; Pan, L.; Zou, J.; Wang, L.; Zhang, X.; Liu, G.; Li, G. Engineering oxygen vacancies and nickel dispersion on CeO₂ by Pr doping for highly stable ethanol steam reforming. *Appl. Catal. B Environ.* **2019**, *258*, 117940. [[CrossRef](#)]
138. Lee, J.H.; Do, J.Y.; Park, N.-K.; Ryu, H.-J.; Seo, M.W.; Kang, M. Hydrogen production on Pd_{0.01}Zn_{0.29}Mg_{0.7}Al₂O₄ spinel catalyst by low temperature ethanol steam reforming reaction. *J. Energy Inst.* **2019**, *92*, 1064–1076. [[CrossRef](#)]
139. Yang, P.; Li, N.; Teng, J.; Wu, J.; Ma, H. Effect of template on catalytic performance of La_{0.7}Ce_{0.3}Ni_{0.7}Fe_{0.3}O₃ for ethanol steam reforming reaction. *J. Rare Earths* **2019**, *37*, 594–601. [[CrossRef](#)]
140. Dai, R.; Zheng, Z.; Yan, W.; Lian, C.; Wu, X.; An, X.; Xie, X. Dragon fruit-like Pt–Cu@mSiO₂ nanocomposite as an efficient catalyst for low-temperature ethanol steam reforming. *Chem. Eng. J.* **2020**, *379*, 122299. [[CrossRef](#)]
141. Zhurka, M.D.; Lemonidou, A.A.; Kechagiopoulos, P.N. Elucidation of metal and support effects during ethanol steam reforming over Ni and Rh based catalysts supported on (CeO₂)-ZrO₂-La₂O₃. *Catal. Today* **2020**. [[CrossRef](#)]
142. Morales, M.; Segarra, M. Steam reforming and oxidative steam reforming of ethanol over La_{0.6}Sr_{0.4}CoO₃–perovskite as catalyst precursor for hydrogen production. *Appl. Catal. A Gen.* **2015**, *502*, 305–311. [[CrossRef](#)]
143. Fang, W.; Pirez, C.; Paul, S.; Jiménez-Ruiz, M.; Jobic, H.; Dumeignil, F.; Jalowiecki-Duhamel, L. Advanced functionalized Mg₂AlNiXHZOY nano-oxyhydrides ex-hydrotalcites for hydrogen production from oxidative steam reforming of ethanol. *Int. J. Hydrogen Energy* **2016**, *41*, 15443–15452. [[CrossRef](#)]
144. Muñoz, M.; Moreno, S.; Molina, R. Promoter effect of Ce and Pr on the catalytic stability of the Ni–Co system for the oxidative steam reforming of ethanol. *Appl. Catal. A Gen.* **2016**, *526*, 84–94. [[CrossRef](#)]
145. Hsieh, H.-C.; Tsai, P.-W.; Chang, Y.-C.; Weng, S.-F.; Sheu, H.-S.; Chuang, Y.-C.; Lee, C.-S. Oxidative steam reforming of ethanol over M_xLa_{2–x}Ce_{1.8}Ru_{0.2}O_{7–δ} (M = Mg, Ca) catalysts: Effect of alkaline earth metal substitution and support on stability and activity. *RSC Adv.* **2019**, *9*, 39932–39944. [[CrossRef](#)]
146. Bej, B.; Bepari, S.; Pradhan, N.C.; Neogi, S. Production of hydrogen by dry reforming of ethanol over alumina supported nano-NiO/SiO₂ catalyst. *Catal. Today* **2017**, *291*, 58–66. [[CrossRef](#)]
147. Samsudeen, K.; Ahmed, A.F.; Yahya, M.; Ahmed, A.; Anis, F. Effect of Calcination Temperature on Hydrogen Production via Ethanol Dry Reforming Over Ni/Al₂O₃ Catalyst. *Int. J. Res. Sci.* **2018**, *4*, 5–9. [[CrossRef](#)]
148. Usman, M.; Daud, W.M.A.W. Recent advances in the methanol synthesis via methane reforming processes. *RSC Adv.* **2015**, *5*, 21945–21972. [[CrossRef](#)]

149. Kothandaraman, J.; Kar, S.; Goeppert, A.; Sen, R.; Prakash, G.K.S. Advances in Homogeneous Catalysis for Low Temperature Methanol Reforming in the Context of the Methanol Economy. *Top. Catal.* **2018**, *61*, 542–559. [[CrossRef](#)]
150. Lee, H.; Jung, I.; Roh, G.; Na, Y.; Kang, H. Comparative Analysis of On-Board Methane and Methanol Reforming Systems Combined with HT-PEM Fuel Cell and CO₂ Capture/Liquefaction System for Hydrogen Fueled Ship Application. *Energies* **2020**, *13*, 224. [[CrossRef](#)]
151. Araya, S.S.; Liso, V.; Cui, X.; Li, N.; Zhu, J.; Sahlin, S.L.; Jensen, S.; Nielsen, M.; Kær, S. A Review of The Methanol Economy: The Fuel Cell Route. *Energies* **2020**, *13*, 596. [[CrossRef](#)]
152. Iulianelli, A.; Ghasemzadeh, K.; Basile, A. Progress in Methanol Steam Reforming Modelling via Membrane Reactors Technology. *Membranes* **2018**, *8*, 65. [[CrossRef](#)]
153. Palma, V.; Ruocco, C.; Martino, M.; Meloni, E.; Ricca, A. Bimetallic supported catalysts for hydrocarbons and alcohols reforming reactions. In *Hydrogen Production, Separation and Purification for Energy*; Institution of Engineering and Technology: London, UK, 2017; pp. 39–70.
154. Xu, X.; Shuai, K.; Xu, B. Review on copper and palladium based catalysts for methanol steam reforming to produce hydrogen. *Catalysts* **2017**, *7*, 183. [[CrossRef](#)]
155. Iulianelli, A.; Ribeirinha, P.; Mendes, A.; Basile, A. Methanol steam reforming for hydrogen generation via conventional and membrane reactors: A review. *Renew. Sustain. Energy Rev.* **2014**, *29*, 355–368. [[CrossRef](#)]
156. Tonelli, F.; Gorriz, O.; Tarditi, A.M.; Cornaglia, L.; Arrúa, L.; Abello, M.C. Activity and stability of a CuO/CeO₂ catalyst for methanol steam reforming. *Int. J. Hydrogen Energy* **2015**, *40*, 13379–13387. [[CrossRef](#)]
157. Das, D.; Llorca, J.; Domínguez, M.; Colussi, S.; Trovarelli, A.; Gayen, A. Methanol steam reforming behavior of copper impregnated over CeO₂–ZrO₂ derived from a surfactant assisted coprecipitation route. *Int. J. Hydrogen Energy* **2015**, *40*, 10463–10479. [[CrossRef](#)]
158. Deshmane, V.G.; Abrokwah, R.Y.; Kuila, D. Synthesis of stable Cu-MCM-41 nanocatalysts for H₂ production with high selectivity via steam reforming of methanol. *Int. J. Hydrogen Energy* **2015**, *40*, 10439–10452. [[CrossRef](#)]
159. Xu, T.; Zou, J.; Tao, W.; Zhang, S.; Cui, L.; Zeng, F.; Wang, D.; Cai, W. Co-nanocasting synthesis of Cu based composite oxide and its promoted catalytic activity for methanol steam reforming. *Fuel* **2016**, *183*, 238–244. [[CrossRef](#)]
160. Thattarathody, R.; Sheintuch, M. Kinetics and dynamics of methanol steam reforming on CuO/ZnO/alumina catalyst. *Appl. Catal. A Gen.* **2017**, *540*, 47–56. [[CrossRef](#)]
161. Bagherzadeh, S.B.; Haghighi, M. Plasma-enhanced comparative hydrothermal and coprecipitation preparation of CuO/ZnO/Al₂O₃ nanocatalyst used in hydrogen production via methanol steam reforming. *Energy Convers. Manag.* **2017**, *142*, 452–465. [[CrossRef](#)]
162. Ajamein, H.; Haghighi, M.; Alaei, S. The role of various fuels on microwave-enhanced combustion synthesis of CuO/ZnO/Al₂O₃ nanocatalyst used in hydrogen production via methanol steam reforming. *Energy Convers. Manag.* **2017**, *137*, 61–73. [[CrossRef](#)]
163. Abrokwah, R.Y.; Deshmane, V.G.; Kuila, D. Comparative performance of M-MCM-41 (M: Cu, Co, Ni, Pd, Zn and Sn) catalysts for steam reforming of methanol. *J. Mol. Catal. A Chem.* **2016**, *425*, 10–20. [[CrossRef](#)]
164. Papadopoulou, E.; Ioannides, T. Methanol Reforming over Cobalt Catalysts Prepared from Fumarate Precursors: TPD Investigation. *Catalysts* **2016**, *6*, 33. [[CrossRef](#)]
165. Li, J.; Mei, X.; Zhang, L.; Yu, Z.; Liu, Q.; Wei, T.; Wu, W.; Dong, D.; Xu, L.; Hu, X. A comparative study of catalytic behaviors of Mn, Fe, Co, Ni, Cu and Zn–Based catalysts in steam reforming of methanol, acetic acid and acetone. *Int. J. Hydrogen Energy* **2020**, *45*, 3815–3832. [[CrossRef](#)]
166. Maiti, S.; Llorca, J.; Domínguez, M.; Colussi, S.; Trovarelli, A.; Priolkar, K.R.; Aquilanti, G.; Gayen, A. Combustion synthesized copper-ion substituted FeAl₂O₄ (Cu_{0.1}Fe_{0.9}Al₂O₄): A superior catalyst for methanol steam reforming compared to its impregnated analogue. *J. Power Sources* **2016**, *304*, 319–331. [[CrossRef](#)]
167. Qing, S.-J.; Hou, X.-N.; Liu, Y.-J.; Wang, L.; Li, L.-D.; Gao, Z.-X. Catalytic performance of Cu-Ni-Al spinel for methanol steam reforming to hydrogen. *J. Fuel Chem. Technol.* **2018**, *46*, 1210–1217. [[CrossRef](#)]
168. Luo, X.; Hong, Y.; Wang, F.; Hao, S.; Pang, C.H.; Lester, E.H.; Wu, T. Development of nano Ni_xMg_yO solid solutions with outstanding anti-carbon deposition capability for the steam reforming of methanol. *Appl. Catal. B Environ.* **2016**, *194*, 84–97. [[CrossRef](#)]

169. Zeng, Z.; Liu, G.; Geng, J.; Jing, D.; Hong, X.; Guo, L. A high-performance PdZn alloy catalyst obtained from metal-organic framework for methanol steam reforming hydrogen production. *Int. J. Hydrogen Energy* **2019**, *44*, 24387–24397. [[CrossRef](#)]
170. Claudio-Piedras, A.; Ramírez-Zamora, R.M.; Alcántar-Vázquez, B.C.; Gutiérrez-Martínez, A.; Mondragón-Galicia, G.; Morales-Anzures, F.; Pérez-Hernández, R.; Modragón-Galicia, G. One dimensional Pt/CeO₂-NR catalysts for hydrogen production by steam reforming of methanol: Effect of Pt precursor. *Catal. Today* **2019**. [[CrossRef](#)]
171. Barrios, C.; Bosco, M.V.; Baltanás, M.A.; Bonivardi, A.L. Hydrogen production by methanol steam reforming: Catalytic performance of supported-Pd on zinc–cerium oxides' nanocomposites. *Appl. Catal. B Environ.* **2015**, *179*, 262–275. [[CrossRef](#)]
172. Ajamein, H.; Haghighi, M.; Shokrani, R.; Abdollahifar, M. On the solution combustion synthesis of copper based nanocatalysts for steam methanol reforming: Effect of precursor, ultrasound irradiation and urea/nitrate ratio. *J. Mol. Catal. A Chem.* **2016**, *421*, 222–234. [[CrossRef](#)]
173. Lin, L.; Zhou, W.; Gao, R.; Yao, S.; Zhang, X.; Xu, W.; Zheng, S.; Jiang, Z.; Yu, Q.; Li, Y.-W.; et al. Low-temperature hydrogen production from water and methanol using Pt/ α -MoC catalysts. *Nature* **2017**, *544*, 80–83. [[CrossRef](#)]
174. Cai, F.; Ibrahim, J.J.; Fu, Y.; Kong, W.; Zhang, J.; Sun, Y. Low-temperature hydrogen production from methanol steam reforming on Zn-modified Pt/MoC catalysts. *Appl. Catal. B Environ.* **2020**, *264*, 118500. [[CrossRef](#)]
175. Liu, X.; Men, Y.; Wang, J.; He, R.; Wang, Y. Remarkable support effect on the reactivity of Pt/In₂O₃/MO_x catalysts for methanol steam reforming. *J. Power Sources* **2017**, *364*, 341–350. [[CrossRef](#)]
176. Diaz-Perez, M.A.; Moya, J.; Serrano-Ruiz, J.C.; Faria, J. Interplay of support chemistry and reaction conditions on copper catalyzed methanol steam reforming. *Ind. Eng. Chem. Res.* **2018**, *57*, 15268–15279. [[CrossRef](#)] [[PubMed](#)]
177. Tahay, P.; Khani, Y.; Jabari, M.; Bahadoran, F.; Safari, N.; Zamanian, A. Synthesis of cubic and hexagonal ZnTiO₃ as catalyst support in steam reforming of methanol: Study of physical and chemical properties of copper catalysts on the H₂ and CO selectivity and coke formation. *Int. J. Hydrogen Energy* **2020**, *45*, 9484–9495. [[CrossRef](#)]
178. Talkhoncheh, S.K.; Minaei, S.; Ajamein, H.; Haghighi, M.; Abdollahifar, M. Synthesis of CuO/ZnO/Al₂O₃/ZrO₂/CeO₂ nanocatalysts via homogeneous precipitation and combustion methods used in methanol steam reforming for fuel cell grade hydrogen production. *RSC Adv.* **2016**, *6*, 57199–57209. [[CrossRef](#)]
179. Taghizadeh, M.; Akhoundzadeh, H.; Rezayan, A.; Sadeghian, M. Excellent catalytic performance of 3D-mesoporous KIT-6 supported Cu and Ce nanoparticles in methanol steam reforming. *Int. J. Hydrogen Energy* **2018**, *43*, 10926–10937. [[CrossRef](#)]
180. Phongboonchoo, Y.; Thouchprasitchai, N.; Pongstabodee, S. Hydrogen production with a low carbon monoxide content via methanol steam reforming over Cu_xCe_yMg_z/Al₂O₃ catalysts: Optimization and stability. *Int. J. Hydrogen Energy* **2017**, *42*, 12220–12235. [[CrossRef](#)]
181. Hou, X.; Qing, S.; Liu, Y.; Li, L.; Gao, Z.; Qin, Y. Enhancing effect of MgO modification of Cu–Al spinel oxide catalyst for methanol steam reforming. *Int. J. Hydrogen Energy* **2020**, *45*, 477–489. [[CrossRef](#)]
182. Liu, X.; Toyir, J.; De La Piscina, P.R.; Homs, N. Hydrogen production from methanol steam reforming over Al₂O₃- and ZrO₂- modified CuOZnOGa₂O₃ catalysts. *Int. J. Hydrogen Energy* **2017**, *42*, 13704–13711. [[CrossRef](#)]
183. Mohtashami, Y.; Taghizadeh, M. Performance of the ZrO₂ promoted Cu ZnO catalyst supported on acetic acid-treated MCM-41 in methanol steam reforming. *Int. J. Hydrogen Energy* **2019**, *44*, 5725–5738. [[CrossRef](#)]
184. Lu, J.; Li, X.; He, S.; Han, C.; Wan, G.; Lei, Y.; Chen, R.; Liu, P.; Chen, K.; Zhang, L.; et al. Hydrogen production via methanol steam reforming over Ni-based catalysts: Influences of Lanthanum (La) addition and supports. *Int. J. Hydrogen Energy* **2017**, *42*, 3647–3657. [[CrossRef](#)]
185. Azenha, C.; Mateos-Pedrero, C.; Queirós, S.; Concepción, P.; Mendes, A. Innovative ZrO₂-supported CuPd catalysts for the selective production of hydrogen from methanol steam reforming. *Appl. Catal. B Environ.* **2017**, *203*, 400–407. [[CrossRef](#)]
186. Liu, D.; Men, Y.; Wang, J.; Kolb, G.; Liu, X.; Wang, Y.; Sun, Q. Highly active and durable Pt/In₂O₃/Al₂O₃ catalysts in methanol steam reforming. *Int. J. Hydrogen Energy* **2016**, *41*, 21990–21999. [[CrossRef](#)]
187. Martinelli, M.; Jacobs, G.; Graham, U.; Crocker, M. Methanol Steam Reforming: Na Doping of Pt/YSZ Provides Fine Tuning of Selectivity. *Catalysts* **2017**, *7*, 148. [[CrossRef](#)]

188. Zhang, R.; Huang, C.; Zong, L.; Lu, K.; Wang, X.; Cai, J. Hydrogen Production from Methanol Steam Reforming over TiO₂ and CeO₂ Pillared Clay Supported Au Catalysts. *Appl. Sci.* **2018**, *8*, 176. [[CrossRef](#)]
189. Lytkina, A.A.; Orekhova, N.V.; Ermilova, M.; Yaroslavtsev, A.B. The influence of the support composition and structure (M_xZr_{1-x}O_{2-δ}) of bimetallic catalysts on the activity in methanol steam reforming. *Int. J. Hydrogen Energy* **2018**, *43*, 198–207. [[CrossRef](#)]
190. Lu, P.-J.; Cai, F.-F.; Zhang, J.; Liu, Y.; Sun, Y.-H. Hydrogen production from methanol steam reforming over B-modified CuZnAlO catalysts. *J. Fuel Chem. Technol.* **2019**, *47*, 791–798. [[CrossRef](#)]
191. Maiti, S.; Das, D.; Pal, K.; Llorca, J.; Soler, L.; Colussi, S.; Trovarelli, A.; Priolkar, K.R.; Sarode, P.; Asakura, K.; et al. Methanol steam reforming behavior of sol-gel synthesized nanodimensional Cu_xFe_{1-x}Al₂O₄ hercynites. *Appl. Catal. A Gen.* **2019**, *570*, 73–83. [[CrossRef](#)]
192. Song, Q.; Men, Y.; Wang, J.; Liu, S.; Chai, S.; An, W.; Wang, K.; Li, Y.; Tang, Y. Methanol steam reforming for hydrogen production over ternary composite ZnyCe1Zr9Ox catalysts. *Int. J. Hydrogen Energy* **2020**, *45*, 9592–9602. [[CrossRef](#)]
193. Mateos-Pedrero, C.; Silva, H.; Tanaka, D.P.; Liguori, S.; Iulianelli, A.; Basile, A.; Mendes, A. CuO/ZnO catalysts for methanol steam reforming: The role of the support polarity ratio and surface area. *Appl. Catal. B Environ.* **2015**, *174*, 67–76. [[CrossRef](#)]
194. Kim, S.; Yun, S.-W.; Lee, B.; Heo, J.; Kim, K.; Kim, Y.-T.; Lim, H. Steam reforming of methanol for ultra-pure H₂ production in a membrane reactor: Techno-economic analysis. *Int. J. Hydrogen Energy* **2019**, *44*, 2330–2339. [[CrossRef](#)]
195. Köpfle, N.; Mayr, L.; Schmidmair, D.; Bernardi, J.; Knop-Gericke, A.; Hävecker, M.; Klötzer, B.; Penner, S. A Comparative Discussion of the Catalytic Activity and CO₂-Selectivity of Cu-Zr and Pd-Zr (Intermetallic) Compounds in Methanol Steam Reforming. *Catalysts* **2017**, *7*, 53. [[CrossRef](#)]
196. Zhou, W.; Ke, Y.; Pei, P.; Yu, W.; Chu, X.; Li, S.; Yang, K. Hydrogen production from cylindrical methanol steam reforming microreactor with porous Cu-Al fiber sintered felt. *Int. J. Hydrogen Energy* **2018**, *43*, 3643–3654. [[CrossRef](#)]
197. Ke, Y.; Zhou, W.; Chu, X.; Yuan, D.; Wan, S.; Yu, W.; Liu, Y. Porous copper fiber sintered felts with surface microchannels for methanol steam reforming microreactor for hydrogen production. *Int. J. Hydrogen Energy* **2019**, *44*, 5755–5765. [[CrossRef](#)]
198. Tajrishi, O.Z.; Taghizadeh, M.; Kiadehi, A.D. Methanol steam reforming in a microchannel reactor by Zn-, Ce- and Zr- modified mesoporous Cu/SBA-15 nanocatalyst. *Int. J. Hydrogen Energy* **2018**, *43*, 14103–14120. [[CrossRef](#)]
199. Liu, Y.; Zhou, W.; Lin, Y.; Chen, L.; Chu, X.; Zheng, T.; Wan, S.; Lin, J. Novel copper foam with ordered hole arrays as catalyst support for methanol steam reforming microreactor. *Appl. Energy* **2019**, *246*, 24–37. [[CrossRef](#)]
200. Sarafraz, M.; Safaei, M.R.; Goodarzi, M.; Arjomandi, M. Reforming of methanol with steam in a micro-reactor with Cu-SiO₂ porous catalyst. *Int. J. Hydrogen Energy* **2019**, *44*, 19628–19639. [[CrossRef](#)]
201. Shanmugam, V.; Neuberg, S.; Zapf, R.; Pennemann, H.; Kolb, G. Hydrogen production over highly active Pt based catalyst coatings by steam reforming of methanol: Effect of support and co-support. *Int. J. Hydrogen Energy* **2020**, *45*, 1658–1670. [[CrossRef](#)]
202. Zhuang, X.; Xia, X.; Xu, X.; Li, L. Experimental investigation on hydrogen production by methanol steam reforming in a novel multichannel micro packed bed reformer. *Int. J. Hydrogen Energy* **2020**, *45*, 11024–11034. [[CrossRef](#)]
203. Zhu, J.; Araya, S.S.; Cui, X.; Sahlin, S.L.; Kær, S.K. Modeling and design of a multi-tubular packed-bed reactor for methanol steam reforming over a Cu/ZnO/Al₂O₃ catalyst. *Energies* **2020**, *13*, 610. [[CrossRef](#)]
204. Ke, C.; Lin, Z. Density functional theory based micro-and macro-kinetic studies of Ni-catalyzed methanol steam reforming. *Catalysts* **2020**, *10*, 349. [[CrossRef](#)]
205. Wang, G.; Wang, F.; Chen, B. Performance study on methanol steam reforming rib micro-reactor with waste heat recovery. *Energies* **2020**, *13*, 1564. [[CrossRef](#)]
206. Udani, P.P.C.; Gunawardana, P.V.D.S.; Lee, H.C.; Kim, D.H. Steam reforming and oxidative steam reforming of methanol over CuO-CeO₂ catalysts. *Int. J. Hydrogen Energy* **2009**, *34*, 7648–7655. [[CrossRef](#)]
207. Kim, J.H.; Jang, Y.S.; Kim, D.H. Multiple steady states in the oxidative steam reforming of methanol. *Chem. Eng. J.* **2018**, *338*, 752–763. [[CrossRef](#)]

208. Turco, M.; Bagnasco, G.; Costantino, U.; Marmottini, F.; Montanari, T.; Ramis, G.; Busca, G. Production of hydrogen from oxidative steam reforming of methanol: I. Preparation and characterization of Cu/ZnO/Al₂O₃ catalysts from a hydrotalcite-like LDH precursor. *J. Catal.* **2004**, *228*, 43–55. [[CrossRef](#)]
209. Pojanavaraphan, C.; Satitthai, U.; Luengnaruemitchai, A.; Gulari, E. Activity and stability of Au/CeO₂-Fe₂O₃ catalysts for the hydrogen production via oxidative steam reforming of methanol. *J. Ind. Eng. Chem.* **2015**, *22*, 41–52. [[CrossRef](#)]
210. Pérez-Hernández, R.; Gutiérrez-Martínez, A.; Espinosa-Pesqueira, M.; Estanislao, M.L.; Palacios, J. Effect of the bimetallic Ni/Cu loading on the ZrO₂ support for H₂ production in the autothermal steam reforming of methanol. *Catal. Today* **2015**, *250*, 166–172. [[CrossRef](#)]
211. Mierczynski, P.; Vasilev, K.; Mierczynska, A.; Maniukiewicz, W.; Ciesielski, R.; Rogowski, J.; Szykowska, I.M.; Trifonov, A.Y.; Dubkov, S.V.; Gromov, D.G. The effect of gold on modern bimetallic Au-Cu/MWCNT catalysts for the oxy-steam reforming of methanol. *Catal. Sci. Technol.* **2016**, *6*, 4168–4183. [[CrossRef](#)]
212. Jampa, S.; Jamieson, A.M.; Chaisuwan, T.; Luengnaruemitchai, A.; Wongkasemjit, S. Achievement of hydrogen production from autothermal steam reforming of methanol over Cu-loaded mesoporous CeO₂ and Cu-loaded mesoporous CeO₂-ZrO₂ catalysts. *Int. J. Hydrogen Energy* **2017**, *42*, 15073–15084. [[CrossRef](#)]
213. Pu, Y.-C.; Li, S.-R.; Yan, S.; Huang, X.; Wang, D.; Ye, Y.-Y.; Liu, Y.-Q. An improved Cu/ZnO catalyst promoted by Sc₂O₃ for hydrogen production from methanol reforming. *Fuel* **2019**, *241*, 607–615. [[CrossRef](#)]
214. Adeniyi, A.G.; Ighalo, J.O. A review of steam reforming of glycerol. *Chem. Pap.* **2019**, *73*, 2619–2635. [[CrossRef](#)]
215. Roslan, N.A.; Abidin, S.Z.; Ideris, A.; Vo, D.-V.N. A review on glycerol reforming processes over Ni-based catalyst for hydrogen and syngas productions. *Int. J. Hydrogen Energy* **2019**. [[CrossRef](#)]
216. Bulutoglu, P.S.; Say, Z.; Bac, S.; Ozensoy, E.; Avci, A.K. Dry reforming of glycerol over Rh-based ceria and zirconia catalysts: New insights on catalyst activity and stability. *Appl. Catal. A Gen.* **2018**, *564*, 157–171. [[CrossRef](#)]
217. Bagnato, G.; Iulianelli, A.; Sanna, A.; Basile, A. Glycerol Production and Transformation: A Critical Review with Particular Emphasis on Glycerol Reforming Reaction for Producing Hydrogen in Conventional and Membrane Reactors. *Membranes* **2017**, *7*, 17. [[CrossRef](#)]
218. Silva, J.; Soria, M.A.; Madeira, L.M. Challenges and strategies for optimization of glycerol steam reforming process. *Renew. Sustain. Energy Rev.* **2015**, *42*, 1187–1213. [[CrossRef](#)]
219. Schwengber, C.A.; Alves, H.J.; Schaffner, R.A.; Silva, F.A.; Sequinel, R.; Bach, V.R.; Ferracin, R.J. Overview of glycerol reforming for hydrogen production. *Renew. Sustain. Energy Rev.* **2016**, *58*, 259–266. [[CrossRef](#)]
220. Seadira, T.; Sadanandam, G.; Ntho, T.A.; Lu, X.; Masuku, C.M.; Scurrrell, M. Hydrogen production from glycerol reforming: Conventional and green production. *Rev. Chem. Eng.* **2018**, *34*, 695–726. [[CrossRef](#)]
221. Charisiou, N.; Siakavelas, G.; Papageridis, K.; Baklavaris, A.; Tzounis, L.; Polychronopoulou, K.; Goula, M. Hydrogen production via the glycerol steam reforming reaction over nickel supported on alumina and lanthana-alumina catalysts. *Int. J. Hydrogen Energy* **2017**, *42*, 13039–13060. [[CrossRef](#)]
222. Gallegos-Suárez, E.; Guerrero-Ruiz, A.; Rodríguez-Ramos, I. Efficient hydrogen production from glycerol by steam reforming with carbon supported ruthenium catalysts. *Carbon* **2016**, *96*, 578–587. [[CrossRef](#)]
223. Papageridis, K.; Siakavelas, G.; Charisiou, N.D.; Avraam, D.; Tzounis, L.; Kousi, K.; Goula, M. Comparative study of Ni, Co, Cu supported on γ -alumina catalysts for hydrogen production via the glycerol steam reforming reaction. *Fuel Process. Technol.* **2016**, *152*, 156–175. [[CrossRef](#)]
224. Charisiou, N.D.; Papageridis, K.; Siakavelas, G.; Tzounis, L.; Kousi, K.; Baker, M.A.; Hinder, S.J.; Sebastian, V.; Polychronopoulou, K.; Goula, M. Glycerol Steam Reforming for Hydrogen Production over Nickel Supported on Alumina, Zirconia and Silica Catalysts. *Top. Catal.* **2017**, *60*, 1226–1250. [[CrossRef](#)]
225. Charisiou, N.; Siakavelas, G.; Tzounis, L.; Dou, B.; Sebastian, V.; Hinder, S.; Baker, M.; Polychronopoulou, K.; Goula, M. Ni/Y₂O₃-ZrO₂ catalyst for hydrogen production through the glycerol steam reforming reaction. *Int. J. Hydrogen Energy* **2020**, *45*, 10442–10460. [[CrossRef](#)]
226. Senseni, A.Z.; Rezaei, M.; Meshkani, F. Glycerol steam reforming over noble metal nanocatalysts. *Chem. Eng. Res. Des.* **2017**, *123*, 360–366. [[CrossRef](#)]
227. Silva, J.; Ribeiro, L.; Órfão, J.; Soria, M.A.; Madeira, L.M. Low temperature glycerol steam reforming over a Rh-based catalyst combined with oxidative regeneration. *Int. J. Hydrogen Energy* **2019**, *44*, 2461–2473. [[CrossRef](#)]

228. Jiang, B.; Zhang, C.; Wang, K.; Dou, B.; Song, Y.; Chen, H.; Xu, Y. Highly dispersed Ni/montmorillonite catalyst for glycerol steam reforming: Effect of Ni loading and calcination temperature. *Appl. Therm. Eng.* **2016**, *109*, 99–108. [[CrossRef](#)]
229. Bepari, S.; Pradhan, N.C.; Dalai, A.K. Selective production of hydrogen by steam reforming of glycerol over Ni/Fly ash catalyst. *Catal. Today* **2017**, *291*, 36–46. [[CrossRef](#)]
230. Wang, Y.; Chen, M.; Yang, Z.; Liang, T.; Liu, S.; Zhou, Z.; Li, X. Bimetallic Ni-M (M = Co, Cu and Zn) supported on attapulgite as catalysts for hydrogen production from glycerol steam reforming. *Appl. Catal. A Gen.* **2018**, *550*, 214–227. [[CrossRef](#)]
231. Carrero, A.; Calles, J.; García-Moreno, L.; Vizcaíno, A. Production of Renewable Hydrogen from Glycerol Steam Reforming over Bimetallic Ni-(Cu,Co,Cr) Catalysts Supported on SBA-15 Silica. *Catalysts* **2017**, *7*, 55. [[CrossRef](#)]
232. Wang, R.; Liu, S.; Liu, S.; Li, X.; Zhang, Y.; Xie, C.; Zhou, S.; Qiu, Y.; Luo, S.; Jing, F.; et al. Glycerol steam reforming for hydrogen production over bimetallic MNi/CNTs (M Co, Cu and Fe) catalysts. *Catal. Today* **2019**. [[CrossRef](#)]
233. Tavanarad, M.; Meshkani, F.; Rezaei, M. Production of syngas via glycerol dry reforming on Ni catalysts supported on mesoporous nanocrystalline Al₂O₃. *J. CO₂ Util.* **2018**, *24*, 298–305. [[CrossRef](#)]
234. Bac, S.; Say, Z.; Koçak, Y.; Ercan, K.E.; Harfouche, M.; Ozensoy, E.; Avci, A.K. Exceptionally active and stable catalysts for CO₂ reforming of glycerol to syngas. *Appl. Catal. B Environ.* **2019**, *256*, 117808. [[CrossRef](#)]
235. Larimi, A.; Kazemeini, M.; Khorasheh, F. Aqueous phase reforming of glycerol using highly active and stable Pt_{0.05}Ce_xZr_{0.95-x}O₂ ternary solid solution catalysts. *Appl. Catal. A Gen.* **2016**, *523*, 230–240. [[CrossRef](#)]
236. Espinosa-Moreno, F.; Balla, P.; Shen, W.; Chavarría-Hernández, J.C.; Ruiz-Gómez, M.; Tlecuítl-Beristain, S. Ir-Based Bimetallic Catalysts for Hydrogen Production through Glycerol Aqueous-Phase Reforming. *Catalysts* **2018**, *8*, 613. [[CrossRef](#)]
237. Kousi, K.; Chourdakis, N.; Matralis, H.; Kontarides, D.; Papadopoulou, C.; Verykios, X. Glycerol steam reforming over modified Ni-based catalysts. *Appl. Catal. A Gen.* **2016**, *518*, 129–141. [[CrossRef](#)]
238. Cheng, C.-K.; Foo, S.Y.; Adesina, A.A. Glycerol Steam Reforming over Bimetallic Co–Ni/Al₂O₃. *Ind. Eng. Chem. Res.* **2010**, *49*, 10804–10817. [[CrossRef](#)]
239. Zamzuri, N.H.; Mat, R.; Amin, N.A.S.; Talebian-Kiakalaieh, A. Hydrogen production from catalytic steam reforming of glycerol over various supported nickel catalysts. *Int. J. Hydrogen Energy* **2017**, *42*, 9087–9098. [[CrossRef](#)]
240. Bobadilla, L.; Penkova, A.; Alvarez, A.; Domínguez, M.; Romero-Sarria, F.; Centeno, M.A.; Odriozola, J.; Leal, M.I.D. Glycerol steam reforming on bimetallic NiSn/CeO₂–MgO–Al₂O₃ catalysts: Influence of the support, reaction parameters and deactivation/regeneration processes. *Appl. Catal. A Gen.* **2015**, *492*, 38–47. [[CrossRef](#)]
241. Charisiou, N.; Papageridis, K.; Tzounis, L.; Sebastian, V.; Hinder, S.; Baker, M.; Alketbi, M.; Polychronopoulou, K.; Goula, M. Ni supported on CaO–MgO–Al₂O₃ as a highly selective and stable catalyst for H₂ production via the glycerol steam reforming reaction. *Int. J. Hydrogen Energy* **2019**, *44*, 256–273. [[CrossRef](#)]
242. Menezes, J.P.D.S.; Duarte, K.R.; Manfro, R.L.; Souza, M.M.V.M. Effect of niobia addition on cobalt catalysts supported on alumina for glycerol steam reforming. *Renew. Energy* **2020**, *148*, 864–875. [[CrossRef](#)]
243. Arif, N.N.M.; Vo, D.-V.N.; Azizan, M.T.; Abidin, S.Z. Carbon Dioxide Dry Reforming of Glycerol for Hydrogen Production using Ni/ZrO₂ and Ni/CaO as Catalysts. *Bull. Chem. React. Eng. Catal.* **2016**, *11*, 200. [[CrossRef](#)]
244. Lee, H.-J.; Shin, G.S.; Kim, Y.-C. Characterization of supported Ni catalysts for aqueous-phase reforming of glycerol. *Korean J. Chem. Eng.* **2015**, *32*, 1267–1272. [[CrossRef](#)]
245. Yancheshmeh, M.S.; Sahraei, O.A.; Aissaoui, M.; Iliuta, M.C. A novel synthesis of NiAl₂O₄ spinel from a Ni–Al mixed-metal alkoxide as a highly efficient catalyst for hydrogen production by glycerol steam reforming. *Appl. Catal. B Environ.* **2020**, *265*, 118535. [[CrossRef](#)]
246. Lima, D.S.; Calgaro, C.O.; Perez-Lopez, O.W. Hydrogen production by glycerol steam reforming over Ni based catalysts prepared by different methods. *Biomass Bioenergy* **2019**, *130*, 105358. [[CrossRef](#)]
247. Dieuzeide, M.; Laborde, M.; Amadeo, N.; Cannilla, C.; Bonura, G.; Frusteri, F. Hydrogen production by glycerol steam reforming: How Mg doping affects the catalytic behaviour of Ni/Al₂O₃ catalysts. *Int. J. Hydrogen Energy* **2016**, *41*, 157–166. [[CrossRef](#)]

248. Demsash, H.; Mohan, R. Steam reforming of glycerol to hydrogen over ceria promoted nickel–alumina catalysts. *Int. J. Hydrogen Energy* **2016**, *41*, 22732–22742. [[CrossRef](#)]
249. Carrero, A.; Vizcaíno, A.; Calles, J.; García-Moreno, L. Hydrogen production through glycerol steam reforming using Co catalysts supported on SBA-15 doped with Zr, Ce and La. *J. Energy Chem.* **2017**, *26*, 42–48. [[CrossRef](#)]
250. Veiga, S.; Bussi, J. Steam reforming of crude glycerol over nickel supported on activated carbon. *Energy Convers. Manag.* **2017**, *141*, 79–84. [[CrossRef](#)]
251. Sahraei, O.A.Z.; Larachi, F.; Abatzoglou, N.; Iliuta, M. Hydrogen production by glycerol steam reforming catalyzed by Ni-promoted Fe/Mg-bearing metallurgical wastes. *Appl. Catal. B Environ.* **2017**, *219*, 183–193. [[CrossRef](#)]
252. Dobosz, J.; Cichy, M.; Zawadzki, M.; Borowiecki, T. Glycerol steam reforming over calcium hydroxyapatite supported cobalt and cobalt-cerium catalysts. *J. Energy Chem.* **2018**, *27*, 404–412. [[CrossRef](#)]
253. Siew, K.W.; Lee, H.C.; Gim bun, J.; Chin, S.Y.; Khan, M.R.; Taufiq-Yap, Y.H.; Cheng, C.-K. Syngas production from glycerol-dry(CO₂) reforming over La-promoted Ni/Al₂O₃ catalyst. *Renew. Energy* **2015**, *74*, 441–447. [[CrossRef](#)]
254. Reynoso, A.; Iriarte-Velasco, U.; Gutiérrez-Ortiz, M.A.; Ayastuy, J. Highly stable Pt/CoAl₂O₄ catalysts in Aqueous-Phase Reforming of glycerol. *Catal. Today* **2020**. [[CrossRef](#)]
255. Pendem, C.; Sarkar, B.; Siddiqui, N.; Konathala, L.N.S.K.; Baskar, C.; Bal, R. K-Promoted Pt-Hydrotalcite Catalyst for Production of H₂ by Aqueous Phase Reforming of Glycerol. *ACS Sustain. Chem. Eng.* **2017**, *6*, 2122–2131. [[CrossRef](#)]
256. Wang, M.; Au, C.T.; Lai, S.Y. H₂ production from catalytic steam reforming of n-propanol over ruthenium and ruthenium-nickel bimetallic catalysts supported on ceria-alumina oxides with different ceria loadings. *Int. J. Hydrogen Energy* **2015**, *40*, 13926–13935. [[CrossRef](#)]
257. Patel, R.; Patel, S. Process development for bio-butanol steam reforming for PEMFC application. *Int. J. Eng. Technol.* **2018**, *7*, 110–112. [[CrossRef](#)]
258. Patel, R.; Patel, S. Effect of operating conditions on hydrogen production in butanol reforming: A review. *Int. Conf. Multidiscip. Res. Pract.* **2015**, 145–150.
259. Patel, R.; Patel, S. Renewable hydrogen production from butanol: A review. *Clean Energy* **2017**, *1*, 90–101. [[CrossRef](#)]
260. Harju, H.; Lehtonen, J.; Lefferts, L. Steam reforming of n-butanol over Rh/ZrO₂ catalyst: Role of 1-butene and butyraldehyde. *Appl. Catal. B Environ.* **2016**, *182*, 33–46. [[CrossRef](#)]
261. Dhanala, V.; Maity, S.K.; Shee, D. Oxidative steam reforming of isobutanol over Ni/γ-Al₂O₃ catalysts: A comparison with thermodynamic equilibrium analysis. *J. Ind. Eng. Chem.* **2015**, *27*, 153–163. [[CrossRef](#)]
262. Wang, Y.; Yang, X.; Wang, Y. Catalytic performance of mesoporous MgO supported Ni catalyst in steam reforming of model compounds of biomass fermentation for hydrogen production. *Int. J. Hydrogen Energy* **2016**, *41*, 17846–17857. [[CrossRef](#)]
263. Yadav, A.K.; Vaidya, P.D. Renewable hydrogen production by steam reforming of butanol over multiwalled carbon nanotube-supported catalysts. *Int. J. Hydrogen Energy* **2019**, *44*, 30014–30023. [[CrossRef](#)]
264. Harju, H.; Lehtonen, J.; Lefferts, L. Steam- and autothermal-reforming of n-butanol over Rh/ZrO₂ catalyst. *Catal. Today* **2015**, *244*, 47–57. [[CrossRef](#)]
265. Harju, H.; Pipitone, G.; Lefferts, L. Influence of the catalyst particle size on the aqueous phase reforming of n-butanol over Rh/ZrO₂. *Front. Chem.* **2020**, *8*, 17. [[CrossRef](#)]
266. Yadav, A.K.; Vaidya, P.D. A study on the efficacy of noble metal catalysts for butanol steam reforming. *Int. J. Hydrogen Energy* **2019**, *44*, 25575–25588. [[CrossRef](#)]
267. Bizkarra, K.; Barrio, V.; Yartu, A.; Requies, J.M.; Arias, P.L.; Cambra, J.F. Hydrogen production from n-butanol over alumina and modified alumina nickel catalysts. *Int. J. Hydrogen Energy* **2015**, *40*, 5272–5280. [[CrossRef](#)]
268. Lobo, R.; Marshall, C.L.; Dietrich, P.J.; Ribeiro, F.H.; Akatay, C.; Stach, E.A.; Mane, A.; Lei, Y.; Elam, J.; Miller, J.T. Understanding the chemistry of H₂ production for 1-propanol reforming: Pathway and support modification effects. *ACS Catal.* **2012**, *2*, 2316–2326. [[CrossRef](#)]
269. Li, Y.; Zhang, L.; Zhang, Z.; Liu, Q.; Zhang, S.; Liu, Q.; Hu, G.; Wang, Y.; Hu, X. Steam reforming of the alcohols with varied structures: Impacts of acidic sites of Ni catalysts on coking. *Appl. Catal. A Gen.* **2019**, *584*, 117162. [[CrossRef](#)]

270. Shejale, A.D.; Yadav, G.D. Noble metal promoted Ni–Cu/La₂O₃–MgO catalyst for renewable and enhanced hydrogen production via steam reforming of bio-based n-butanol: Effect of promotion with Pt, Ru and Pd on catalytic activity and selectivity. *Clean Technol. Environ. Policy* **2019**, *21*, 1323–1339. [[CrossRef](#)]
271. Sharma, M.P.; Akyurtlu, J.F.; Akyurtlu, A. Autothermal reforming of isobutanol over promoted nickel xerogel catalysts for hydrogen production. *Int. J. Hydrogen Energy* **2015**, *40*, 13368–13378. [[CrossRef](#)]
272. Lei, Y.; Lee, S.; Low, K.-B.; Marshall, C.L.; Elam, J.W. Combining Electronic and Geometric Effects of ZnO-Promoted Pt Nanocatalysts for Aqueous Phase Reforming of 1-Propanol. *ACS Catal.* **2016**, *6*, 3457–3460. [[CrossRef](#)]



© 2020 by the authors. Licensee MDPI, Basel, Switzerland. This article is an open access article distributed under the terms and conditions of the Creative Commons Attribution (CC BY) license (<http://creativecommons.org/licenses/by/4.0/>).